

PEROVSKITE ALKALINE EARTH TITANATES BASED NANOMATERIALS AS PHOTOCATALYSTS

Thesis

Submitted in partial fulfilment of the requirements for the degree of

DOCTOR OF PHILOSOPHY

by

HARSHA B



DEPARTMENT OF CHEMISTRY

NATIONAL INSTITUTE OF TECHNOLOGY KARNATAKA,

SURATHKAL, MANGALURU – 575025

March, 2023

DECLARATION

by the Ph.D. Research Scholar

I hereby declare that the Research Thesis entitled “**Perovskite alkaline earth titanates based nanomaterials as photocatalysts**” which is being submitted to the National Institute of Technology Karnataka, Surathkal in partial fulfilment of the requirements for the award of the Degree of Doctor of Philosophy in Chemistry is a *bonafide report of the research work carried out by me*. The material contained in this Research Thesis has not been submitted to any University or Institution for the award of any degree.

Harsha B

Harsha B

Register No. 158034CY15F09

Department of Chemistry

Place: NITK-Surathkal

Date:

CERTIFICATE

This is to *certify* that the Research Thesis entitled "**Perovskite alkaline earth titanates based nanomaterials as photocatalysts**" submitted by Mr. Harsha B (Register No: 158034CY15F09) as the record of the research work carried out by him, is *accepted as the Research Thesis submission* in partial fulfilment of the requirements for the award of degree of Doctor of Philosophy.



Prof. D. Krishna Bhat

Research Guide

Date: 15-03-2023



Chairman DRPC

Date: 15-03-2023

HEAD, DEPARTMENT OF CHEMISTRY
National Institute of Technology Karnataka
Surathkal, Srinivasnagar
MANGALORE- 575 025, D.K.

No language can express the power, beauty, heroism, and majesty of a mother's love. It shrinks not where man cowers, and grows stronger where man faints, and over the wastes of worldly fortunes sends the radiance of its quenchless fidelity like a star in heaven.

---Edwin Hubbell Chapin

This thesis is dedicated to my beloved mother

ACKNOWLEDGEMENT

I owe my deepest gratitude to the Almighty for giving me the strength and patience to work throughout these years.

I acknowledge the people who are the pillars of my life, my parents, for instilling in me the virtues of perseverance and commitment and relentlessly encouraging me to strive for excellence.

I owe a debt of gratitude to my research supervisor, Prof. D. Krishna Bhat, Department of Chemistry, NITK, Surathkal, for giving me an opportunity to pursue my research work under his valuable guidance, from whom I have learnt how to be humble and patient.

I express my thanks to NITK Surathkal, for providing the research fellowship and the laboratory facilities for my research work.

My sincere gratitude to the RPAC members, Prof. A. C. Hegde, Department of Chemistry, and Prof. S. M. Kulkarni, Department of Mechanical Engineering for their timely assessment and for providing thoughtful suggestions during the progress of my work.

I thank the present Head of the Department, Dr. Udaya Kumar D., and former Head of the Department Prof. Arun M. Isloor for providing the laboratory facilities. I am also thankful to Prof. A. Nithyananda Shetty, Prof. A. V. Adhikari, Prof. B. Ramachandra Bhat, Dr. Darshak R. Trivedi, Dr. Sib Sankar Mal, Dr. Saikat Dutta, Dr. P. B. Beneesh and Dr. Debasree Chakraborty for their encouragement and moral support.

My special thanks to Dr. Sandhya Shenoy for her kind cooperation and support during my research work.

I sincerely thank my lab members, Mr. Pavan Kumar S., Ms. Uma P. I., Ms. Theertha P. Ramesh and Ms. Bhava, for their active co-operation and for rebuilding my confidence at each and every stage of my research work. A special thanks to my research colleague Dr. Meenaketan Sethi for constant help, support, and all the fun we had in the last five years.

The saying “A real friend is the one who walks in when the rest of the world walks out” holds true and it’s my fortune to gratefully acknowledge the support of my friends, Dr. Viprabha, Dr. Rajkumar Reddyrajula, Dr. Akshatha R Shetty, Dr. Aranganathan, Dr. Dilip, Dr. Praveen Mishra, Mr. Yathish Rai and Mr. Kalinga Nayak for their support and generous care throughout the research tenure. They were always beside me during the happy and hard moments to push me and motivate me, without whom the learning curve would have been very much steeper.

It will not be complete without mentioning my gratitude to the non-teaching staff members of the Chemistry Department Mrs. Shamila Nandini, Ms. Vikitha, Mrs. Rashmi, Mr. Prashanth, Mr. Pradeep, Mr. Harish, Mrs. Sharmila, Mrs. Deepa, Mr. Santhosh, Mr. Gopal and Mr. Vaman Shetty for their timely help during my research.

This thesis would not have been possible without the inspiration and support of many wonderful individuals — my thanks and appreciation to all of them who are scattered around the country for being part of this journey and making this possible.

HARSHA B

ABSTRACT

The research thesis entitled '**Perovskite alkaline earth titanates based nanomaterials as photocatalysts**' deals with the synthesis, characterization and photocatalytic studies of some doped perovskite alkaline earth titanates and porous graphene-perovskite alkaline earth titanate nanocomposites. The present study reports the successful synthesis of seven different series of novel perovskite alkaline earth titanate-based materials namely, Rh-doped SrTiO₃, V-doped SrTiO₃, porous graphene-SrTiO₃ nanocomposite (PGST), Rh-doped BaTiO₃, porous graphene-BaTiO₃ nanocomposite (PGBT), V-doped CaTiO₃ and porous graphene-CaTiO₃ nanocomposite (PGCT) using facile solvothermal/hydrothermal method. All the synthesized materials were carefully characterized for their elemental composition, structural, morphological, and optical properties by employing appropriate techniques such as XRD, FESEM, EDS, TEM, HRTEM, Raman Spectroscopy, XPS, BET, DRS, and PL spectroscopy. Thereafter, each material was investigated for its catalytic efficiency towards the degradation of methylene blue dye under visible light irradiation. The synthesized materials exhibited enhanced photocatalytic efficiency which could be attributed to the efficient visible light harvesting capacity and reduced rate of recombination of photoinduced charges.

Keywords: Doping; Graphene; Perovskite; Methylene blue; Photocatalysis; Solvothermal.

CONTENTS

CHAPTER 1 INTRODUCTION	11
1.1 PEROVSKITE TITANATES OVERVIEW	3
1.2 GRAPHENE OVERVIEW	4
1.3 CATALYSIS.....	5
1.3.1 Photocatalysis.....	5
1.3.2 Mechanism of Photocatalysis.....	6
1.3.3 Thermodynamic Requirement for the Generation of Active Species	8
1.3.4 Photocatalytic Reactor.....	8
1.3.5 Modification Routes for Extending Visible Light Response of Catalysts	8
1.3.5.1 Doping	8
1.3.5.2 Dye Sensitization.....	9
1.3.5.3 Heterostructure	10
1.3.5.4 Coupled with π -Conjugated Structure	11
1.4 A REVIEW OF LITERATURE	12
1.4.1 Graphene	12
1.4.2 Perovskite Titanates	14
1.5 PROBLEM IDENTIFICATION.....	20
1.6 SCOPE AND OBJECTIVES OF THE WORK.....	21
1.7 THESIS WORK.....	22
CHAPTER 2 SOLVOTHERMAL SYNTHESIS OF RHODIUM-DOPE STRONTIUM TITANATE FOR PHOTOCATALYTIC APPLICATION.....	25
2.1 INTRODUCTION	27
2.2 EXPERIMENTAL SECTION	27
2.2.1 Synthesis.....	27

2.2.2 Characterization	28
2.2.3 Determination of Photocatalytic Activity	28
2.3 RESULTS AND DISCUSSION	28
2.3.1 XRD Analysis	28
2.3.2 FESEM, EDS and TEM Analysis	29
2.3.3 XPS Analysis	30
2.3.4 Optical Absorbance Analysis	31
2.3.5 Photocatalytic Activity	33
2.3.6 Photocatalytic Reaction Mechanism	35
CHAPTER 3 SOLVOTHERMAL SYNTHESIS OF VANADIUM-DOPED STRONTIUM TITANATE FOR PHOTOCATALYTIC APPLICATION	39
3.1 INTRODUCTION	41
3.2 EXPERIMENTAL SECTION	41
3.2.1 Synthesis	41
3.3 RESULTS AND DISCUSSION	42
3.3.1 XRD Analysis	42
3.3.2 TEM and EDS Analysis	43
3.3.3 BET Surface Area Analysis	44
3.3.4 XPS Analysis	44
3.3.5 Optical Absorbance Analysis	46
3.3.6 Photocatalytic Activity	48
CHAPTER 4 SOLVOTHERMAL SYNTHESIS OF POROUS GRAPHENE- STRONTIUM TITANATE NANOCOMPOSITE FOR PHOTOCATALYTIC APPLICATION	523
4.1 INTRODUCTION	55
4.2 EXPERIMENTAL SECTION	56
4.2.1 Synthesis of PGST Composite	56

4.2.2 Characterization	56
4.3 RESULTS AND DISCUSSION	57
4.3.1 XRD Analysis	57
4.3.2 Raman Analysis.....	58
4.3.3 FESEM and TEM analysis.....	58
4.3.4 BET Surface Area Analysis	59
4.3.5 XPS Analysis	60
4.3.6 Optical Absorbance Analysis	62
4.3.7 Photocatalytic Activity	62
CHAPTER 5 HYDROTHERMAL SYNTHESIS OF RHODIUM-DOPED BARIUM TITANATE FOR PHOTOCATALYTIC APPLICATION	67
5.1 INTRODUCTION	69
5.2 EXPERIMENTAL SECTION	70
5.2.1 Synthesis.....	70
5.3 RESULTS AND DISCUSSION	70
5.3.1 XRD Analysis	70
5.3.2 EDS and TEM Analysis	71
5.3.3 BET Surface Area Analysis	72
5.3.4 XPS Analysis	73
5.3.5 Optical Absorbance Analysis	75
5.3.6 Photocatalytic Activity	76
CHAPTER 6 SOLVOTHERMAL SYNTHESIS OF POROUS GRAPHENE- BARIUM TITANATE NANOCOMPOSITE FOR PHOTOCATALYTIC APPLICATION	851
6.1 INTRODUCTION	83
6.2 EXPERIMENTAL SECTION	83
6.2.1 Synthesis of PGBT Composite.....	83

6.3 RESULTS AND DISCUSSION	84
6.3.1 XRD Analysis	84
6.3.2 Raman Analysis.....	85
6.3.3 TEM Analysis	86
6.3.4 BET Surface Area Analysis	87
6.3.5 XPS Analysis	88
6.3.6 Optical Absorbance Analysis	90
6.3.7 Photocatalytic Activity	91
CHAPTER 7 SOLVOTHERMAL SYNTHESIS OF VANADIUM-DOPED CALCIUM TITANATE FOR PHOTOCATALYTIC APPLICATION.....	967
7.1 INTRODUCTION	99
7.2 EXPERIMENTAL SECTION	100
7.2.1 Synthesis.....	100
7.3 RESULTS AND DISCUSSION	100
7.3.1 XRD Analysis	100
7.3.2 FESEM and TEM analysis.....	101
7.3.3 BET Surface Area Analysis	102
7.3.4 XPS Analysis	103
7.3.5 Optical Absorbance Analysis	105
7.3.6 Photocatalytic Activity	106
CHAPTER 8 SOLVOTHERMAL SYNTHESIS OF POROUS GRAPHENE- CALCIUM TITANATE NANOCOMPOSITE FOR PHOTOCATALYTIC APPLICATION	1151
8.1 INTRODUCTION	113
8.2 EXPERIMENTAL SECTION	113
8.2.1 Synthesis.....	113
8.3 RESULTS AND DISCUSSION	114

8.3.1 XRD Analysis	114
8.3.2 Raman Analysis.....	115
8.3.3 FESEM and TEM Analysis.....	116
8.3.4 BET Surface Area Analysis	117
8.3.5 XPS Analysis	118
8.3.6 Optical Absorbance Analysis	120
8.3.7 Photocatalytic Activity	121
CHAPTER 9 SUMMERY AND CONCLUSIONS.....	127
9.1 SUMMARY	129
9.2 CONCLUSIONS.....	131
9.3 SCOPE FOR FUTURE WORK.....	136
REFERENCES	137
LIST OF PUBLICATIONS	159
CONFERENCES ATTENDED.....	160
BIODATA.....	161

NOMENCLATURE

LIST OF ABBREVIATIONS

BET	Brunauer-Emmett-Teller
BJH	Barrett-Joyner-Halenda
CB	Conduction Band
DRS	Diffuse Reflectance Spectroscopy
FESEM	Field Emission Scanning Electron Microscopy
FWHM	Full Width at Half Maximum
GO	Graphene Oxide
HRTEM	High-Resolution Transmission Electron Microscopy
LUMO	Lowest Unoccupied Molecular Orbital
MB	Methylene Blue
PL	Photo-Luminescence
RGO	Reduced Graphene Oxide
TEM	Transmission Electron Microscopy
VB	Valence Band
XPS	X-Ray Photoelectron Spectroscopy
XRD	X-Ray Diffraction

CHAPTER 1

INTRODUCTION

This chapter gives a brief introduction to the basic concepts of the study undertaken. It also gives a summary of the relevant works in the literature which will focus on perovskite titanates, graphene, doped-perovskite titanates, graphene-based nanocomposites, their synthetic methods, and photocatalytic applications. The scope and objectives of the present research work have been given at the end of this chapter.

1.1 PEROVSKITE TITANATES OVERVIEW

Perovskite is a calcium titanate with the chemical formula CaTiO_3 , a mineral discovered by Gustav Rose in 1839 and is named after Russian mineralogist Count Lev Alekseevich Perovski (1792-1856). Perovskites are the family of compounds represented with the general formula ABO_3 where A site is occupied by the larger cation and B site is occupied by the smaller cation. In this crystal structure, the corner is occupied by BO_6 octahedra (where B cation is positioned at the center of the octahedron). The A-site cations occupy the cavities created by these 8 octahedra and thus leading to the 12-fold cub-octahedral coordination of oxygen anions. However, a slight buckling and distortion of the octahedra takes place, depending upon the ionic radii and electronegativity of the A and B site cations. This distortion gives rise to lower symmetry structures. Different degrees of structural distortion of the BO_6 octahedra gives rise to different crystal fields, which may influence the band structure, dielectric, photoluminescence, piezoelectric, ferroelectric, pyroelectric, hole, and electron transport properties (Kanhere and Chen 2014).

From the perspective of photocatalysis, perovskite structure compounds have many advantages over binary metal oxides. Firstly, perovskites possess suitable band edge potentials which will favor various photoinduced reactions (Phoon et al. 2019). Secondly, the flexibility of the A site and B site for cation doping can alter the band structure and thus lead to a noticeable change in the photophysical properties (Irshad et al. 2022). Thirdly, it is possible to combine the properties like ferroelectricity or piezoelectric with that of the photocatalytic property to enhance the photocatalytic activity (Xu et al. 2019). In particular perovskite alkaline earth titanates (ATiO_3) like SrTiO_3 , BaTiO_3 and CaTiO_3 have sparked the scientist community due to their high dielectric constant, low dielectric loss, high thermal stability, high chemical stability,

wide band gap and high mechanical stability (Rayssi et al. 2018, Zhang et al. 2017, Kumar et al. 2020).

They can be used in a variety of applications which includes dynamic random access memory, multilayer capacitors, thermistors, sensors, high-temperature superconductors, solid oxide fuel cell, hydrogen storage, piezoelectric devices, and photocatalysis (Xiao et al. 2020, Priyadharsini et al. 2020, Hanani et al. 2021, Taşyürek et al. 2018, Singh et al. 2018, Yahya et al. 2018, Ren et al. 2020, Zhang et al. 2021, Shi et al. 2021). Several methods have been reported for the synthesis of ATiO_3 which includes the hydrothermal method (Wong et al. 2021), solvothermal method (Chen et al. 2020), solid-state reaction (Qi et al. 2020), sol-gel method (Hussain et al. 2020), molten salt synthesis (Zhou et al. 2021), co-precipitation method (Zhang et al. 2021) and combustion method (Jongprateep et al. 2019) among which solvothermal (or hydrothermal) approach is an effective method because of its high purity, lower energy consumption, eco-friendly characteristics. Moreover, the crystallinity, morphology, and size can be fine-tuned by controlling various synthetic parameters like reaction temperature, reaction time, nature of solvents and surfactants (Phoon et al. 2019).

1.2 GRAPHENE OVERVIEW

Graphene, a 2D layer of sp^2 hybridized carbon atoms with a hexagonal pattern is known to possess many interesting properties such as large theoretical surface area ($2630 \text{ m}^2\text{g}^{-1}$), high electron mobility ($\sim 200,000 \text{ cm}^2\text{V}^{-1}\text{s}^{-1}$), high Young's modulus ($\sim 1 \text{ TPa}$), high thermal conductivity ($3000\text{-}5000 \text{ Wm}^{-1}\text{K}^{-1}$), excellent optical transparency and good chemical stability (Kusiak-Nejman and Morawski 2019). Porous graphene consists of few-layered planar graphene sheets that possess high surface area, excellent hydrophobicity, optical transparency, high chemical stability, and structural stability. Such porous structures afford smooth access for the contaminants, expediting faster adsorption and desorption of contaminants (Tabish et al. 2018). These unique properties make it well suitable for many potential applications such as memory devices, transistors, surface-enhanced Raman spectroscopy, sensor, supercapacitor, batteries, fuel cells, catalysis, dye-sensitized solar cell, drug delivery, and so on (Sattari-Esfahlan and Kim 2021, Deng et al. 2019, You et al. 2019, Huo et

al. 2019, Lee et al. 2020, Wang et al. 2020, Su and Hu 2021, Wang et al. 2020, Mahalingam et al. 2021, Song et al. 2020). Currently, several methods can be implemented for the production of single or few-layered graphene sheets which include epitaxial growth on single-crystal silicon carbide, the epitaxial growth of graphene films on metal surfaces like Co, Ni, Cu, Pt, Ir, and Ru using CVD and the most widely used technique is the initial oxidation of graphite to graphene oxide by improved/Hummers method followed by the subsequent reduction to RGO or graphene (Mishra et al. 2016, Wu et al. 2019, Alkhouzaam et al. 2020).

1.3 CATALYSIS

The term “catalysis” was first coined by the Swedish chemist Berzelius in 1835. Catalysis can be defined as the increase in the rate of a chemical reaction by the addition of a reagent without itself being consumed. The catalyst alters the path of the reaction by lowering the activation barrier between the reactants and the products. Types of catalysis include homogeneous catalysis, heterogeneous catalysis, biocatalysis, phase transfer catalysis, organocatalysis, electrocatalysis, photocatalysis, asymmetric catalysis, and so on (Viswanathan et al. 2002). Nanocatalysts are composed of nano-dimensional particles (nanometals or nano metal oxides) with a large exposed surface area, which can boost the accessibility of the active sites to the reactants and have been used in a variety of applications which include environmental remediation, food processing, refining, sensors, energy conversion and storage, reforming, biorefinery and so on (Prinsen and Luque 2019).

1.3.1 Photocatalysis

Environmental pollution is one of the most serious problems faced by developed and developing countries in the world. The most common pollutants include chlorinated and non-chlorinated aliphatic and aromatic compounds, detergents, dyes, agricultural wastes, plastics, heavy metals, toxic gases (CO, NH₃, NO_x, SO_x), and so on. Water is imperative to life. A major portion of water is constituted by aquatic resources such as salted waters of oceans, seas, and glaciers. About only 0.65 % of the water total mass can be usable by man. Dyes find many applications in our daily life including clothing, food, paper, leather, cosmetics, drugs,

electronics, plastics, and printing. Nearly 80 % of the synthetic dyes are consumed by the textile industry.

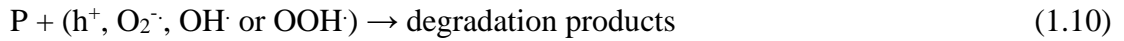
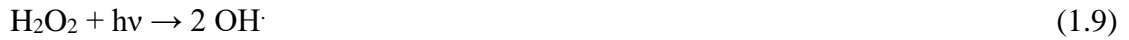
One of the major congestions in the textile industry is the dye treatment and nearly 10 % of the dyes are discharged to the effluent as a result of several washing processes (Vinu and Madras 2010). Therefore, there is an imperative need of developing potent and eco-friendly techniques to treat wastewater. Advanced oxidation processes (AOPs) have been defined by Glaze et al. (1987) and they play a vital role in the removal of persistent organic pollutants.

Photocatalysis is an integral part of the AOPs, which means these processes exploit oxidizing agents like hydrogen peroxide (H₂O₂), ozone, Fenton's reagent (H₂O₂+Fe²⁺) for the effectual degradation of the pollutants. Photocatalysis refers to the acceleration of the rate of chemical reactions (oxidation/reduction) in the presence of a catalyst generally a semiconductor oxide by UV/visible radiation. In 1972 Fujishima and Honda discovered that water can be split simultaneously into oxygen and hydrogen under an applied bias to an irradiated TiO₂ single-crystal electrode. This notable discovery pointed the onset of photoinduced redox reactions on semiconductor surfaces.

1.3.2 Mechanism of Photocatalysis

In general, heterogeneous photocatalysis consists of a semiconductor (SC) which can harvest light energy to produce several active species to expedite the degradation of recalcitrant pollutants. The photocatalytic mechanism can be represented by the following steps (Dong et al. 2015):





When a SC is irradiated with an energy equal to greater than its bandgap equal number of holes (h^\cdot) and electrons (e^-) are formed in the VB and CB respectively (equation 1.1). The so-formed holes and electrons then migrate to the surface of the semiconductor and participate in the redox reactions. The photogenerated holes oxidize the surface adsorbed water or hydroxyl groups to produce hydroxyl radicals (OH^\cdot) as given in equations (1.2) and (1.3). There is a possibility that the formed holes can directly oxidize the pollutant (P) (equation 1.4). The photoinduced electrons reduce the surface adsorbed oxygen to produce superoxide radicals ($\text{O}_2^{\cdot-}$) as given in equation (1.5), which on further reaction with H^+ to form OOH^\cdot radicals (equation 1.6) which will finally decompose to produce OH^\cdot radicals as shown in equations (1.7), (1.8), and (1.9). Hence, the formed h^\cdot , OH^\cdot , and $\text{O}_2^{\cdot-}$ are said to be active species for the degradation of harmful pollutants to harmless degradation products (equation 1.10). The overall photocatalytic mechanism is schematically shown in Figure 1.1.

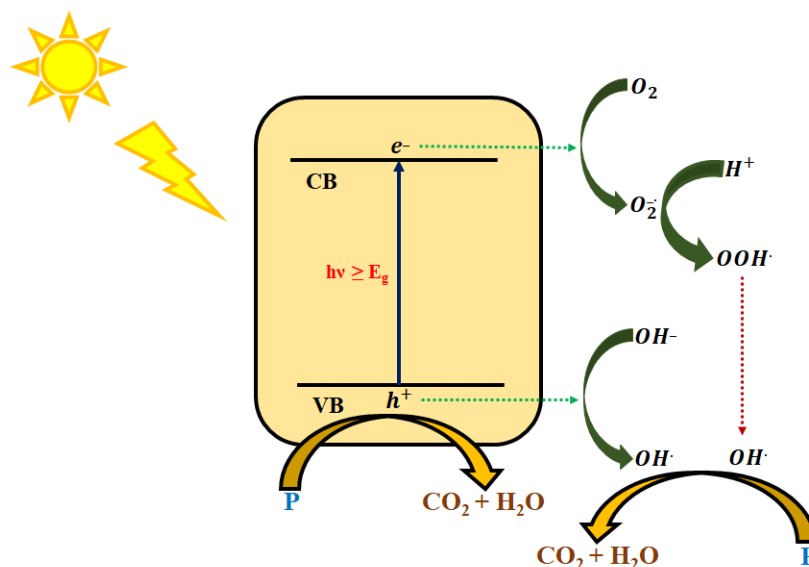


Figure 1.1 Mechanism for the photocatalytic degradation of pollutants.

1.3.3 Thermodynamic Requirement for the Generation of Active Species

The VB and CB of the semiconductor should be located in such a way that the oxidation potential of the hydroxyl radicals $E^\circ (\text{H}_2\text{O}/\text{OH}\cdot) = 2.8 \text{ V vs NHE}$ and the reduction potential of superoxide radicals $E^\circ (\text{O}_2/\text{O}_2^{\cdot-}) = -0.28 \text{ V vs NHE}$ should lie within the band gap. In other words, the redox potential of VB should be sufficiently positive to generate $\text{OH}\cdot$ radicals and the redox potential of CB should be sufficiently negative to generate $\text{O}_2^{\cdot-}$ radicals (Vinu and Madras 2010).

1.3.4 Photocatalytic Reactor

Photocatalytic reactors of volumes ranging from 0.1-10 L are commonly used to study the photocatalytic activity of semiconductor photocatalysts. Different reactor designs have been found to be suitable for photocatalytic degradation reactions in which immersion type photoreactor with the catalyst particles in the suspension have been found to yield a higher rate of degradation of the pollutants (Vinu and Madras 2010). We are using an immersion type photocatalytic reactor supplied by Lelesil innovative systems which consists of a jacketed quartz tube that houses the UV radiation source at 250 W. The mixture of catalyst and organic pollutant is taken in the outer jacketed reaction beaker made of borosilicate glass. Coldwater is circulated to avoid the thermal effects for the degradation of the pollutants.

1.3.5 Modification Routes for Extending Visible Light Response of Catalysts

As we know that nearly 43 % of the solar irradiation energy corresponds to visible light and nearly 7 % of the energy corresponds to UV light. Undeniably, the first generation TiO_2 is a prominent photocatalyst in the UV region, due to its wide band gap of 3.2 eV which hampers its use in the visible range. Therefore, there is an imperative need for the extension of visible light response of wide band gap photocatalysts.

1.3.5.1 Doping

Doping plays an important role in extending the visible light response of wide-gap semiconductors, and in particular non-metal doping has been extensively studied. Non-metal doping could retain the inherent surface properties of the photocatalyst at the atomic scale (Valentin et al. 2013).

The dopant states are generally located slightly above the valence band maximum making the photogenerated holes in these states suitable for various

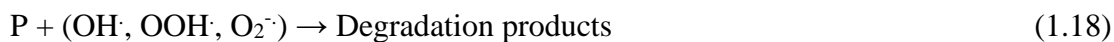
photoinduced oxidation reactions (Ong et al. 2014). Nitrogen doping has been intensively studied amongst all the non-metal dopants. Zou et al. (2012) prepared nitrogen-doped SrTiO₃ by template-free methodology using glycine as a pore creator as well as a nitrogen source. Their results indicated that N-doped SrTiO₃ exhibited enhanced photocatalytic activity which could be attributed to the enhanced visible light absorption due to the contribution of nitrogen dopants and oxygen vacancies. The enhanced photocatalytic activity could also be attributed to the mesoporous structure and higher surface area.

Modification of photocatalysts with noble and other metals such as Pt, Au, Ag, Rh, Ru, Pb, Pd, Bi, Cr, Co, Zn, Mn, Cu, V, Ni, and Sn have also enabled the extension of the spectral response of photocatalysts well into the visible region (Pelaez et al. 2012). However few reports indicated that the doped metal ions may serve as recombination sites for the photo-induced holes and electrons thereby suppressing the photocatalytic efficiency (Li et al. 2014). Codoping with two or more metals or nonmetal atoms is highly advantageous in maintaining the charge neutrality and can suppress defect formation thereby enhancing the mobility of the charge carrier, enhancing the visible light activity, and reducing the charge recombination, which will be highly beneficial for various photo induced redox reactions (Chen et al. 2020).

1.3.5.2 Dye Sensitization

Dye photo sensitization has been found to be one of the most promising methods to extend the optical response in to the visible region of the solar spectrum. The photocatalytic mechanism of the dye sensitized photocatalyst under visible light was proposed as follows (Zhao et al. 2005):





When dye absorbs visible light, it will be excited to the excited state (D^*) from the ground state (D). When the LUMO of the dye matches with the CB of the semiconductor, the excited dye molecule will be converted to a semi-oxidised radical cation (D^+) by injecting an electron into the CB of the semiconductor. The pictorial representation of the photocatalytic mechanism of the dye-sensitized photocatalyst under visible light is shown in Figure 1.2.

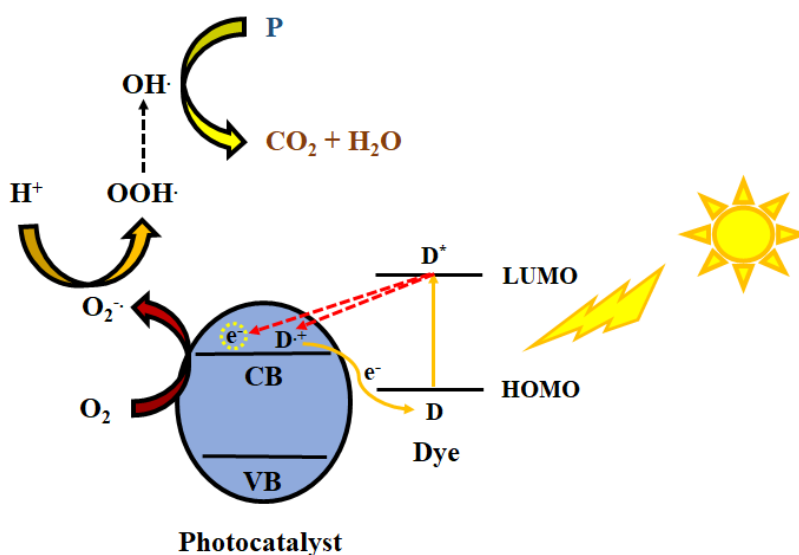


Figure 1.2 Photocatalytic mechanism of the dye-sensitized photocatalyst under visible light.

1.3.5.3 Heterostructure

Heterostructured semiconductor is another promising strategy for extending the optical response of wide band gap semiconductors in the visible region of the solar spectrum. When a wide gap semiconductor is composited with a narrow band gap semiconductor (which can absorb visible light) with a more negative CB level as compared to a wide band gap semiconductor, photogenerated electrons from the narrow band gap semiconductor will be injected into the CB of the wide band gap

semiconductor thereby suppressing the charge recombination (Li et al. 2021). The pictorial representation of the photocatalytic mechanism of the heterostructured semiconductor under visible light is shown in Figure 1.3.

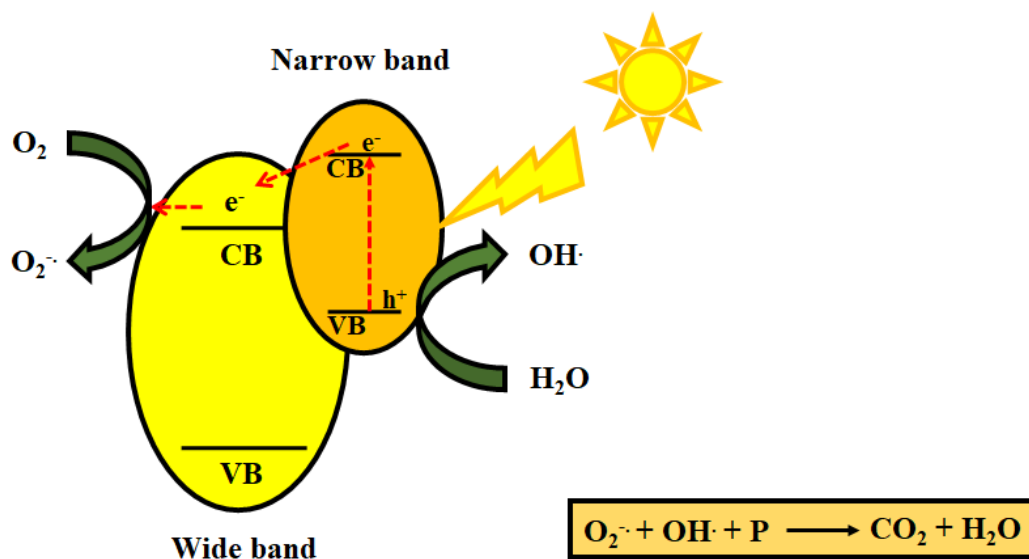


Figure 1.3 Photocatalytic mechanism of the heterostructured semiconductor under visible light.

1.3.5.4 Coupled with π -Conjugated Structure

Semiconductor photocatalyst coupled with a π -conjugated structural material like graphene has been found to be an effective strategy for enhancing visible light activity. When graphene is composited with a wide bandgap semiconductor, the interaction between the graphene and the semiconductor narrows down the band gap, thus improving the visible light absorption property and also suppressing the charge recombination (Sekar et al. 2021). The pictorial representation of the photocatalytic mechanism of the semiconductor coupled with graphene under visible light is shown in Figure 1.4.

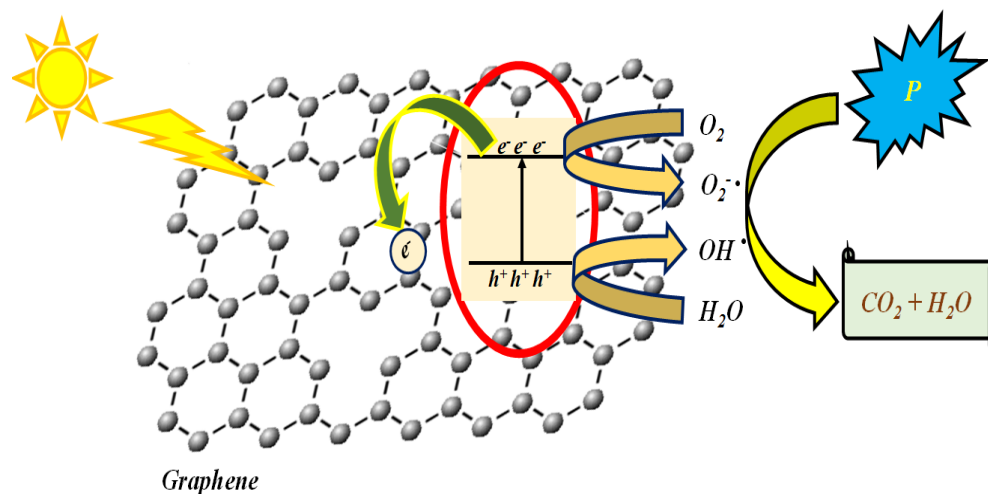


Figure 1.4 Photocatalytic mechanism of the semiconductor coupled with graphene under visible light.

1.4 A REVIEW OF LITERATURE

A review of the literature was carried out to understand the recent developments in the area of doped ATiO_3 and graphene-based ATiO_3 nanocomposites for photocatalysis. Various synthetic methodologies used for the synthesis of graphene, doped ATiO_3 , and graphene-based nanocomposites in the recent past have been discussed below, followed by a brief account on their applications in photocatalysis.

1.4.1 Graphene

Graphene is an attractive candidate in several industries due to its excellent electrical conductivity, high surface area, excellent thermal conductivity, high mechanical strength, high chemical stability, and excellent optical transparency. But producing high-quality sheets in a large scale is still a challenge. Mechanical exfoliation, being a top-down approach is the first method used for the synthesis of single-layer graphene, where a small mass of graphite is repeatedly peeled out with the help of scotch tape (Novoselov et al. 2004). However, the yield was reported to be too low. CVD being a bottom-up approach is one of the most popular methods utilized for the large-scale synthesis of single or few-layer graphene, where the activation of gaseous reactants takes place followed by the subsequent chemical reaction and followed by the formation of a stable solid coating on a suitable substrate

(Munoz and Gomez-Aleixandre 2013). Oxidative exfoliation-reduction being a top-down approach is one of the most popular methods employed in the synthesis of graphene sheets due to its high yield and low production cost (Lee et al. 2019). In this method, graphite is oxidatively exfoliated to get GO and is subjected to reduction to give RGO. The Hummers method is widely used for the synthesis of GO as it is a safe and quick process (Hummers and Offeman 1958). Chemical reduction, thermal reduction, hydrothermal reduction, and electrochemical reduction are the common reduction techniques utilized for the reduction of GO to graphene sheets, and other reduction techniques include photocatalytic, microwave, and photothermal methods.

Yu et al. (2016) reported an economical, fast, scalable, and eco-friendly NaNO_3 -free Hummers method by partly replacing KMnO_4 with K_2FeO_4 of higher oxidizability at low temperature to enhance the pre-oxidation and intercalation of graphite. This improved method also reduces the amount of concentrated H_2SO_4 . The derived graphene aerogel was found to be an excellent candidate for supercapacitor application.

Xing et al. (2017) synthesized graphene nanosheets from humic acid by preliminary carbonization followed by oxidation-exfoliation-thermal reduction. The obtained graphene sheets exhibited a high specific surface area ($495 \text{ m}^2\text{g}^{-1}$), large pore volume ($2.987 \text{ cm}^3\text{g}^{-1}$), and interconnected mesoporous structure with uniform oxygen-containing functionalities. The synthesized graphene nanosheets exhibited high specific capacitance, excellent rate capability, outstanding cyclic performance, and desirable energy density with low resistance value in aqueous electrolytes.

Pie et al. (2018) reported a safe, scalable, ultrafast, and green method for the synthesis of GO sheets by electrolytic oxidation of graphite by using commercial flexible graphite paper as a raw material. In this method, two electrochemical processes were involved namely electrochemical intercalation and electrochemical oxidation-exfoliation. They found that the pre-intercalation of graphite inhibits the electrocatalytic oxygen evolution reaction of water at a higher voltage which enables the oxidation of graphene lattice within a few seconds. GO obtained in this method exhibited similar chemical composition and properties as achieved from the traditional Hummers method and this method enables continuous production and easy control on the number of layers and oxidation degree of GO sheets.

Xing et al. (2019) reported a cost-effective and eco-friendly method for the preparation of porous graphene sheets via graphitization followed by liquid oxidation-rapid thermal reduction by using anthracite as a precursor. The prepared porous graphene exhibited a hierarchical micro-meso-macroporous structure, high specific surface area ($640 \text{ m}^2\text{g}^{-1}$), large pore volume ($3.792 \text{ cm}^3\text{g}^{-1}$), with an enormous amount of defects and nanopores which will be helpful in providing sufficient active sites for lithium ions storage and enable quick transport of lithium ions and electrons. The synthesized porous graphene exhibited a high reversible capacity of 770 mAhg^{-1} at a current density of 0.1 C and possessed an outstanding rate capability with desirable capacities even at high current densities. The synthesized porous graphene also exhibited superior cyclic performance of 98.0% of the initial capacitance retention even after 110 cycles.

Coros et al. (2020) synthesized RGO by a simple, eco-friendly, and cost-effective technique. They also studied the structural properties of the synthesized RGO by using XRD, UV-Visible, Raman, TGA, and XPS analysis. At a temperature of $400 \text{ }^\circ\text{C}$, the highest percent (82%) of few layers graphene is obtained. The material exhibited superior removal capacity for atenolol (61% in 30 minutes).

Ma et al. (2021) synthesized porous RGO by a novel and facile microwave-assisted one-pot method using the ZnO as the template with highly interconnected porous channels and without any restacking between the layers. The HCl solution act as the etching agent. The presence of open-macroscopic channels in porous RGO reduces the ion-transfer resistance and provide satisfactory ion-diffusion and ion-accessible surface areas which lead to higher electrochemical performance.

1.4.2 Perovskite Titanates

Kawasaki et al. (2012) investigated the occupied and unoccupied in-gap electronic states of Rh-doped SrTiO_3 photocatalyst by X-ray emission spectroscopy and X-ray absorption spectroscopy. An unoccupied midgap Rh^{4+} acceptor state was found 1.5 eV below the conduction band minimum of SrTiO_3 . They also found that both Rh^{4+} and Rh^{3+} dopants possess an occupied donor level close to the valence band maximum of SrTiO_3 . First-principles calculations indicate the substitution of Rh at the Ti site and that Rh: SrTiO_3 has a p-type electronic structure. The Rh doping results in

a large decrease in band gap, making Rh: SrTiO₃ an attractive material under visible light for the H₂ evolution reaction.

Furuhashi et al. (2013) synthesized Rh and Sb co-doped photocatalyst by hydrothermal synthesis. The UV-visible absorption results indicated that doping Rh alone resulted in a mixture of Rh⁴⁺ and Rh³⁺. An equivalent amount of Sb was added to maintain the oxidation state of Rh as +3 due to the charge compensation. The doped and non-doped samples exhibited transient infrared absorption due to photoexcited electrons. Doping Rh alone caused the fastest absorbance decay, which could be due to the presence of Rh⁴⁺ as the recombination center and the absorbance decay was retarded in the presence of Sb. The synthesized photocatalyst was found to be highly efficient for overall water splitting.

Maeda (2014) synthesized rhodium-doped barium titanate (BaTiO₃:Rh) by the polymerized complex (PC) method. Their results indicated that the doping of Rh species into the lattice of BaTiO₃ resulted in the formation of new absorption bands in the visible light region. It was found that the BaTiO₃:Rh loaded with Pt as a hydrogen evolution promoter will be able to produce H₂ from water containing an electron donor such as methanol and iodide under visible light. It was also found that the Z-scheme water splitting could be achieved using Pt/BaTiO₃:Rh as a building block for H₂ evolution in combination with PtO_x-loaded WO₃ as an O₂ evolution photocatalyst in the presence of an IO₃⁻/I⁻ shuttle redox mediator under visible light irradiation. Photoelectrochemical analysis indicated that the BaTiO₃:Rh electrode exhibited cathodic photoresponse due to water reduction in a neutral aqueous Na₂SO₄ solution upon visible light.

Xian et al. (2014) synthesized SrTiO₃-graphene nanocomposite via photocatalytic reduction of GO by SrTiO₃ under UV irradiation. It was found that the band structure of SrTiO₃ in the composite was uninterrupted. The photocatalytic activity of the composite was enhanced as compared to bare SrTiO₃ for the degradation of acid orange 7 under UV light, which can be attributed to the reduced charge recombination. The effect of nitrogen, ethanol and KI on the photocatalytic efficiency of the SrTiO₃-graphene nanocomposite was studied. The photocatalytic efficiency was slightly reduced by purging nitrogen gas due to the removal of dissolved oxygen from the solution whereas the photocatalytic efficiency was

significantly reduced by the addition of ethanol (hydroxyl radical scavenger) and KI (hydroxyl radical scavenger as well as hole scavenger). Hence hydroxyl radicals and holes are suggested to be active species for the photocatalytic degradation of dye.

Xian et al. (2014) reported CaTiO₃-graphene composite for the photocatalytic degradation of methyl orange. The enhanced photocatalytic activity (98 % in 60 minutes) under UV irradiation was attributed to the effective suppression of photoinduced charges.

Modak and Ghosh (2015) studied the effect of La codoping on the geometric and electronic structure of Rh-doped SrTiO₃ using hybrid density functional theory towards hydrogen evolution. The electronic structure of Rh-doped SrTiO₃ was found to be strongly influenced by the presence of La. The localized mid-gap states were completely passivated upon the introduction of La to Rh-doped SrTiO₃ and hence responsible for the enhancement of photocatalytic activity. The presence of La not only minimizes the formation of a photochemically inert Rh⁴⁺ state but also minimizes oxygen vacancy formation.

Modak and Ghosh (2015) studied the role of F in improving the photoconversion efficiency of Rh-doped SrTiO₃. Doping with Rh reduces the band gap by introducing partially occupied and unoccupied states above the VB. These states may also act as recombination centers. Electronic structure calculation revealed that the unoccupied localized states of Rh-doped SrTiO₃ are completely passivated in the presence of F and thus reduces the rate of electron-hole recombination. The valance band maxima are elevated significantly, reducing the band gap to 2.50 eV which will enhance the visible light activity of SrTiO₃. It was found that the band structure of the codoped system is found to be strongly dependent on the ratio of the dopant elements. In the case of 1:2 (Rh, F)-codoped SrTiO₃, a clean band structure, with a significant reduction of band gap to 2.31 eV is observed. It was found that the relative positions of the band edges for both 1:1 and 1:2 (Rh, F)-codoped SrTiO₃ are favorable for overall water splitting.

Nishioka and Maeda (2015) synthesized rhodium-doped barium titanate (BaTiO₃:Rh) nanocrystals by a facile hydrothermal method followed by post-heating. It was found that the photocatalytic activity was mainly dependent on the various synthetic parameters such as precursor ratio, nature of TiO₂ precursor materials, and

post-heating conditions. These synthetic parameters have a considerable impact on crystallinity, the generation of Ba vacancies as well as the oxidation state of Rh in BaTiO₃:Rh. Their experimental results indicated that suppressing the generation of Ba vacancies during the synthetic process and improving the crystallinity can lead to enhancement in photocatalytic activity.

Wang et al. (2015) synthesized BaTiO₃-graphene nanocomposites with different weight ratios of GO by a facile one-pot hydrothermal approach. The as-prepared samples were characterized by various advanced characterization techniques. The photocatalytic activity of the BaTiO₃-graphene composite was found to be higher as compared to pure BaTiO₃ for the degradation of MB under visible light irradiation. It was suggested that graphene acts as an organic dye-like photosensitizer in the BaTiO₃-graphene nanocomposite which transforms the wide band gap BaTiO₃ semiconductor into visible light.

Kiss et al. (2017) synthesized nanostructured Rh-doped SrTiO₃ by a facile hydrothermal approach by avoiding high-temperature calcination and maintaining Rh in the photocatalytically active +3 oxidation state. The photocatalytic activity of SrTiO₃ containing 5 at % Rh was found to be higher for the degradation of methyl orange and E. coli under visible light which could be attributed to the high surface area and the efficient visible light absorption (>420 nm) caused by the presence of Rh³⁺ species.

Kumar et al. (2017) reported nitrogen-doped CaTiO₃-reduced graphene oxide composite for the photocatalytic degradation of MB and thiabendazole. The improved activity (95 % of MB and 90 % of thiabendazole in 180 minutes) under visible light was due to the excellent adsorption capacity and suppressed charge recombination.

He et al. (2018) synthesized core-shell SrTiO₃/graphene composite by the chemical vapour deposition technique. The composite with CH₄ flux of 5 sccm exhibited enhanced photocatalytic activity as compared to bare SrTiO₃ towards the degradation of Rhodamine B under UV irradiation. It was found that the formation of the Ti-C bond is highly beneficial for the effectual transport of electrons from SrTiO₃ to graphene sheets and thus suppressing the charge recombination also it was claimed that the core-shell structure successfully avoids the restacking of graphene sheets, thus

leading to the efficient absorption of light and higher interface area for charge carrier separation.

Zhao et al. (2018) prepared the core-shell BaTiO₃ nanoparticles and GO nanosheets by a sol-precipitation process and the Hummers' method, respectively. BaTiO₃/GO nanocomposites were successfully prepared via the freeze-drying method. The BaTiO₃/GO nanocomposites promoted the formation of steady architecture and enhanced the active reaction sites for photo-degradation. The nanocomposite with 80 % GO exhibited enhanced photocatalytic performance towards the degradation of MB (67 % in 150 minutes) which was mainly attributed to the appropriate energy band structure and effective absorption.

Ahmadi et al. (2019) synthesized SrTiO₃/reduced-graphene oxide (STO/rGO) nanocomposite by using the photocatalytic reduction method. The as-prepared STO/rGO nanocomposite exhibited enhanced photocatalytic efficiency as compared to bare STO towards the degradation of Rhodamine B under visible light. The enhanced photocatalytic activity of STO/rGO could be attributed to the efficient transfer of photoexcited electrons and holes in the STO/rGO nanocomposite. Holes and hydroxyl radicals were found to be the main active species for the degradation of Rhodamine B. The band structure of STO/rGO nanocomposite is almost unchanged as compared to pure STO. The higher PL intensities of the STO/rGO nanocomposite as compared to bare STO could be attributed to the higher recombination rate of photoinduced electrons in the CB of rGO and CB of STO, pointing that the holes in the VB of STO with more positive potential can take part in the oxidation reactions to produce hydroxyl radicals. They also proposed the possible photocatalytic mechanism, in which rGO get photoexcited (as a sensitizer) to produce electron and hole pairs. These photogenerated electrons on the rGO, can be transferred to the CB of STO as a result, rGO gets a positive charge which removes an electron from the VB of the STO, and the remained holes on the VB of STO can react with water molecules or directly with Rhodamine B dye molecules to generate the hydroxyl radicals.

Hoang et al. (2019) synthesized Mo, V-codoped SrTiO₃ by a sol-gel method. It was found that the reduction in the band gap energy from 3.24 eV (pure SrTiO₃) to 2.64 eV for co-doped SrTiO₃ could be attributed to the creation of impurity levels

caused by the Mo^{6+} and V^{5+} cations. The co-doped SrTiO_3 exhibited higher photocatalytic degradation towards MB as compared to undoped and mono-doped SrTiO_3 in the visible region, which can be attributed to the reduced band gap and reduced recombination rate of photoinduced charges caused by the dopants Mo^{6+} and V^{5+} cations.

Mengting et al. (2019) investigated the photodegradation of MB by BaTiO_3/GO composite under UV–visible irradiation. They also found that the photodegradation of MB by BaTiO_3/GO composite takes place via hydroxyl radicals. The composite with a 1:2 ratio of BaTiO_3/GO (0.5 g/L catalyst dose, pH 9.0, and 5 mg/L of MB concentration) exhibited the highest MB degradation of 95 % in 3 hours under UV-visible irradiation.

Yan et al. (2019) synthesized CaTiO_3 nanocuboids by a hydrothermal route using P25 as the titanium source. Au nanoparticles were uniformly decorated on the CaTiO_3 nanocuboids by a photocatalytic reduction of HAuCl_4 solution. Compared to pure CaTiO_3 nanocuboids, the $\text{Au}@\text{CaTiO}_3$ composites exhibited enhanced visible-light absorption, increased photocurrent density, suppressed PL intensity, as well as enhanced photocatalytic performance for the degradation of Rhodamine B under the different light sources (simulated sunlight, UV light, and visible light). The photocatalytic activity of 4.3 % $\text{Au}@\text{CaTiO}_3$ (99.6 % of Rhodamine B under simulated sunlight) was found to be higher than that of bare CaTiO_3 nanocuboids. The enhanced photocatalytic activity of the composites could be attributed to the efficient separation of photogenerated e^-/h^+ pairs due to the electron transfer from CaTiO_3 nanocuboids to Au nanoparticles and enhanced visible-light absorption due to the localized surface plasmon resonance effect of Au nanoparticles. The electromagnetic field caused by the localized surface plasmon resonance effect of Au nanoparticles could trigger the generation and separation of electron-hole pairs in CaTiO_3 . Hydroxyl radicals and holes were found to be the major active species for photocatalysis.

Chen et al. (2020) synthesized Na^+ co-doped $\text{CaTiO}_3:\text{Eu}^{3+}$ through the solution combustion method. It was found that doping of Na^+ and Eu^{3+} enlarged the absorption region and reduction in the band gap energy of pure CaTiO_3 . It was observed that the greatest photocatalytic property and the degradation rate of MB (96.2 % in 300 minutes) with $\text{CaTiO}_3:0.5\% \text{Eu}^{3+}, 0.5\% \text{Na}^+$ sample under UV light was due to the

reduction in band gap and grain size. It was also found that codoping restrained the formation of Ca^{2+} ions and oxygen defects thus improving the photocatalytic activity.

Cui et al. (2022) synthesized porous CQDs-doped SrTiO_3 /graphene material (CSG) by the sol-gel carbonized propagation method. The best sample CSG-5 (80 mL ethanol) showed the highest degradation rate for MB (94 %) at a dose of 1.5 mg L^{-1} . The best photocatalytic performance under visible light can be attributed to the support of graphene and the formation of SrTiO_3 and CQDs heterojunctions, which facilitate the separation of photoinduced charges. Acidic media and appropriate amounts of NO_3^- can promote the degradation of MB. The trapping experiment and ESR results indicated that holes and superoxide anion radicals are the main active species. The CSG-5 catalyst showed excellent reusability and stability after 5 cycles.

1.5 PROBLEM IDENTIFICATION

Heterogeneous photocatalysis with the aid of different semiconductors has been receiving immense interest in the research community for their gigantic potential in the treatment of recalcitrant pollutants in water, production of hydrogen via water splitting due to their economic, environmentally benign, and alignment with the “zero” waste scheme. Perovskite alkaline earth titanates like SrTiO_3 , BaTiO_3 , and CaTiO_3 have been utilized as a photocatalyst due to their ease of preparation, chemical stability, biocompatibility, and resistance to photo corrosion. However, their photocatalytic activity is strictly restricted to the UV region of the solar spectrum due to the wide band gap of 3.2 eV, and also, they suffer from high recombination rates of photoinduced charges which will limit their use in practical applications. There are several strategies for improving the photocatalytic activity of perovskite alkaline earth titanates such as doping with metals or non-metals, formation of heterostructures, coupled with π -conjugated structures like graphene, and so on (Zhou et al. 2022, Wu et al. 2020, Kumar et al. 2017).

Doping with metals and non-metals or tuning the cation ratio has been found to be an effective strategy in extending the optical response of perovskite titanates well into the visible region as there are three possible sites for doping. Though doping seems to be a promising strategy, it is also known to introduce mid-gap states acting as recombination centers which will diminish the photocatalytic efficiency and also it

should be noted that the oxidation state of a metal dopant has a significant effect on the modification of the electronic structure by the formation of donor and acceptor levels as well as suppressing the electron-hole recombination (Saad et al. 2018). Thus, it is necessary to design the synthetic technique with appropriate dopants to get better photocatalytic efficiency.

Semiconductor photocatalyst coupled with a π -conjugated structural material like graphene has been found to be a promising method for enhancing visible light activity. When graphene was composited with a wide band gap semiconductor, the interaction between graphene and the semiconductor narrows down the band gap, thus improving the visible light absorption property, enhancing the surface area, enhancing the charge transport, and suppressing the charge recombination.

Porous graphene consists of few-layered planar graphene sheets that possess large surface area, excellent hydrophobicity, excellent optical transparency, high chemical stability, and structural stability. Such porous structures promote faster adsorption and desorption of contaminants during the photocatalytic reaction. However, the nature of chemical bonding between the semiconductor and the graphene plays a vital role in photo-induced interfacial electron transfer (He et al. 2018). Therefore, the development of environmentally benign photocatalysts to overcome these problems is of great importance and a challenge in the current scenario.

1.6 SCOPE AND OBJECTIVES OF THE WORK

Perovskite alkaline earth titanates, MTiO_3 ($M = \text{Ba, Ca, Sr}$) have attracted extensive interest because of their widespread applications in the photocatalytic degradation of organics, water splitting owing to their high chemical stability, good biocompatibility, and resistance towards photo corrosion. However, due to their wide band gap, their photocatalytic activity is hampered in the visible light region of the solar spectrum. Hence, it would be worthwhile to work on these MTiO_3 to enhance their catalytic activity.

Generally, for heterogeneous photocatalysts, the crystal phase, particle size, surface area, crystallinity, morphology, and photocatalytic activity can be well-tuned

by tailoring various processing parameters such as surfactants, reaction temperature, reaction time, and solvents. As a result, a similar strategy can be used for MTiO_3 .

Doping has been found to be a promising strategy in extending the visible light response of MTiO_3 as there are three possible sites for doping. It is well known that the incorporation of noble and other metals such as Ag, Bi, Co, Cr, Fe, Ir, La, Mn, Nb, Pb, Pd, Pt, Rh, Ru, Sb, and Zn have enabled the efficient harvesting of the solar energy. However few reports indicated that the doped metal ions may act as recombination centers for the photo-induced charges, thereby suppressing the photocatalytic efficiency. Thus, it is necessary to design the synthetic technique with appropriate dopants by avoiding the formation of the so-called recombination centers to get better photocatalytic efficiency.

Graphene can be coupled with perovskite titanates to enhance photocatalytic activity due to its excellent transparency, superior electron conductivity, electron mobility, high specific surface area, and high chemical stability. Graphene sheets act as an electron transfer channel for reducing the recombination of the photoinduced charges and leading to improved photoconversion efficiency of the photocatalytic materials and also enlarging the photocatalytic reaction space.

In this view and based on the literature studies, the following objectives have been proposed for the present work.

- To synthesize the perovskite structure compounds of general formula MTiO_3 (where, $M = \text{Ba, Sr, Ca}$) and metal ion-doped MTiO_3 by hydrothermal/solvothermal method.
- To synthesize MTiO_3 -graphene composite by a facile solvothermal approach.
- To characterize the synthesized materials by diffraction, microscopic and spectroscopic techniques.
- To study the photocatalytic activity by taking MB as a target pollutant under visible light irradiation.

1.7 THESIS WORK

The present thesis reports the successful synthesis of seven different series of photocatalysts using a solvothermal or hydrothermal approach. All the synthesized

materials were thoroughly characterized for their elemental composition, structural, morphological, and optical properties with the help of various characterization techniques such as XRD, FESEM, TEM, HRTEM, Raman Spectroscopy, XPS, BET Method, DRS, and PL Spectroscopy. Thereafter, the photocatalytic efficiencies of the synthesized materials were evaluated by taking MB as a target pollutant under visible light.

The contents presented in the thesis have been broadly categorized into nine chapters with several sections in each chapter.

Chapter 1 gives a brief introduction to the basic concepts of the study carried out. It also gives a brief outline of the relevant works in the literature which focus on graphene, perovskite titanate, metal-doped perovskite titanate, graphene-based composites, their synthetic methods, and photocatalytic applications along with the scope and objectives of the present research work.

Chapter 2, Chapter 3 and Chapter 4 deals with the solvothermal synthesis of Rh-doped SrTiO₃ nanoparticles, V-doped SrTiO₃ nanoparticles and porous graphene-SrTiO₃ nanocomposite, respectively and the study of their structure, morphology, optical property, and photocatalytic activity.

Chapter 5 and Chapter 6 deals with the hydrothermal synthesis of Rh-doped BaTiO₃ nanoparticles and solvothermal synthesis of porous graphene-BaTiO₃ nanocomposite, respectively and the study of their structure, morphology, optical property, and photocatalytic activity.

Chapter 7 and Chapter 8 deals with the solvothermal synthesis of V-doped CaTiO₃ nanoparticles and porous graphene-CaTiO₃ nanocomposite, respectively and the study of their structure, morphology, optical property, and photocatalytic activity.

Chapter 9 deals with the summary of the work presented in the thesis along with important conclusions drawn from the study. The results of the research work presented in the thesis are also compared with the reported literature. The scope for further research has also been included in this chapter.

References used have been listed at the end.

CHAPTER 2

SOLVOTHERMAL SYNTHESIS OF RHODIUM-DOPED STRONTIUM TITANATE FOR PHOTOCATALYTIC APPLICATION

Chapter 2 presents and discusses the synthesis and photocatalytic activity of Rh-doped SrTiO₃ by a solvothermal approach.

2.1 INTRODUCTION

Various elements such as Ag, Bi, Co, Cr, Fe, Ir, La, Mn, Nb, Pb, Pd, Pt, Rh, Ru, Sb, and Zn have been utilized for Sr or/and Ti site doping and co-doping, while B, N, F have been used for substitution at O site either alone or accompanied by metal doping in Sr/Ti sites (Zhang et al. 2016, Irie et al. 2007, Lv et al. 2015, Yu et al. 2014, Jiao et al. 2013, Tonda et al. 2014, Ouyang et al. 2012, Xie et al. 2008, Xue et al. 2017, Kawasaki et al. 2014, Zhou et al. 2011, Modak and Ghosh 2015, Modak and Ghosh 2015, Zou et al. 2012). Among these, Rh-doped SrTiO₃ has attracted significant attention due to its absorption in the visible region (Modak and Ghosh 2015, Iwashina and Kudo 2011, Kawasaki et al. 2012, Furuhashi et al. 2013, Chen et al. 2012, Kiss et al. 2017). When Rh is doped into SrTiO₃ both Rh³⁺ and Rh⁴⁺ exist in the lattice. Though Rh doping decreases the band gap of the material due to Rh³⁺ states acting as donor levels, it suffers from the drawback that acceptor states get formed in the mid-gap region due to the presence of Rh⁴⁺ states. Doping Rh by maintaining it in +3 state, by avoiding the formation of photocatalytically inactive +4 state has become a challenge in the synthesis of Rh doped SrTiO₃.

In this chapter, for the first time, the synthesis of Rh-doped SrTiO₃ nanoparticles by a facile one-pot solvothermal method by avoiding high-temperature calcination is reported. The photocatalytic activity of Rh-doped SrTiO₃ nanoparticles is evaluated by taking MB as a target pollutant.

2.2 EXPERIMENTAL SECTION

2.2.1 Synthesis

All chemicals were of analytical grade and were used as procured (Sigma Aldrich) without any purification. Rh-doped SrTiO₃ with varying percentages of Rh was synthesized as follows: 1.47 mL of titanium(IV) isopropoxide and rhodium (III) chloride were dissolved in 10 mL of 2-propanol which was labeled as solution A. An appropriate amount of strontium nitrate was dissolved in 10 mL of 2 M KOH which was labeled as solution B. Solution A was continuously stirred, as solution B was added dropwise to it. The resulting mixture was transferred to an autoclave and heated

in an oven at 200 °C for 4 hours. The obtained precipitate was first purified by washing with 1 M acetic acid and water and then dried in an oven at 70 °C for 8 hours. The products finally obtained by taking 0.1, 0.5, 1.0, and 3.0 mole % of Rh precursor were designated as 0.1 Rh, 0.5 Rh, 1.0 Rh, and 3.0 Rh respectively.

2.2.2 Characterization

The crystallographic structures of the as-synthesized catalysts were analyzed using a powder X-ray diffractometer (Rigaku Miniflex 600) with monochromatic Cu- K_{α} radiation ($\lambda = 0.154$ nm) at a scan rate of 2° per minute in the range of 20° - 80°. Kratos XSAM800 spectrometer equipped with an Al K_{α} source was used to record XPS. The morphological features of the synthesized catalysts were analyzed using a field emission scanning electron microscope (Carl Zeiss Ultra 55) and transmission electron microscope (Fie Tecnai G2). DR spectra were taken using a UV-visible DR spectrometer (DR SPECORD S600 Analytic Jena) and the PL spectra were obtained using a HORIBA Jobin Yvon fluorescence spectrometer at room temperature.

2.2.3 Determination of Photocatalytic Activity

The photocatalytic studies were carried out using a reactor equipped with a high-pressure 250 W Hg vapor lamp acting as a visible light source ($\lambda=410-700$ nm). In a 500 mL pyrex glass beaker, 100 mL of a solution containing 1 mg of MB and 50 mg of the photocatalyst was magnetically stirred for 30 minutes to achieve adsorption-desorption equilibrium of the catalyst. Later, the visible light irradiated solution was drawn out at regular intervals in a quantity of 5 mL and centrifuged. The supernatant solution was subjected to DR analysis at 664 nm. Considering C_0 as the initial concentration of the solution and C as the concentration at different intervals of time, the percentage degradation of dye is given by equation 2.1.

$$\text{Degradation \%} = [(C_0 - C) / C_0] \times 100 \quad (2.1)$$

2.3 RESULTS AND DISCUSSION

2.3.1 XRD Analysis

The XRD patterns of the SrTiO₃ and Rh-doped SrTiO₃ (Figure 2.1 a) could be indexed to the cubic phase of SrTiO₃ with JCPDS card number 01-089-4934. The absence of impurity peaks indicates that Rh occupied the lattice sites of the host structure. The similarity of the patterns of doped samples with that of pristine

indicates that the overall crystal structure was not much affected by the doping in the concentration range studied. It was observed that (110) peaks appearing in the 2θ range of $32^\circ - 32.5^\circ$ of the doped samples (Figure 2.1 b) shifted towards higher θ values which caused a decrease in the lattice parameter from 3.971 \AA to 3.941 \AA . This could be a consequence of Rh substituting Sr as the ionic radius of Rh^{3+} (0.067 nm) is smaller than Sr^{2+} (0.118 nm). Rh replacing Ti would have increased the lattice constant as Ti^{4+} (0.061 nm) is smaller in size.

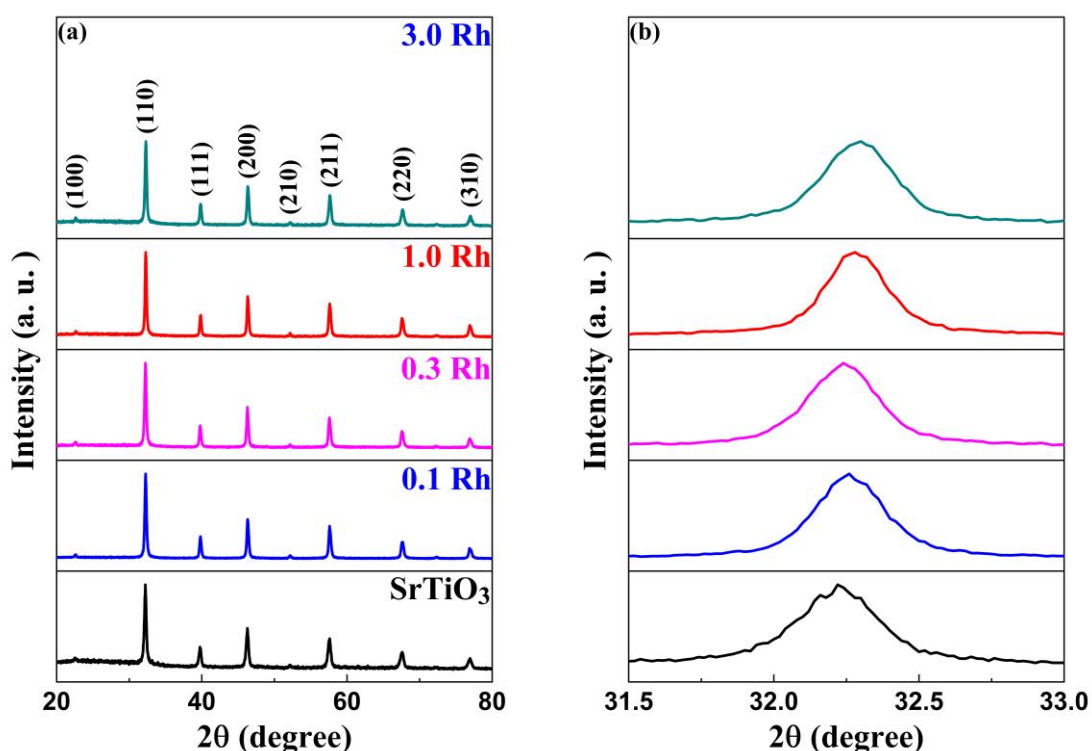


Figure 2.1 (a) XRD patterns as a function of doping concentrations of Rh and (b) diffraction peaks of (110) planes in the range of $2\theta = 31.5^\circ - 33^\circ$.

2.3.2 FESEM, EDS and TEM Analysis

The FESEM image of the 1.0 Rh sample (Figure 2.2 a) revealed numerous irregular spherical particles which are highly porous. Some broken spheres indicate the hollow nature of the material (circled yellow). Efficient photocatalysis requires a large contact area between the catalyst material and the reactant species, in addition to visible light absorption. Spherical particle is known to provide high surface area and in addition to it, the porous nature of the doped samples with low density offers large interaction frequency and high-speed molecular transport. EDX spectrum indicated

the presence of Sr, Ti, O, and Rh as elements (inset of 2.2 a). TEM image (Figure 2.2 b) reveals irregular spherical particles with their average size ranging from 70-150 nm.

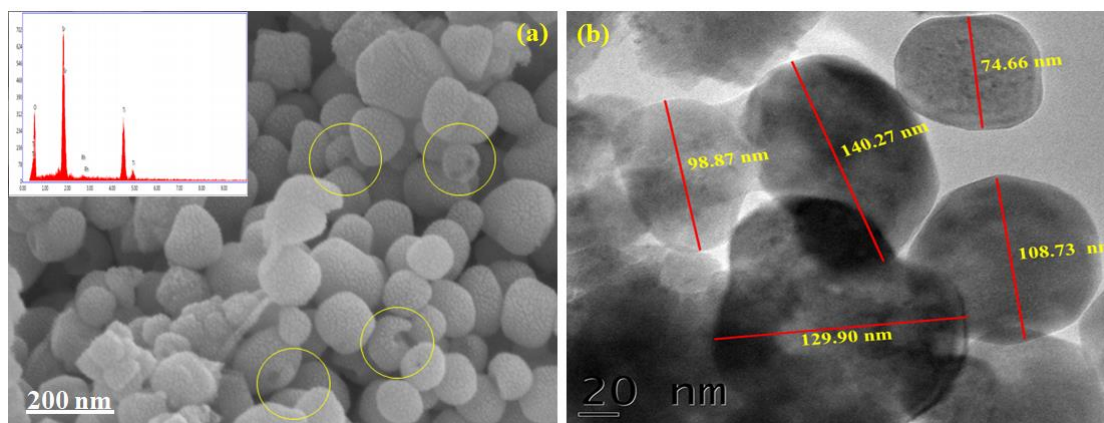


Figure 2.2 (a) FESEM image (EDX spectrum in the inset) and (b) TEM image of 1.0 Rh.

2.3.3 XPS Analysis

XPS was used to analyze the surface chemical composition of Rh-doped samples. Figure 2.3 shows the full range XPS survey plot of the as-synthesized 1.0 Rh sample. The deconvoluted spectra (Figure 2.4 a) show peaks with binding energies of 132.31 eV and 133.96 eV which can be attributed to Sr $3d_{5/2}$ and Sr $3d_{3/2}$ states, respectively. The peaks with binding energies of 457.5 eV and 463.3 eV (Figure 2.4 b) can be indexed to Ti $2p_{3/2}$ and Ti $2p_{1/2}$ states, respectively. These binding energy values correspond to Ti with the oxidation state of +4 in the perovskite structure of SrTiO_3 (Kiss et al. 2017). Figure 2.4 c shows the high-resolution O 1s spectrum which can be deconvoluted into two peaks of binding energies 528.83 eV and 530.75 eV which can be allotted to oxygen in the oxide lattice (O_L) and surface hydroxyl groups (O_{OH}) respectively. The peaks shown in Figure 2.4 d with binding energies of 308.5 eV and 313.1 eV can be indexed to Rh $3d_{5/2}$ and Rh $3d_{3/2}$ states, respectively corresponding to Rh with +3 oxidation states (Kiss et al. 2017). The absence of peaks corresponding to Rh^{4+} states indicate the successful incorporation of Rh into SrTiO_3 as Rh^{3+} and not as Rh^{4+} .

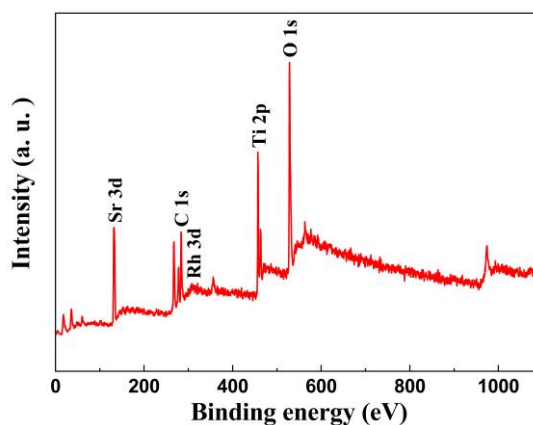


Figure 2.3 XPS survey spectrum of 1.0 Rh sample.

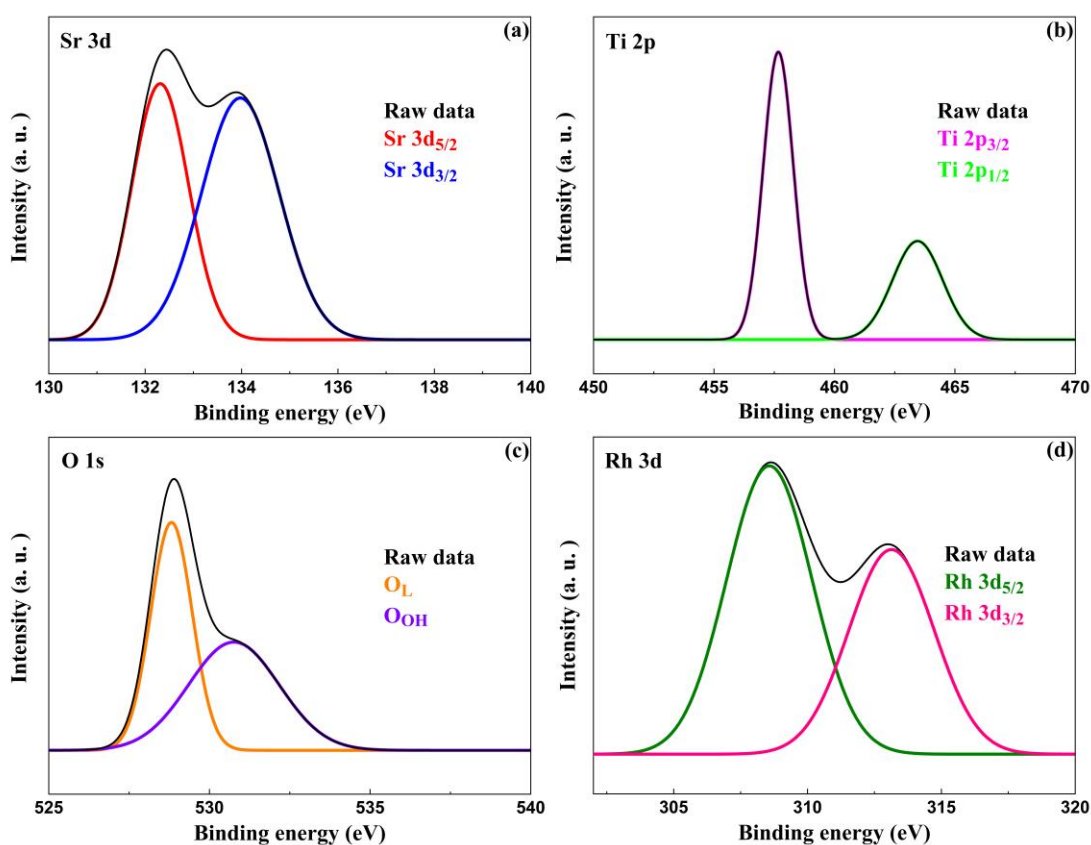


Figure 2.4 High-resolution XPS plot of (a) Sr 3d, (b) Ti 2p, (c) O 1s and (d) Rh 3d of 1.0 Rh sample.

2.3.4 Optical Absorbance Analysis

The DR spectra were measured as a function of wavelength from 250 nm to 700 nm (Figure 2.5 a) which shows an increase in the intensity of absorption from 400

to 500 nm range and thereafter a steady absorption with an increase in the concentration of Rh in SrTiO₃ (Tonda et al. 2014, Kiss et al. 2017). Further, the spectra did not show any presence of the characteristic absorption peak at 580 nm, caused by Rh⁴⁺, indicating the absence of this species in the sample (Kawasaki et al. 2012). Tauc relation was used to calculate the direct band gap of the samples using equation 2.2 (Sadiq et al. 2018, Mohamed et al. 2018).

$$(\alpha h\nu)^2 = K(h\nu - E_g) \quad (2.2)$$

where α is the absorption coefficient, E_g is the band gap energy of the semiconductor, K is a constant, and $h\nu$ is the photon energy. The band gap energies of SrTiO₃, 0.1 Rh, 0.5 Rh, 1.0 Rh and 3.0 Rh were found to be 3.24 eV, 3.01 eV, 2.55 eV, 2.42 eV and 2.0 eV, respectively (Figure 2.5 b). The absorption edge is seen to increase beyond 385 nm as the concentration of Rh is increased. The decrease in the band gap with the redshift in the absorption peak points to the formation of donor levels in the doped samples (Chen et al. 2012).

Figure 2.5 c shows the comparison of the PL spectra of SrTiO₃ and Rh-doped samples. The decrease in the intensity of the doped sample is due to the lower rate of recombination of electrons and holes due to the rapid rate of replenishment of electrons to the vacant site by the valence band. However, the PL intensity was found to increase beyond 1.0 Rh because dopants can become the recombination centers for the photoinduced charges at higher concentrations which will diminish the photocatalytic activity (Tian et al. 2009).

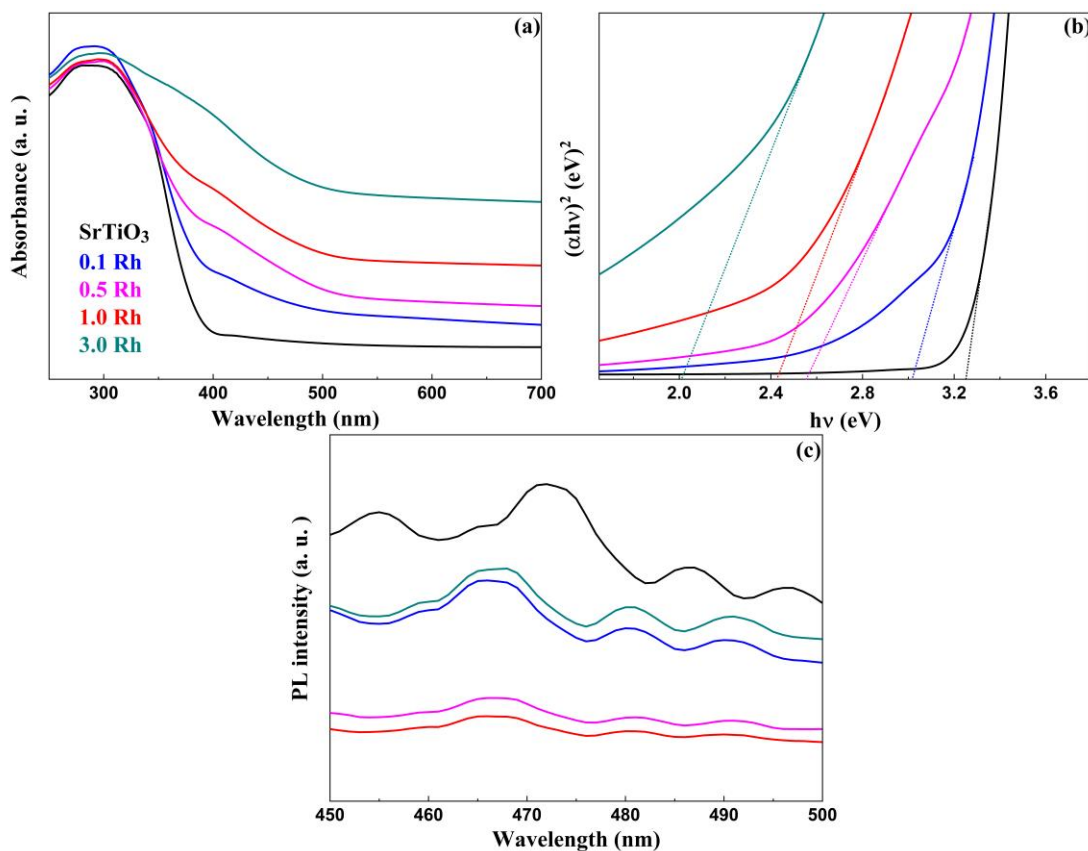


Figure 2.5 (a) UV-visible DR spectra, (b) Tauc plots and (c) PL spectra of SrTiO₃ and Rh doped SrTiO₃ samples.

2.3.5 Photocatalytic Activity

MB was chosen as the target moiety for testing the photocatalytic efficiency of Rh-doped samples. The percentage degradation of SrTiO₃, 0.1 Rh, 0.5 Rh, 1.0 Rh, and 3.0 Rh was found to be 20, 41.6, 65.2, 72.9, and 37.5, respectively (Figure 2.6 a). The results indicate that with an increase in Rh content the photocatalytic efficiency increases but beyond 1.0 Rh the photocatalytic activity decreases. This could be due to the fact that though the band gap decreases with an increase in the concentration of Rh, there is a possibility of the formation of recombination centers for photogenerated charge carriers which is supported by the results of PL.

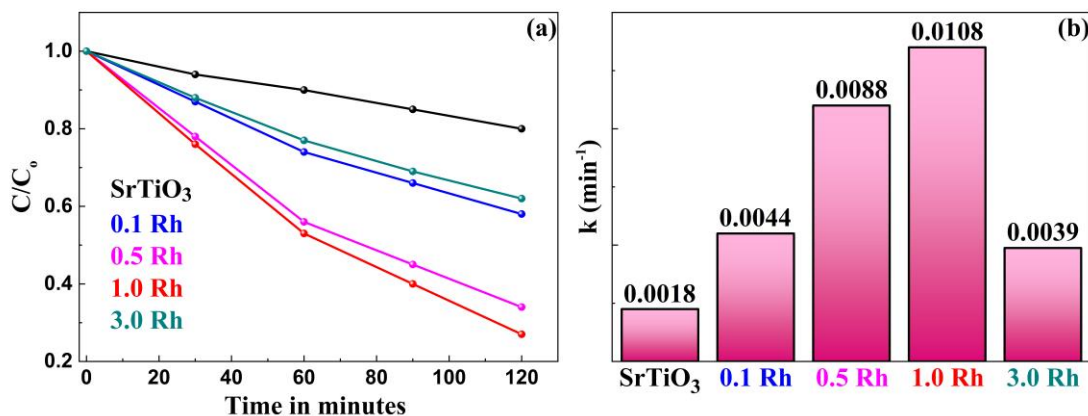


Figure 2.6 (a) Photocatalytic degradation curves and (b) rate constants for the photocatalytic degradation of MB by SrTiO₃ and doped samples.

The above photocatalysis reaction follows the first-order rate equation as given in equation 2.3 (Sadiq et al. 2018).

$$\ln(C/C_0) = -kt \quad (2.3)$$

where C₀ is the concentration of dye at time t=0, C is the concentration of the dye at irradiation time 't' and k is the first-order rate constant, given by the slope of the straight line. 1.0 Rh sample exhibited the highest rate constant of 0.0108 min⁻¹ compared to SrTiO₃, which showed a value of 0.0018 min⁻¹ (Figure 2.6 b). The catalyst showed only a slight decline in the activity even after 4 cycles indicating its stability and reusability for practical applications (Figure 2.7).

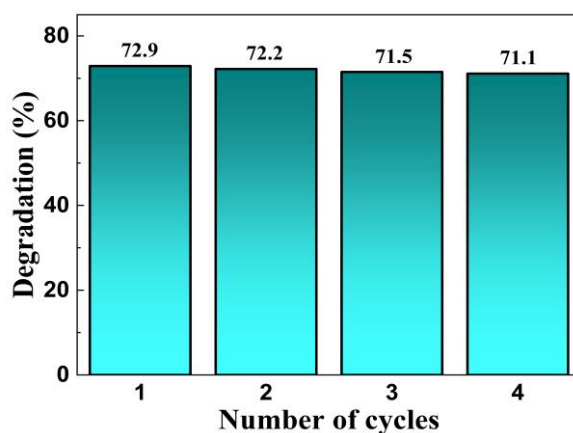


Figure 2.7 Cyclic stability of the synthesized 1.0 Rh.

Trapping experiments were carried out to determine the active species involved in photocatalytic degradation. The procedure followed was similar to the one used for degradation measurements as above but with the addition of different radical scavenging agents like benzoquinone (1 mM) as a superoxide anion radical ($O_2^{\cdot-}$) scavenger, potassium iodide (10 mM) as a hole (h^+) scavenger and isopropyl alcohol (10 mM) as a hydroxyl radical (OH^{\cdot}) scavenger. From Figure 2.8, we see that superoxide radical anions are not the major active species as the corresponding scavenger benzoquinone did not reduce the photocatalytic activity much. Whereas the addition of potassium iodide (hole scavenger) and isopropyl alcohol (OH^{\cdot} scavenger) reduced the photocatalytic activity appreciably. As a result, holes followed by hydroxyl radicals are considered to be the major active species for the effectual degradation of dye.

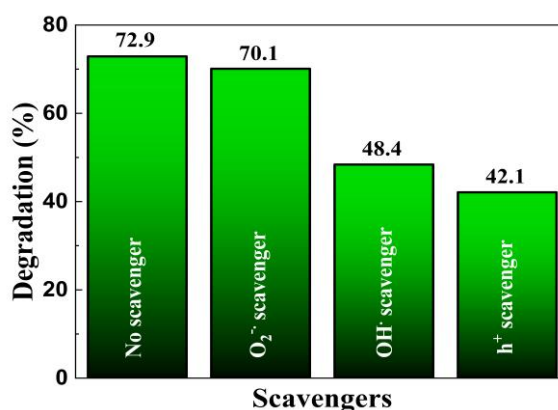


Figure 2.8 Effect of radical and hole scavengers on the photocatalytic degradation of MB by 1.0 Rh.

2.3.6 Photocatalytic Reaction Mechanism

The Rh-doped $SrTiO_3$ exhibited higher photocatalytic activity as compared to undoped $SrTiO_3$ due to the formation of donor levels by the Rh d orbitals which lie slightly above the valence band maximum, thus reducing the band gap. When the 1.0 Rh was exposed with the energy of photon equal to or greater than its band gap, an electron from the donor level is transferred to the CB and these electrons react with oxygen to produce superoxide radicals. Meanwhile, the formed holes either directly react with MB or with water molecules to produce hydroxyl radicals. These two

radicals are said to be active species for the effectual degradation of MB to harmless degradation products (Figure 2.9).

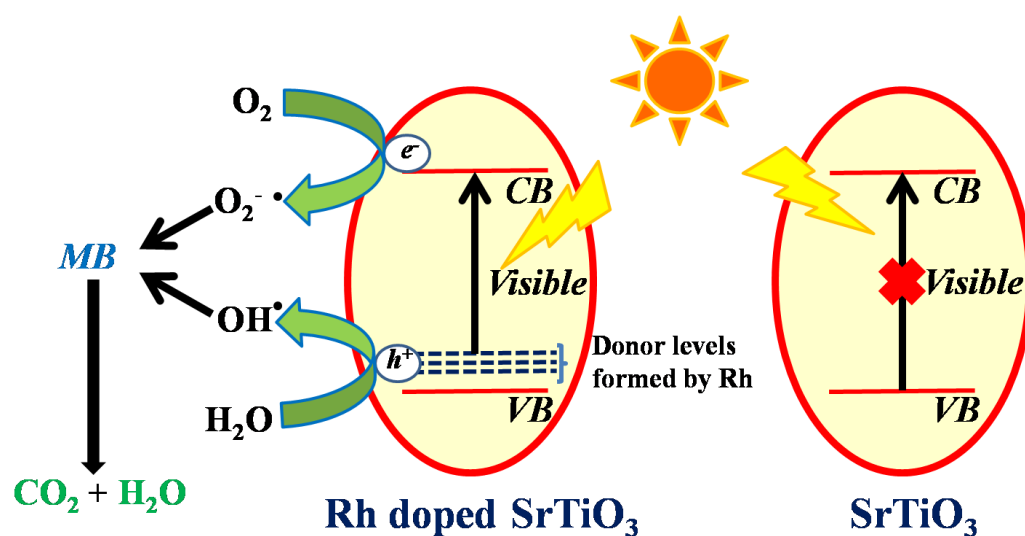


Figure 2.9 The photocatalytic mechanism of Rh-doped SrTiO₃ for the degradation of MB under visible light irradiation.

The activation energy for the photocatalytic degradation of MB can be calculated by using equation (2.4) (Kshirsagar and Khanna 2019, Jaihindh et al. 2019).

$$\log k = -E_a/2.303RT \quad (2.4)$$

where k is the rate constant of photocatalytic degradation, E_a is the energy of activation, R is the gas constant ($R=8.314 \text{ J/K}$) and T is the temperature in the kelvin (K) scale taken as 300 K in the current study.

The other thermodynamic parameters such as, the free energy of activation (ΔG^\ddagger), enthalpy of activation (ΔH^\ddagger), and entropy of activation (ΔS^\ddagger) were computed by employing the activation complex theory (ACT) and Eyring equation (Table 2.1).

$$\ln k = \ln (k_B T/h) - \Delta H^\ddagger/RT + \Delta S^\ddagger/R \quad (2.5)$$

$$\Delta H^\ddagger = E_a - RT \quad (2.6)$$

$$\Delta G^\ddagger = \Delta H^\ddagger - T \Delta S^\ddagger \quad (2.7)$$

where k_B is the Boltzmann's constant (1.3805×10^{-23} J/K) and h is the Planck's constant (6.6261×10^{-34} Js).

Table 2.1 Thermodynamic parameters of the SrTiO₃ and Rh doped SrTiO₃ samples

Sample	E _a (kJ/mol)	ΔH [#] (kJ/mol)	ΔS [#] (kJ/mol)	ΔG [#] (kJ/mol)
SrTiO ₃	15.7	13.2	-0.25	89.3
0.1 Rh	13.5	11.0	-0.25	87.0
0.5 Rh	11.8	9.3	-0.25	85.2
1.0 Rh	11.2	8.8	-0.25	84.7
3.0 Rh	13.8	11.3	-0.25	87.3
Without catalyst	17.7	15.2	-0.25	91.2

From the values tabulated, it is observed that higher energy of activation is required for the photodegradation of MB without catalyst whereas a relatively lower energy of activation is needed in presence of SrTiO₃ and Rh doped SrTiO₃ samples. This ascertains that the catalyst alters the path of the reaction by lowering the activation energy. 1.0 Rh sample exhibited the lowest activation energy as compared to other samples. The endothermic and non-spontaneous nature of the reaction was revealed by the positive enthalpy and free energy change.

CHAPTER 3

SOLVOTHERMAL SYNTHESIS OF VANADIUM-DOPED STRONTIUM TITANATE FOR PHOTOCATALYTIC APPLICATION

Chapter 3 presents and discusses the synthesis and photocatalytic activity of V-doped SrTiO₃ by a solvothermal approach.

3.1 INTRODUCTION

Vanadium (V) doped in SrTiO₃ has been successfully studied for photocatalytic water splitting application but has been hardly reported for photocatalytic degradation of organic dyes (Modak and Ghosh 2018, Hoang et al. 2019). Vanadium is a transition element that has variable oxidation states. If introduced with an aliovalent charge (say V³⁺ or V⁵⁺) from that of the atom which it is substituting (say Ti⁴⁺) then defect states will be introduced due to the formation of oxygen vacancies which will act as recombination centers. Hence, there is a need to develop a synthetic route such that the dopant atom will be isovalent with that of the host atom which it is substituting. Herein, V-doped SrTiO₃ was synthesized by a one-pot facile solvothermal approach by avoiding high-temperature calcination. The photocatalytic activity of the pure and doped samples was evaluated by taking MB dye under visible light.

3.2 EXPERIMENTAL SECTION

3.2.1 Synthesis

All the chemicals were purchased from Sigma-Aldrich and were used as received. Titanium(IV) isopropoxide (1.47 mL) was dissolved in 10 mL of 2-propanol. To this, a calculated amount of vanadyl acetylacetonate was added and stirred for one hour to ensure complete dissolution. An appropriate amount of strontium nitrate and 10 mL of 2 M KOH were added. The resultant mixture was sealed in an autoclave and kept in a hot air oven maintained at 200 °C for 4 hours. The as-obtained precipitates were washed thoroughly with acetic acid and water. The washed products were dried in an oven at 70 °C for 8 hours. The products obtained by using 0.5, 1.0, 1.5, and 2.0 mol % of the V precursor were labeled as 0.5 V, 1.0 V, 1.5 V, and 2.0 V respectively. The details of characterization tools employed and the procedure for the determination of photocatalytic activity are discussed in the previous chapter.

3.3 RESULTS AND DISCUSSION

3.3.1 XRD Analysis

The obtained XRD patterns of SrTiO_3 and V-doped SrTiO_3 can be well-matched with the standard perovskite phase of SrTiO_3 indexed in JCPDS card number 01-089-4934 (Figure 3.1). Successful incorporation of V in SrTiO_3 is revealed by the absence of impurity peaks in the XRD patterns of V-doped samples. The shift in the 2θ values after V doping is negligible due to the similar radius of V^{4+} and Ti^{4+} ions. If V is doped in the Sr site, then an appreciable shift would have been observed as Sr^{2+} ions are larger compared to V^{4+} ions.

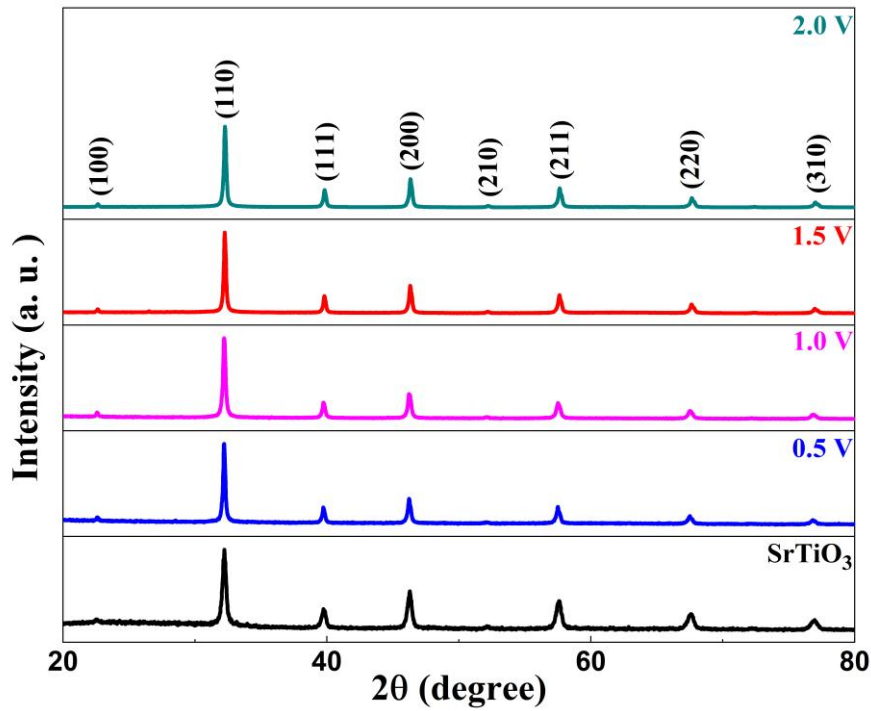


Figure 3.1 XRD patterns as a function of doping concentrations of V.

3.3.2 TEM and EDS Analysis

The TEM image of SrTiO₃ indicated irregular slightly elongated particles and that of the 1.0 V sample indicated well-formed nanocubes (Figure 3.2 a and Figure 3.2 b). The EDS analysis indicated the presence of Sr, Ti, O, and V as elements (Figure 3.2 c). HRTEM analysis indicated uniform lattice fringes of about 2.78 Å which could be indexed to the (110) plane of SrTiO₃ (Figure 3.2 d).

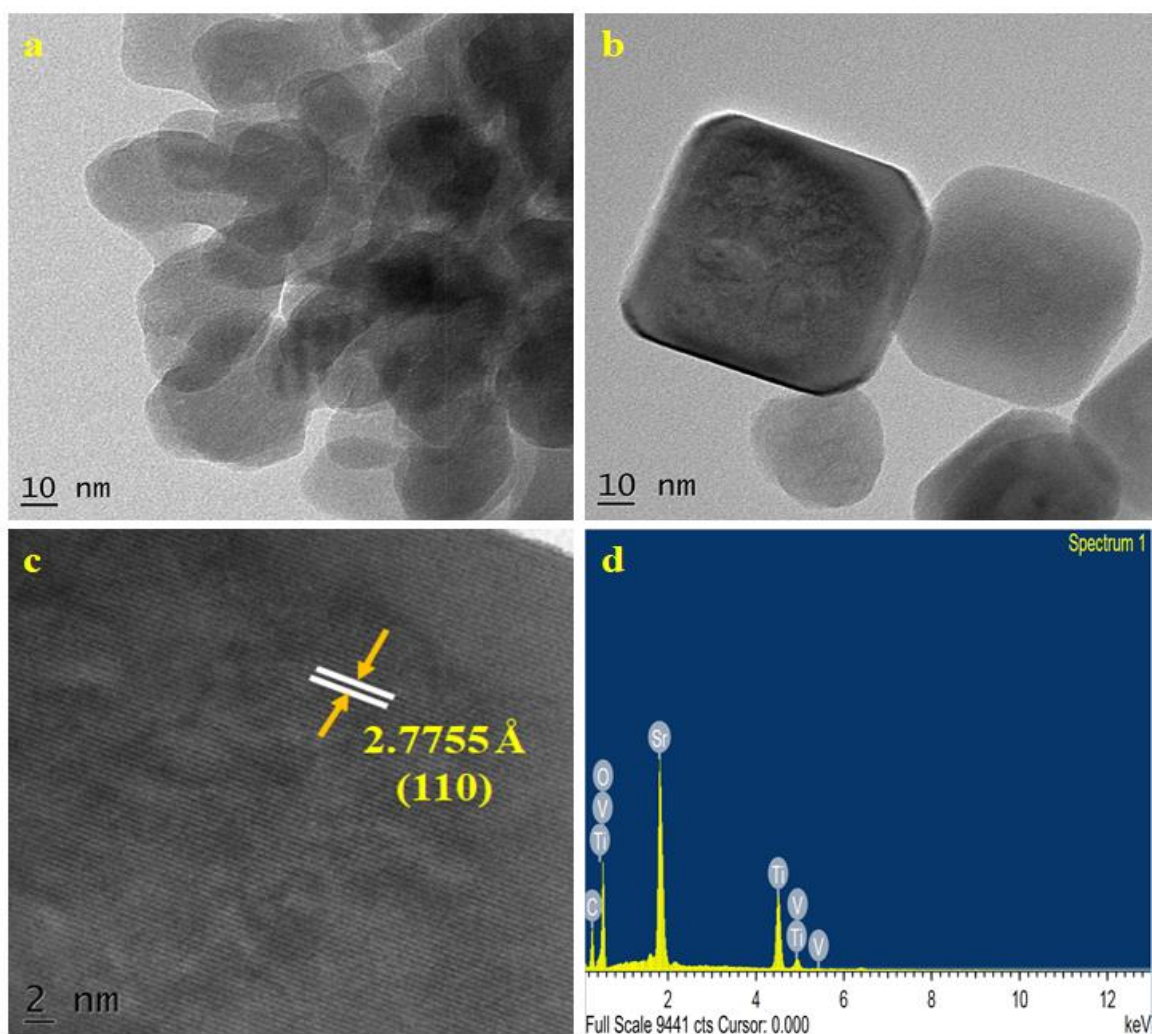


Figure 3.2 (a) TEM image of SrTiO₃, (b) TEM image of 1.0 V, (c) HRTEM image of 1.0 V and (d) EDS spectrum of 1.0 V.

3.3.3 BET Surface Area Analysis

The BET surface area of the SrTiO₃ and 1.0 V were determined with the help of nitrogen adsorption-desorption isotherms. The nitrogen adsorption-desorption isotherms exhibited a type IV pattern with the hysteresis loops mimicking type H3 (in the P/P₀ range of 0.4-1.0), indicating there may have been the development of minute pores (Figure 3.3) (Sethi et al. 2020). The higher BET surface area of the 1.0 V (36.3 m²/g) in comparison to SrTiO₃ (26.45 m²/g), facilitated the efficient adsorption and degradation of the pollutants by increasing the surface area and active site for catalysis, respectively. The pore size distribution of the 1.0 V sample was determined by BJH analysis. A broad pore size distribution can be seen in the inset of Figure 3.3, which further indicates the presence of mesopores as well as macropores. The pore volume of 1.0 V was found to be 0.1381 cm³/g which is almost three times that of SrTiO₃ (0.040 cm³/g), promoting effective transport of reactants and products during the photocatalytic reaction.

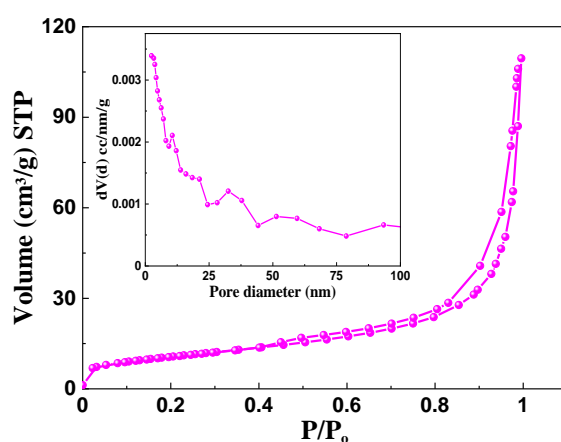


Figure 3.3 Nitrogen adsorption-desorption isotherm and BJH pore size distribution (inset) of 1.0 V.

3.3.4 XPS Analysis

XPS analysis indicated the presence of Sr, Ti, O, and V elements in the survey spectrum of the 1.0 V sample (Figure 3.4). The peaks at binding energies 132.74 eV and 134.4 eV correspond to Sr 3d_{5/2} and Sr 3d_{3/2} states, respectively (Figure 3.5 a) (Wu et al. 2017). The peaks at binding energies 457.9 eV and 463.67 eV could be attributed to Ti 2p_{3/2} and Ti 2p_{1/2} states respectively indicating the oxidation state of Ti

as +4 (Figure 3.5 b) (Wu et al. 2017). The binding energies at 529.7 eV and 531.3 eV could be allotted to lattice oxygen (O_L) and the surface hydroxyl groups (O_{OH}), respectively (Figure 3.5 c). The peaks at binding energies 515.2 eV and 523.2 eV could be ascribed to V $2p_{3/2}$ and V $2p_{1/2}$ states respectively implying the oxidation state of V as +4 (Figure 3.5 d) (Macías et al. 2019). Since, V atoms were successfully doped into the Ti sites of $SrTiO_3$ in the V^{4+} oxidation state, thus avoiding the formation of oxygen vacancies that otherwise would have been created to maintain the charge neutrality. The doping site of V in $SrTiO_3$ can also be determined experimentally using the XPS technique. Here it can be noted that the peak positions of Sr 3d increase by 0.34 eV as compared to pure $SrTiO_3$ whereas Ti 2p increase by 0.68 eV (Figure 3.6). This strongly suggests that the incorporated vanadium has more effect on the Ti sites than the Sr sites, which can be considered as another evidence for Ti site doping besides XRD analysis.

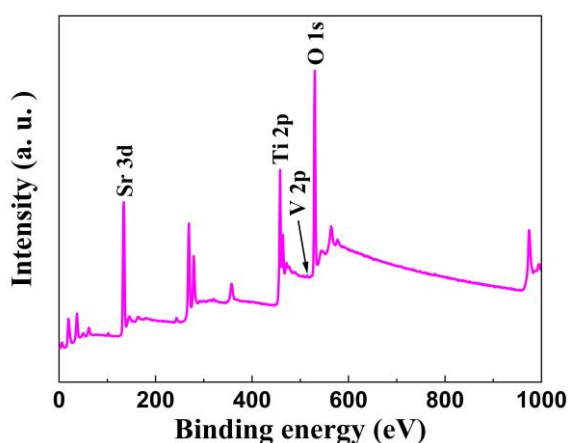


Figure 3.4 XPS survey spectrum of 1.0 V sample.

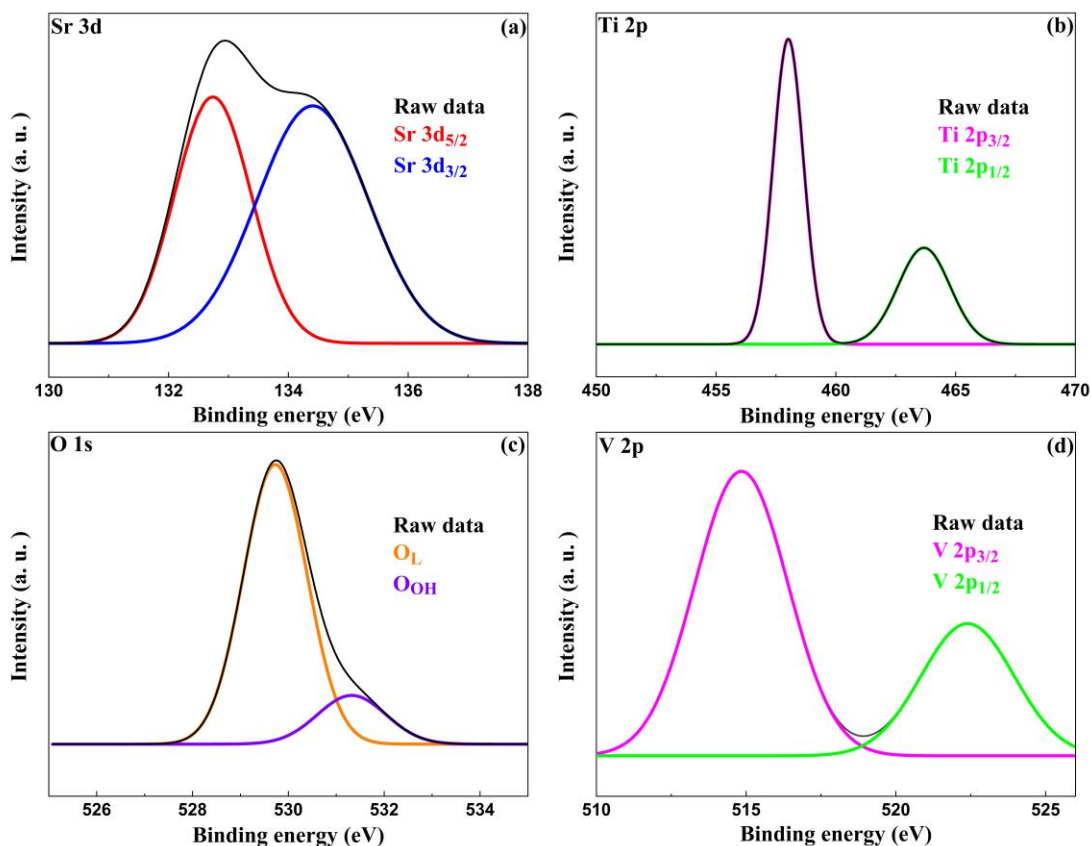


Figure 3.5 High-resolution XPS spectra (a) Sr 3d, (b) Ti 2p, (c) O 1s and (d) V 2p of 1.0 V.

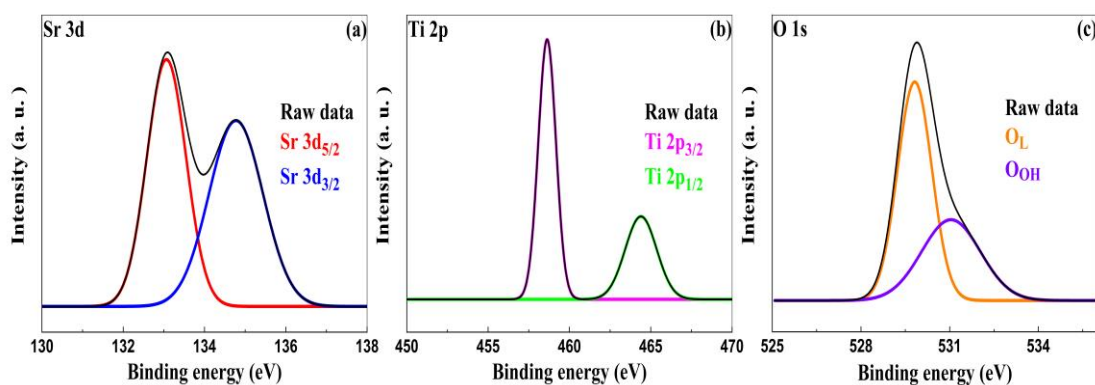


Figure 3.6 High-resolution XPS spectra (a) Sr 3d, (b) Ti 2p and (c) O 1s of pure SrTiO₃.

3.3.5 Optical Absorbance Analysis

The DR spectra showed a redshift in the absorption edge of V-doped SrTiO₃ in comparison to pristine SrTiO₃ (Figure 3.7 a). This is attributed to the dopant level

introduced by V. The absorption data was derived using the Kubelka-Munk equation 3.1 (Bhat and Shenoy 2019).

$$A/S = (1-R)^2/2R \quad (3.1)$$

where, R is the reflectance, A and S are the absorption and scattering coefficients. The band gap was determined by A/S versus energy plot (Figure 3.7 b). The band gaps of SrTiO₃, 0.5 V, 1.0 V, 1.5 V and 2.0 V were found to be 3.17 eV, 2.66 eV, 2.51 eV, 2.27 eV and 2.14 eV, respectively.

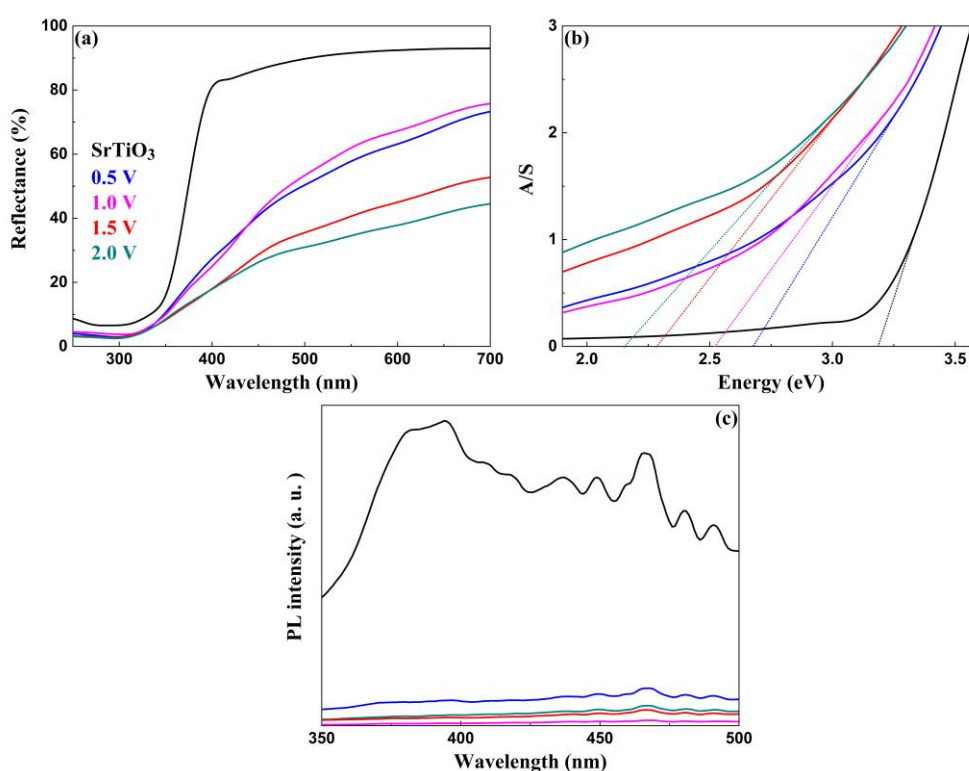


Figure 3.7 (a) UV-visible DR spectra, (b) electronic absorption spectra and (c) PL spectra of SrTiO₃ and V-doped SrTiO₃ samples.

The PL intensity of V-doped SrTiO₃ is found to be extremely low in comparison to pristine SrTiO₃ indicating that V-doped in 4+ oxidation state reduces the formation of the recombination centers and hence increases the charge carrier lifetime (Figure 3.7 c). 1.0 V shows the least PL intensity leading to the highest photocatalytic activity in the degradation of MB as explained in the subsequent section. Aliovalent doping leads to the introduction of oxygen vacancies to balance

the charge. Since this synthetic technique introduces V in an isovalent state as confirmed by XPS, the formation of oxygen vacancies is reduced thus reducing the chances of photo-generated electron-hole recombination.

3.3.6 Photocatalytic Activity

The photocatalytic efficiency of the synthesized materials was evaluated for the decomposition of MB dye solution under visible light (Figure 3.8 a). We observe that the photocatalytic activity of V-doped SrTiO₃ samples is higher than the pristine SrTiO₃. This is attributed to the decrease in the band gap of the material with an increase in the dopant concentration. Substitution of V in Ti site introduces continuous energy level in CB facilitating the easy migration and separation of photogenerated charge carriers. In addition to it, the 1.0 V sample shows a higher surface area facilitating higher adsorption of MB dye leading to subsequent degradation of adsorbed molecules.

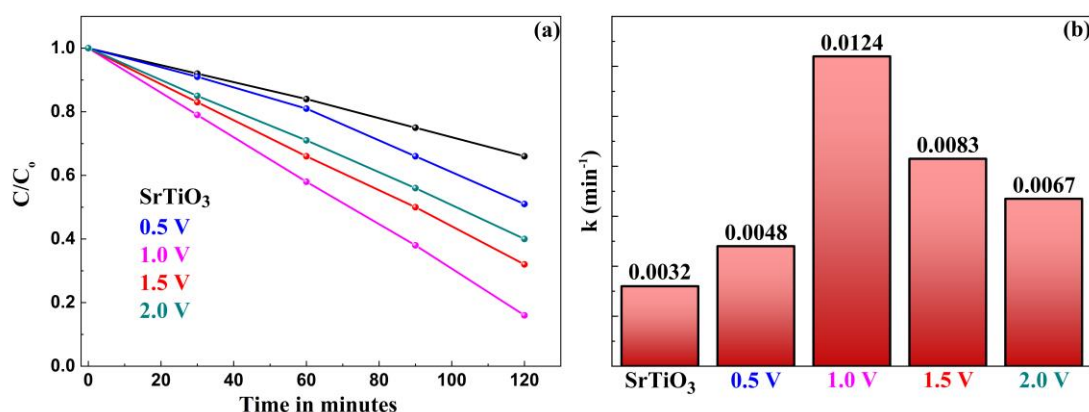


Figure 3.8 (a) Photocatalytic degradation curves and (b) rate constants for the photocatalytic degradation of MB by SrTiO₃ and doped samples.

The kinetics of the photocatalytic degradation of MB by SrTiO₃ and V-doped SrTiO₃ is in good agreement with the pseudo-first-order rate equation given by (2.3). The rate constant of 1.0 V was found to be higher than all the other samples indicating the high efficiency of the sample (Figure 3.8 b). The high stability of 1.0 V is further confirmed from the cyclic stability test indicating the photo corrosion resistance of the material (Figure 3.9).

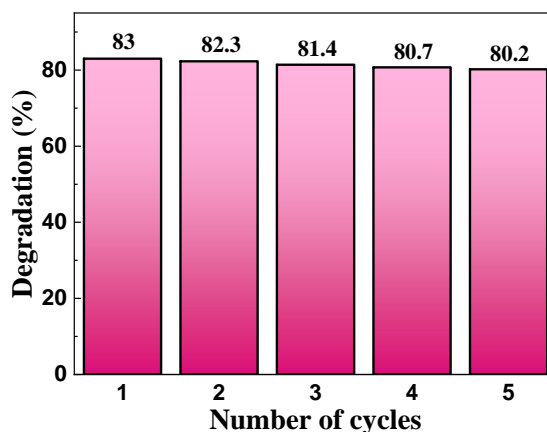


Figure 3.9 Cyclic stability of the synthesized 1.0 V.

From Figure 3.10, it can be seen that superoxide radical anions are not the major active species as the corresponding scavenger benzoquinone did not deteriorate the photocatalytic activity much. Whereas the addition of potassium iodide (hole scavenger) and isopropyl alcohol (OH^\cdot scavenger) reduced the photocatalytic activity significantly. As a result, holes followed by hydroxyl radicals are considered to be the active species for the effectual degradation of dye.

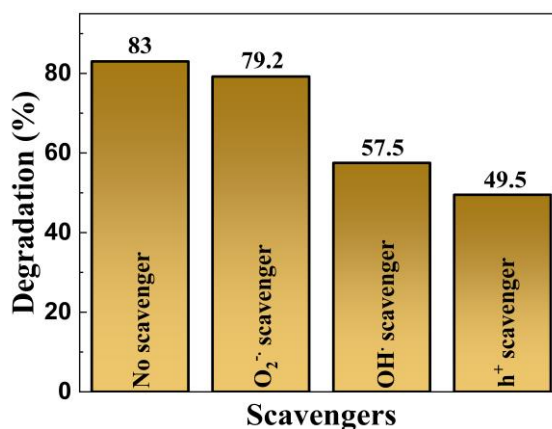


Figure 3.10 Effect of radical and hole scavengers on the photocatalytic degradation of MB by 1.0 V.

The mechanism of degradation is follows: When V-doped SrTiO_3 is irradiated with an energy equal to or greater than its band gap, electrons from the VB get excited to the CB leaving the corresponding number of holes in VB. These electrons in CB react with oxygen to produce superoxide radicals ($\text{O}_2^{\cdot-}$) and the holes in VB either directly react with MB or surface adsorbed water to produce hydroxyl radicals (OH^\cdot).

The formed radicals are said to be active species for the effectual degradation of MB to CO₂ and water (Figure 3.11).

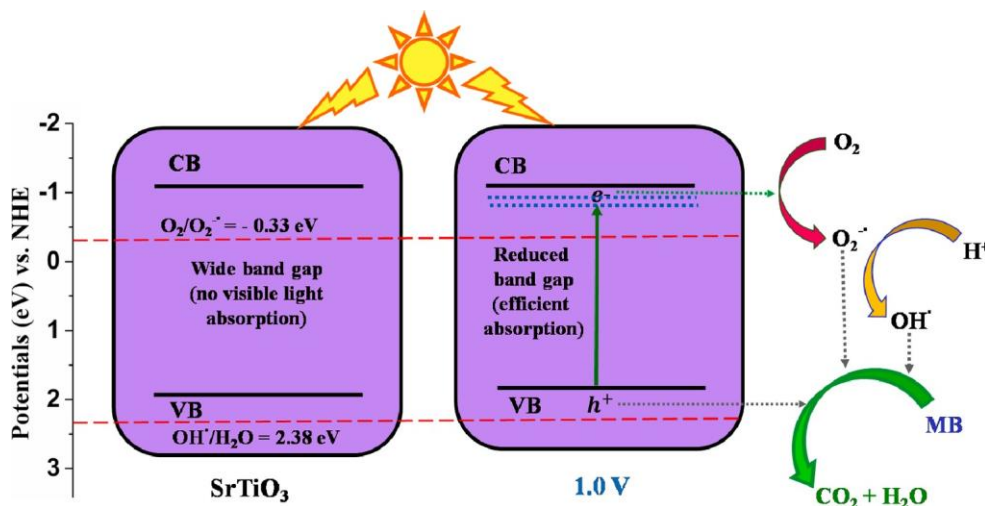


Figure 3.11 The photocatalytic mechanism for the degradation of MB by V-doped SrTiO₃ under visible light irradiation.

The thermodynamic parameters such as activation energy (E_a), the free energy of activation (ΔG^\ddagger), enthalpy of activation (ΔH^\ddagger), and entropy of activation (ΔS^\ddagger) were computed as described in Chapter 2.

Table 3.1 Thermodynamic parameters of SrTiO₃ and V doped SrTiO₃ samples.

Sample	E_a (kJ/mol)	ΔH^\ddagger (kJ/mol)	ΔS^\ddagger (kJ/mol)	ΔG^\ddagger (kJ/mol)
SrTiO ₃	14.3	11.8	-0.25	87.8
0.5 V	13.3	10.8	-0.25	86.8
1.0 V	10.9	8.4	-0.25	84.4
1.5 V	11.9	9.4	-0.25	85.4
2.0 V	12.4	9.9	-0.25	85.9
Without catalyst	17.7	15.2	-0.25	91.2

From the values tabulated (Table 3.1), it can be observed that higher energy of activation is required for the photodegradation of MB without catalyst whereas a

relatively lower energy of activation is needed in presence of SrTiO₃ and V-doped SrTiO₃. This ascertains that the catalyst alters the path of the reaction by lowering the activation energy. 1.0 V sample exhibited the lowest activation energy as compared to other samples. The endothermic and non-spontaneous nature of the reaction was revealed by the positive enthalpy and free energy change.

CHAPTER 4

SOLVOTHERMAL SYNTHESIS OF POROUS GRAPHENE-STRONTIUM TITANATE NANOCOMPOSITE FOR PHOTOCATALYTIC APPLICATION

Chapter 4 presents and discusses the synthesis and photocatalytic activity of porous graphene-SrTiO₃ nanocomposite by a solvothermal approach.

4.1 INTRODUCTION

Although doping has been implemented to tune the electronic structure and reduce the band gap this leads to the surfacing of another drawback viz. the high rate of recombination due to the introduction of defect states of the dopant atom (Kawasaki et al. 2012, Kawasaki et al. 2014). Also, poor transport of carriers leads to inefficient charge separation and hence reduced lifetime of photogenerated electron-hole pairs. Therefore, to facilitate the rapid transport of charge carriers to the reaction site blending SrTiO₃ with an efficient conducting material is essential.

Graphene, a 2D layer of sp² hybridized carbon atoms with a hexagonal motif is known to possess favorable properties. Porous graphene (PG) on the other hand which is formed by the removal of one sp² hybrid carbon atom is known to possess outstanding properties (Sethi et al. 2019). Hence, SrTiO₃-PG composite is expected to exhibit high conductivity, adsorptivity, and enhanced photocatalytic activity. Although the synthesis of SrTiO₃/graphene composites for photocatalytic applications has been previously reported, the synthesis of porous graphene-SrTiO₃ (PGST) composite has not been reported (He et al. 2018, Ahmadi et al. 2019, Govindasamy et al. 2019). Hence, the development of a facile synthetic technique for producing highly efficient PGST composite for photocatalytic applications is highly anticipated. The goal is to design the synthesis such that the composite possesses high surface area, has an appropriate band gap for visible light absorption and the surface interaction between SrTiO₃ and PG is high to facilitate easy charge carrier transfer along with the reduced tendency for recombination of photogenerated electron-hole pair.

Herein, the PGST composite was prepared by a facile and reproducible one-step solvothermal approach. The synthesized materials were thoroughly characterized by XRD, Raman spectroscopy, XPS, FESEM, TEM, BET analysis, DR spectroscopy, and PL spectroscopic techniques. The photocatalytic efficiency of PGST was assessed by analyzing the degradation of MB dye solution.

4.2 EXPERIMENTAL SECTION

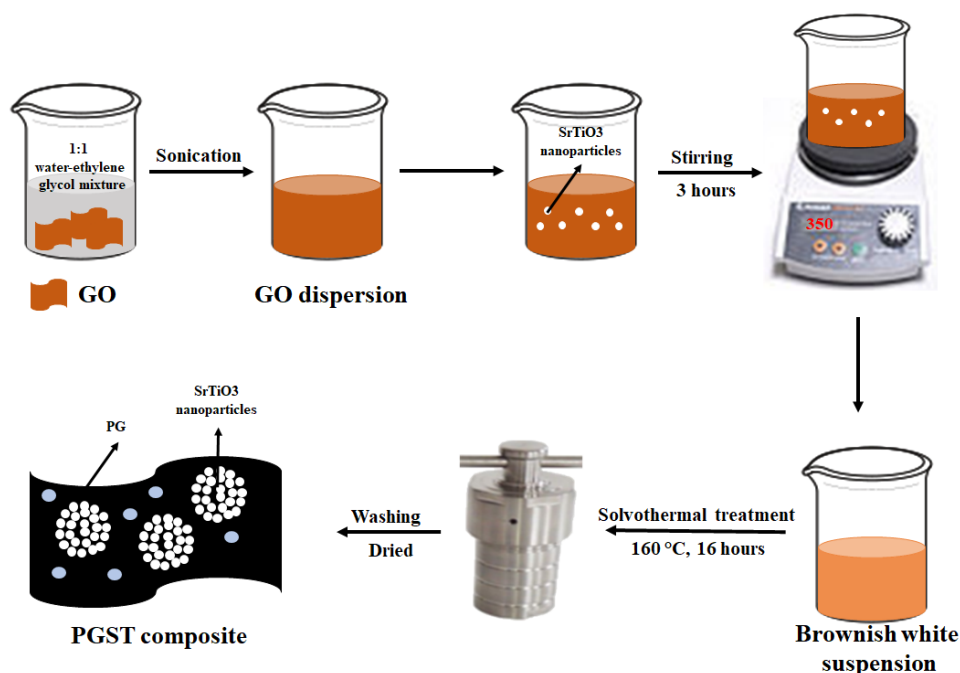


Figure 4.1 Schematic illustration of the synthesis of PGST composite.

4.2.1 Synthesis of PGST Composite

All chemicals were procured from Sigma Aldrich and were used without further purification. GO, PG and SrTiO₃ were synthesized according to the previously reported procedure (Sethi et al. 2019, Shenoy et al. 2018). ‘x PGST’ ($x = 2.5, 5.0, 7.5,$ and 10.0 wt % GO) was synthesized by a simple solvothermal approach (Figure 4.1). A calculated amount of SrTiO₃ powder was added to the solution of GO dispersed in a 1:1 water-ethylene glycol mixture and stirred for 3 hours to obtain a homogeneous solution. The resultant mixture was sealed in an autoclave and then heated to 160 °C for 16 hours. The obtained black precipitates were thoroughly washed with distilled water and dried in an oven at 70 °C for 8 hours. The composite obtained by taking 2.5, 5.0, 7.5, and 10.0 wt % GO was labeled as 2.5 PGST, 5.0 PGST, 7.5 PGST, and 10 PGST, respectively.

4.2.2 Characterization

Raman spectra were recorded with the help of a He–Ne source operating at 532 nm (Renishaw Invia). The details of other characterization tools employed and

the procedure for the determination of photocatalytic activity are discussed in the previous chapters.

4.3 RESULTS AND DISCUSSION

4.3.1 XRD Analysis

XRD technique was used for the crystallographic study of the as-synthesized catalysts. The peak indexed XRD plot (Figure 4.2) of PGST samples matched well with the cubic phase of SrTiO_3 (JCPDS card No. 01-089-4934). A small shift in the 2θ value of (110) peak from 32.21° (SrTiO_3) to 32.17° (7.5 PGST) indicates the possible interaction between the components of the composite formed. Scherrer equation was used to calculate the average crystal sizes using (110) peak. The calculated values turned out to be 34.7 nm, 32.8 nm, 30.0 nm, 28.8 nm, and 26.1 nm for SrTiO_3 , 2.5 PGST, 5.0 PGST, 7.5 PGST, and 10 PGST, respectively. Due to the lower quantity of PG in the composite, peaks corresponding to it are absent. However, its presence is confirmed from Raman spectra. Among the different composite samples, 7.5 PGST showed the highest photocatalytic activity. Hence, for detailed analysis, only a 7.5 PGST sample was considered.

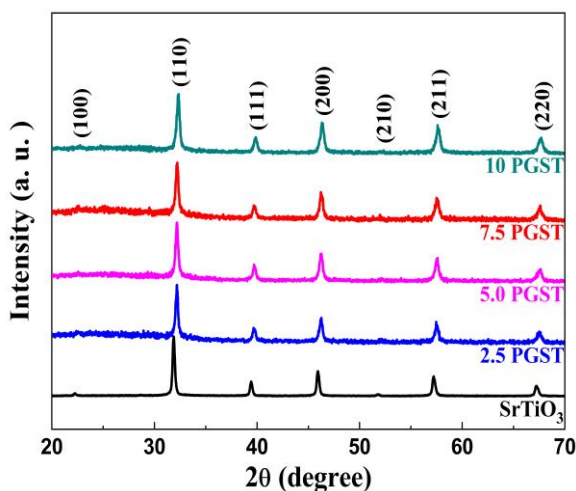


Figure 4.2 XRD patterns of SrTiO_3 and PGST samples.

4.3.2 Raman Analysis

The Raman spectra of PG reveal a peak at 1347.5 cm^{-1} (D band), which can be assigned to the presence of sp^3 defects, and another peak at 1590.7 cm^{-1} (G band), which can be attributed to the in-plane vibration of sp^2 bonded carbon atoms (Figure 4.3) (Sethi et al. 2019). These peaks shift to 1348.8 cm^{-1} and 1588.5 cm^{-1} , respectively in 7.5 PGST. It is seen that the intensity ratio of the D band to the G band (I_D/I_G) in the case of 7.5 PGST (0.94) is lower than that of PG (1.05). This is attributed to the interaction of PG with SrTiO_3 moiety which neutralizes the free defects present in the PG (Sadiq et al. 2016).

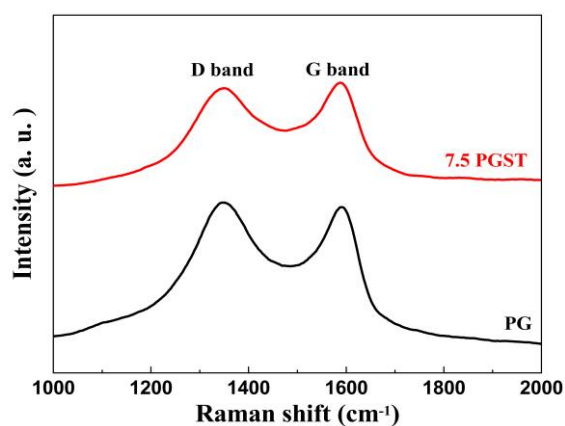


Figure 4.3 Raman spectra of PG and 7.5 PGST.

4.3.3 FESEM and TEM analysis

The morphological study of 7.5 PGST was carried out using FESEM and TEM. Figure 4.4 a reveals SrTiO_3 nanoparticles as spherical agglomerates while Figure 4.4 b shows PG in the form of wrinkled sheets with porous nature. The TEM image of 7.5 PGST shows SrTiO_3 nanoparticles being wrapped in PG sheets and the entire composite having a loofah-like structure (Figure 4.4 c). The wrapping of nanoparticles by PG increases the area of contact between the two components facilitating better interaction for charge transfer in comparison to SrTiO_3 particles being just distributed on the planar PG sheets (He et al. 2018). HRTEM analysis indicated lattice fringes of about 2.78 \AA which could be attributed to the (110) plane of SrTiO_3 (Figure 4.4 d).

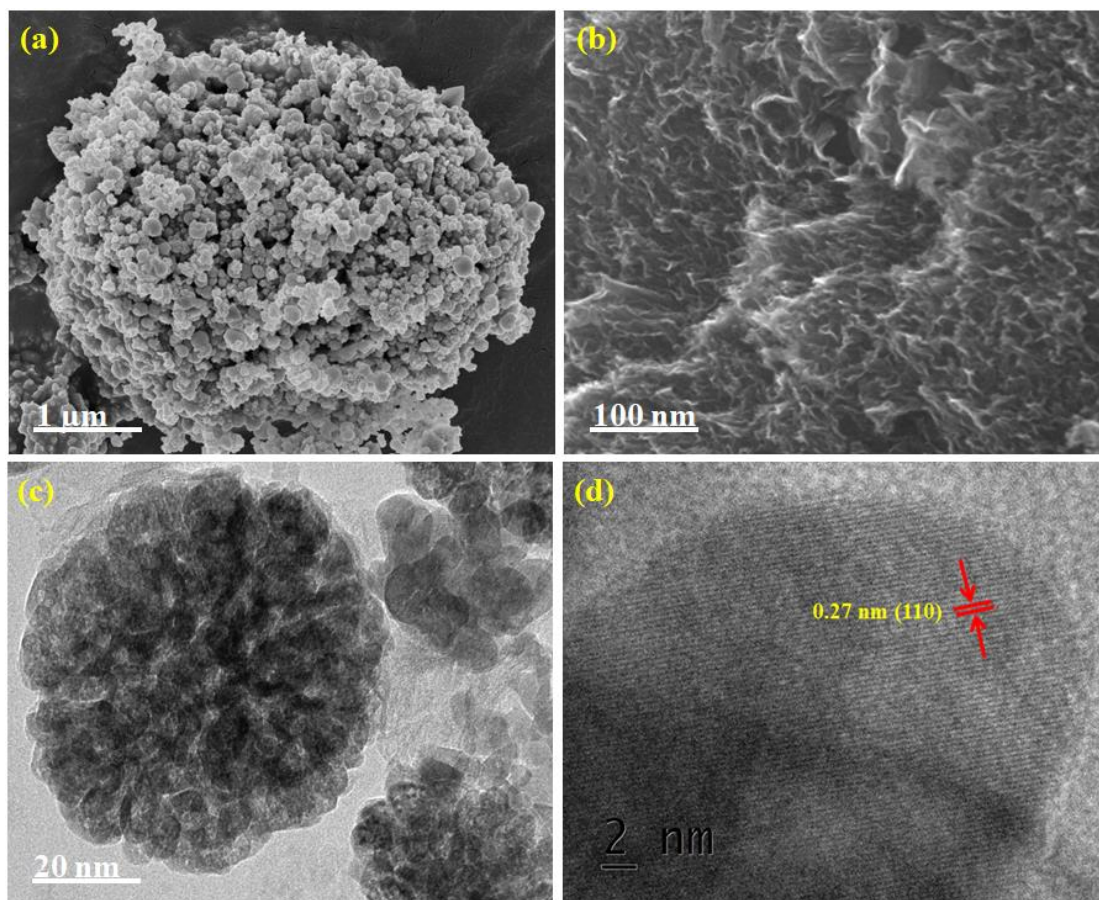


Figure 4.4 FESEM image of (a) SrTiO₃ nanoparticles, (b) PG, (c) TEM image of 7.5 PGST and (d) HRTEM image of 7.5 PGST.

4.3.4 BET Surface Area Analysis

The nitrogen adsorption analysis was carried out to obtain information on the specific surface area and porosity of PGST. The isotherm for 7.5 PGST was type IV with hysteresis loops of type H3, indicating the presence of slit-like pores (Figure 4.5) (Sadiq et al. 2017). The BET-specific surface area of 7.5 PGST was found to be 65.35 m²g⁻¹, which is much greater than SrTiO₃ (26.45 m²g⁻¹). The large surface area of the composite is due to the formation of contusions in the loofah-like structure. This in turn allows more MB dye molecules to get adsorbed onto the surface of the catalyst due to the π - π interaction between the PG and MB dye molecule. The photogenerated carrier migrates to the surface of the material to react with oxygen or water to form active species. Adsorption of MB dye on the surface of the catalyst decreases the path length to be traveled by the active species for the effective reaction and hence

increases the photocatalytic activity. The BJH method was utilized to analyze the pore size distribution of 7.5 PGST indicating the presence of mesopores with a pore volume of $0.151 \text{ cm}^3\text{g}^{-1}$ (Figure 4.5 inset) while that of SrTiO_3 was $0.040 \text{ cm}^3\text{g}^{-1}$.

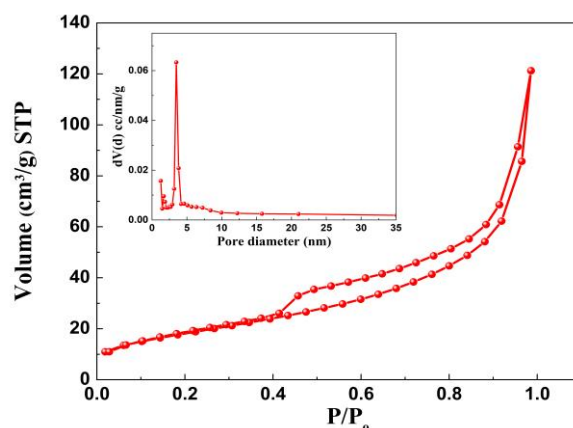


Figure 4.5 Nitrogen adsorption-desorption isotherm and BJH pore size distribution (inset) of 7.5 PGST.

4.3.5 XPS Analysis

XPS survey spectrum of 7.5 PGST reveals the presence of Sr, Ti, O, and C (Figure 4.6). The peaks at binding energies 132.5 eV and 134.3 eV are attributed to Sr $3d_{5/2}$ and Sr $3d_{3/2}$ states, respectively (Figure 4.7 a) (Shenoy et al. 2018). While the peak at 132.96 corresponds to Sr bonded to C. This suggests the chemical interaction of SrTiO_3 with the PG in the composite which is favorable for the transport of photogenerated electrons. One of the main reasons for the low efficiency of a photocatalyst despite having a favorable band gap is the recombination of charge carriers. The formation of Sr-C bonds facilitates the transfer of electrons generated in SrTiO_3 to electron-accepting PG, thereby separating the electrons and holes and reducing the recombination of the charges. Ti $2p_{3/2}$ and Ti $2p_{1/2}$ states appear as peaks in Figure 4.7 b at binding energies of 458.13 eV and 463.93 eV, respectively (Shenoy et al. 2018). The peak at 529.3 eV in Figure 4.7 c is due to the lattice oxygen (O_L) and at 531.2 eV is due to the surface hydroxyl groups (O_{OH}) (Shenoy et al. 2018). Figure 4.7 d shows the high-resolution C 1s spectrum which is deconvoluted into two peaks of binding energies 284.7 eV and 285.7 eV and is attributed to sp^2 carbon of PG and C-H bond of sp^3 carbon atom at the edge of PG, respectively (Sethi et al. 2019).

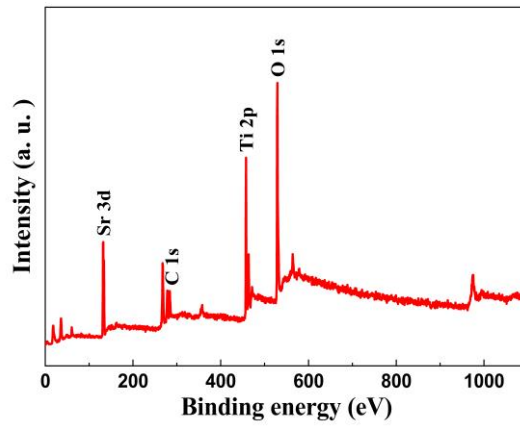


Figure 4.6 XPS survey spectrum of 7.5 PGST sample.

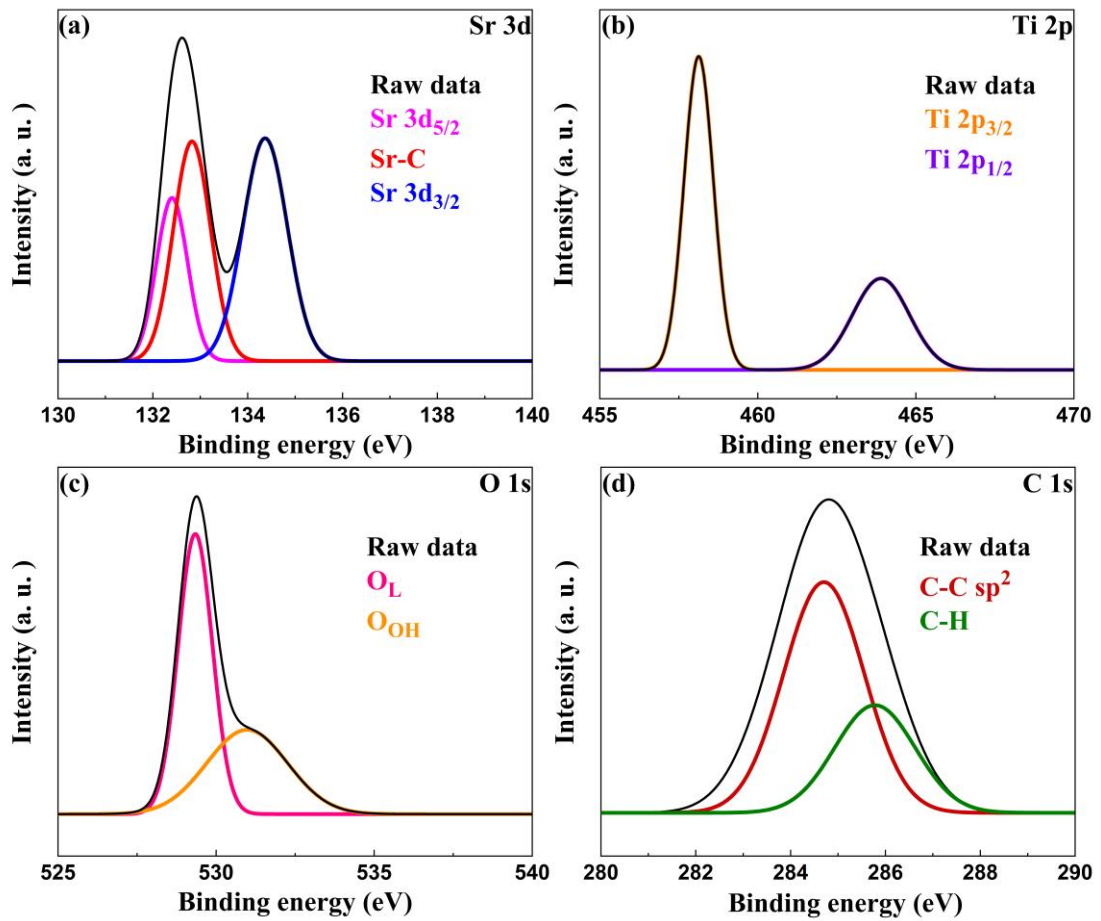


Figure 4.7 High-resolution XPS spectra (a) Sr 3d, (b) Ti 2p, (c) O 1s and (d) C 1s of 7.5 PGST.

4.3.6 Optical Absorbance Analysis

The UV-visible absorbance plot of SrTiO₃ exhibited an absorption edge at 387 nm, due to the electronic transition from the O 'p' to the Ti 'd' states. The absorption band edges of PGST exhibited a redshift from 405 nm to 431 nm (Figure 4.8 a). SrTiO₃ exhibited a band gap of 3.21 eV while the band gap of the PGST samples decreased gradually from 3.06 eV (405 nm), 3.03 eV (409 nm), 2.93 eV (424 nm) to 2.87 eV (431 nm) for 2.5 PGST, 5.0 PGST, 7.5 PGST, and 10 PGST, respectively. This decrease in the band gap of PGST is attributed to the formation of C 'p' states above the VB and Sr 's' states below the CB.

The PL spectra of the as-synthesized SrTiO₃ and PGST were examined to get more information on the recombination behavior of photoinduced charges (Figure 4.8 b). Compared with SrTiO₃, a severe decrease in the fluorescence intensity of PGST samples can be observed. This decrease in the PL intensity of the PGST samples is because of the lower recombination rate of photoinduced holes and electrons due to efficient electron transfer from SrTiO₃ by the PG through the Sr-C bond. Further increasing the PG content above its optimal value resulted in the enhancement of fluorescence intensity due to agglomeration of PG which again introduces recombination centers.

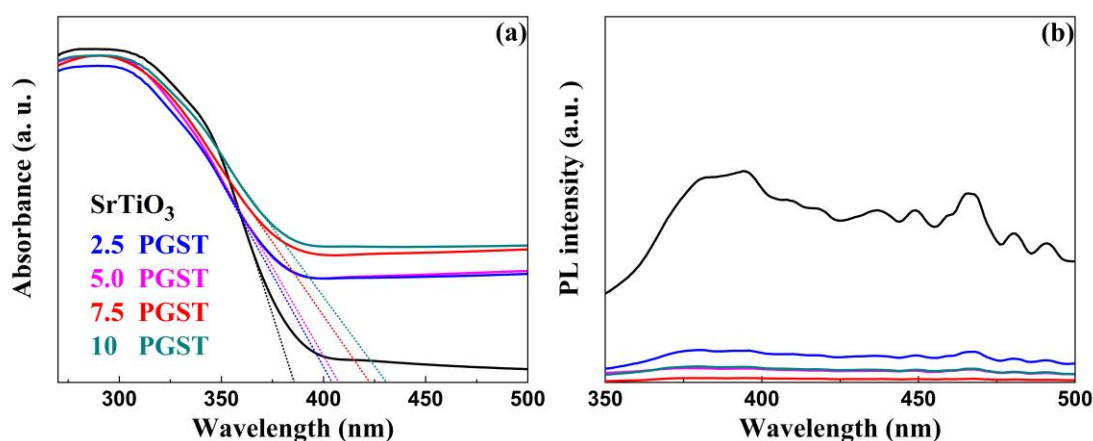


Figure 4.8 (a) UV-visible DR spectra and (b) PL spectra of SrTiO₃ and PGST.

4.3.7 Photocatalytic Activity

The percentage degradation of MB by SrTiO₃, 2.5 PGST, 5.0 PGST, 7.5 PGST, and 10 PGST was found to be 45.7, 70.4, 80.8, 91.9, and 79.5, respectively (Figure 4.9 a). The enhanced photocatalytic activity of 7.5 PGST can be attributed to

the enhanced light absorption in the visible region, high surface area, high pore volume, and low recombination rate of photoinduced charges. The large surface area of the 7.5 PGST composite allows more MB dye molecules to get adsorbed onto the surface of the catalyst and the higher pore volume leads to the rapid diffusion of various inorganic products formed during the photocatalytic reaction (Kampouri et al. 2019). On the other hand, in the case of 10 PGST, the higher amount of PG content hinders the absorption of light by SrTiO₃ nanoparticles which can cause decreased generation of electron-hole pairs (Sadiq et al. 2016). The presence of excess PG can also act as a recombination center for photoinduced electron-hole pairs as revealed by PL results. Due to these reasons, the photocatalytic activity of 10 PGST was found to be lower.

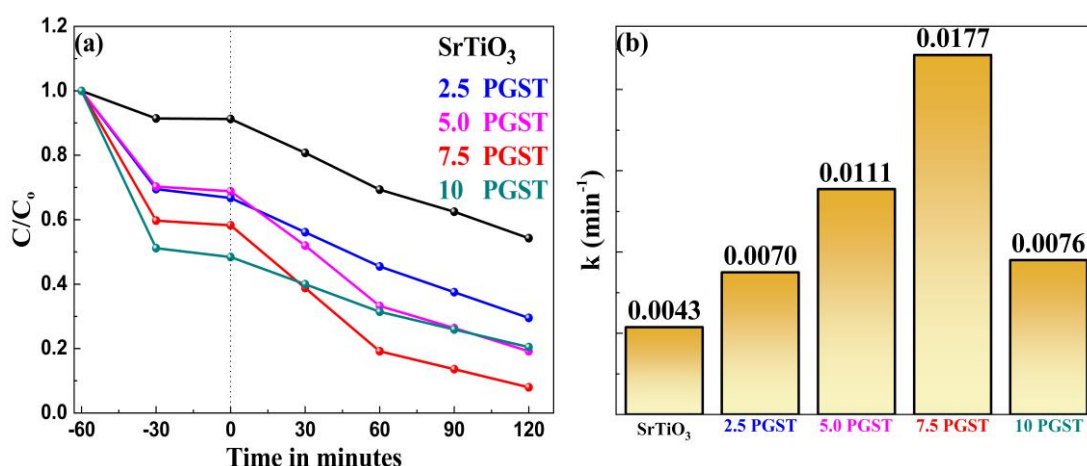


Figure 4.9 (a) Photocatalytic degradation curves and (b) rate constants for the photocatalytic degradation of MB by SrTiO₃ and PGST.

The above photocatalytic reaction follows the pseudo-first-order rate equation 2.3. It is found that the rate constant increases with an increase in PG content (Figure 4.9 b). 7.5 PGST exhibited a value of 0.0177 min⁻¹, which is higher than the SrTiO₃ (0.0043 min⁻¹). The drop in the photocatalytic activity of 7.5 PGST after five consecutive cycles was minimal, pointing to its high stability (Figure 4.10).

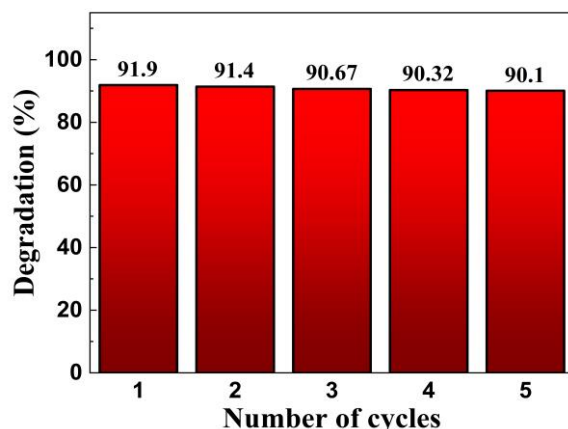


Figure 4.10 Cyclic stability of the synthesized 7.5 PGST.

Also, the addition of potassium iodide reduced the photocatalytic activity to the maximum extent followed by isopropyl alcohol indicating that holes and hydroxyl radicals are the major active species (Figure 4.11). Benzoquinone addition had the least effect indicating $O_2^{\cdot -}$ had a minor role in the degradation of MB.

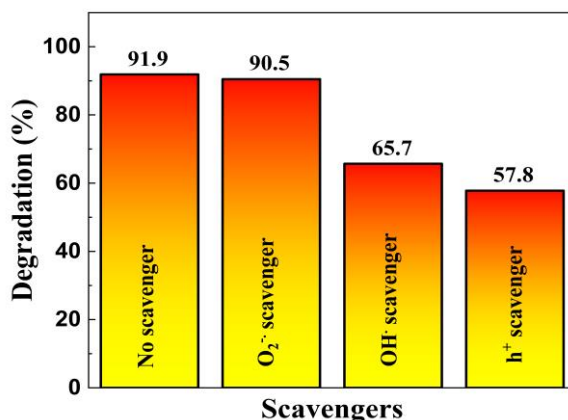


Figure 4.11 Effect of radical and hole scavengers on the photocatalytic degradation of MB by 7.5 PGST.

Taking into consideration of these results, the mechanism of photocatalytic degradation of MB by PGST can be explained as follows (Figure 4.12). When a photon of suitable energy is irradiated on PGST, electron-hole pairs are generated in $SrTiO_3$. As PG is an electron acceptor, the electrons from the $SrTiO_3$ transfer to it through the Sr-C bond thereby reducing the rate of recombination of photoinduced charges and boosting the photocatalytic activity. These electrons react with oxygen to produce superoxide radicals and the holes either directly oxidize MB or react with

surface adsorbed water to produce hydroxyl radicals. These generated active species act as a strong oxidizer for the effectual degradation of the MB adsorbed on the PGST to CO₂ and H₂O.

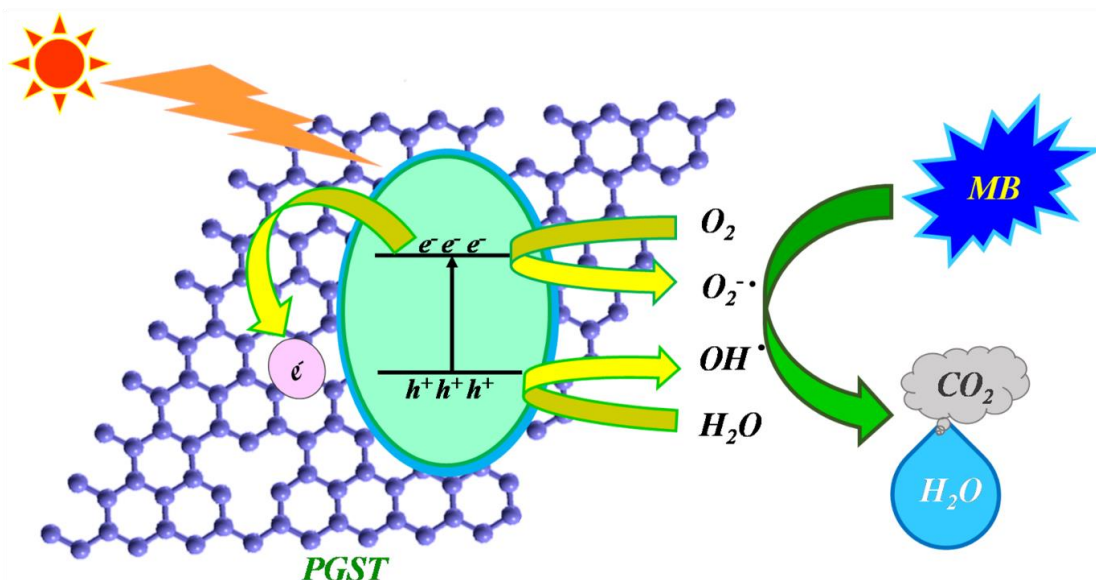


Figure 4.12 Mechanism of photocatalytic degradation of MB by PGST.

The thermodynamic parameters such as, activation energy (E_a), the free energy of activation (ΔG^\ddagger), enthalpy of activation (ΔH^\ddagger), and entropy of activation (ΔS^\ddagger) were computed as described in Chapter 2.

Table 4.1 Thermodynamic parameters of the SrTiO₃ and PGST samples

Sample	E_a (kJ/mol)	ΔH^\ddagger (kJ/mol)	ΔS^\ddagger (kJ/mol)	ΔG^\ddagger (kJ/mol)
SrTiO ₃	13.5	11.0	-0.25	87.0
2.5 PGST	12.3	9.8	-0.25	85.8
5.0 PGST	11.2	8.7	-0.25	84.7
7.5 PGST	10.0	7.5	-0.25	83.5
10 PGST	12.1	9.6	-0.25	85.6
Without catalyst	17.7	15.2	-0.25	91.2

From the values tabulated (Table 4.1), we observe that higher energy of activation is required for the photodegradation of MB without catalyst whereas relatively lower energy of activation is needed in presence of SrTiO₃ and PGST samples. This ascertains that the catalyst alters the path of the reaction by lowering the activation energy. 7.5 PGST sample exhibited the lowest activation energy as compared to other samples. The endothermic and non-spontaneous nature of the reaction was revealed by the positive enthalpy and free energy change.

CHAPTER 5

HYDROTHERMAL SYNTHESIS OF RHODIUM-DOPED BARIUM TITANATE FOR PHOTOCATALYTIC APPLICATION

Chapter 5 presents and discusses the synthesis and photocatalytic activity of Rh-doped BaTiO₃ by a solvothermal approach.

5.1 INTRODUCTION

BaTiO₃ is a versatile material with a highly tunable crystal and electronic structure with the potential of being a multifunctional material (Ali et al. 2020, Xu et al. 2019). So far, the piezoelectric effect of BaTiO₃ has been used to enhance the separation of photo-generated charge carriers while it is also combined with some other plasmonic nanomaterials of Ag or Au to further meet the challenge of absorption of the visible light radiation (Xu et al. 2019, Liu et al. 2020, Liu et al. 2020). Besides this, compositing with carbon-based materials have also been adopted to enhance the photocatalytic efficiency via promoting charge carrier separation (Mengting et al. 2019, Wang et al. 2015, Xian et al. 2015, Demircivi et al. 2020).

Various dopants such as Ce, Cr, Fe, In, Mn, Mo, Ni, N, Rh, W, and Zn have been used to reduce the band gap of BaTiO₃ and bring its absorption from UV to the visible region of the solar spectrum and thus improving its photocatalytic efficiency (Zhong et al. 2019, Zou et al. 2012, Nageri and Kumar 2018, Senthilkumar et al. 2019, Amaechi et al. 2021, Amaechi et al. 2019, Xie et al. 2019, Cao et al. 2014, Demircivi and Simsek 2019). Doped BaTiO₃ has largely been used for the photocatalytic production of hydrogen rather than the degradation of dyes (Zhong et al. 2019, Zou et al. 2012, Xie et al. 2019, Huang et al. 2019). Doping is well known to largely affect the electronic structure and hence properties associated with it depending on the site which it occupies (Shenoy and Bhat 2020, Shenoy and Bhat 2017). Therefore, in addition to being stable, nontoxic, and having an appropriate band gap, the recombination rate should be low with increase in the lifetime of charge carriers for a material to be an ideal photocatalyst (Mohamed et al. 2018).

Rh is an ideal dopant in SrTiO₃ for photocatalytic degradation of MB and found that site occupancy plays a major role in the performance of the material (Shenoy et al. 2018). Although Rh has already been doped in BaTiO₃ its efficiency as a photocatalyst is tested only for hydrogen generation (Maeda 2014, Nishioka and Maeda 2015). Herein, Rh-doped BaTiO₃ was synthesized by a simple hydrothermal technique. It should be noted here that except for this series all other series presented

in this thesis were synthesized by the solvothermal approach. Since the solvothermal approach did not yield satisfactory results under the prevailing synthetic conditions, hence hydrothermal approach was utilized. Since Rh is expensive, the final material was made considerably economic by trying to achieve higher efficiency for a low concentration as 0.5 Rh (mol%). 96 % degradation exhibited in 120 min and high cyclic stability revealed high efficiency of the material as a photocatalyst in comparison to 65.2 % exhibited by 0.5 Rh doped in SrTiO₃ (Shenoy et al. 2018).

5.2 EXPERIMENTAL SECTION

5.2.1 Synthesis

All the chemicals were purchased from Sigma-Aldrich and were used as received without further purification. 0.35 g of titanium (IV) oxide, anatase (325 Mesh Powder) was added into 30 mL of 5 M KOH solution. To this, the calculated amount of rhodium (III) chloride and barium hydroxide (octahydrate) were added and stirred for one hour. The resultant mixture was sealed in an autoclave and kept in a hot air oven maintained at 180 °C for 20 hours. The as-obtained precipitates were washed thoroughly with acetic acid and water. The washed products were dried in an oven at 70 °C for 8 hours. The products obtained by using 0.1, 0.3, 0.5, 0.7, and 0.9 mol % of the Rh precursor were labeled as 0.1 Rh, 0.3 Rh, 0.5 Rh, 0.7 Rh, and 0.9 Rh, respectively. The details of other characterization tools employed and the procedure for the determination of photocatalytic activity are discussed in the previous chapters.

5.3 RESULTS AND DISCUSSION

5.3.1 XRD Analysis

The XRD pattern of the synthesized samples matched well with the cubic phase of BaTiO₃ (JCPDS card no. 00-031-0174) indicating that both doped and undoped samples had the same crystal structure (Figure 5.1 a). Successful incorporation of Rh in BaTiO₃ is revealed by the absence of impurity peaks in the XRD patterns of Rh-doped samples. The ionic radius of Rh³⁺, Ba²⁺, and Ti⁴⁺ is 0.067 nm, 0.161 nm, and 0.061 nm, respectively which means that Rh should preferably be doped in the Ti site. Substitution in the Ti site would have caused a slight increase in the lattice parameter which was not the case here. The synthetic approach adopted here directs the Rh towards the Ba site which leads to a reduction in the lattice

parameter to 4.02 Å. This manifests as the shifting of peaks towards higher θ values in the doped samples with respect to the undoped BaTiO₃ (Figure 5.1 b).

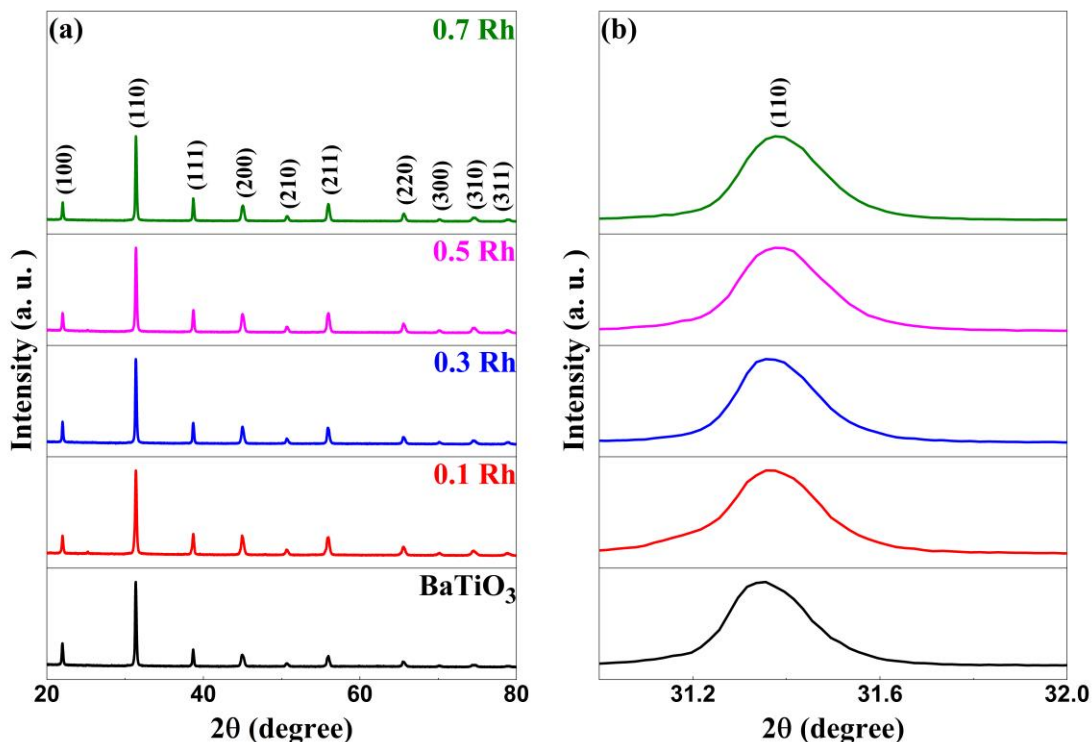


Figure 5.1 (a) XRD patterns of BaTiO₃ and Rh doped BaTiO₃ with varying concentrations of Rh and (b) diffraction peaks of (110) planes in the range of $2\theta = 31^\circ - 32^\circ$.

5.3.2 EDS and TEM Analysis

The morphology of the samples was studied using TEM. It can be seen that undoped BaTiO₃ has a cuboctahedral shape while doping it with Rh makes it cubic in structure (Figures 5.2 a and 5.2 b). The 110 planes can be clearly observed in the HRTEM image of 0.5 Rh with a spacing of 0.28 nm (Figure 5.2 c). The single crystalline nature of the synthesized 0.5 Rh indicates the success of the employed synthetic technique. The elemental composition studied using EDX reveals Ba, Ti, O, and Rh as elements present confirming the results from XPS (Figure 5.2 d).

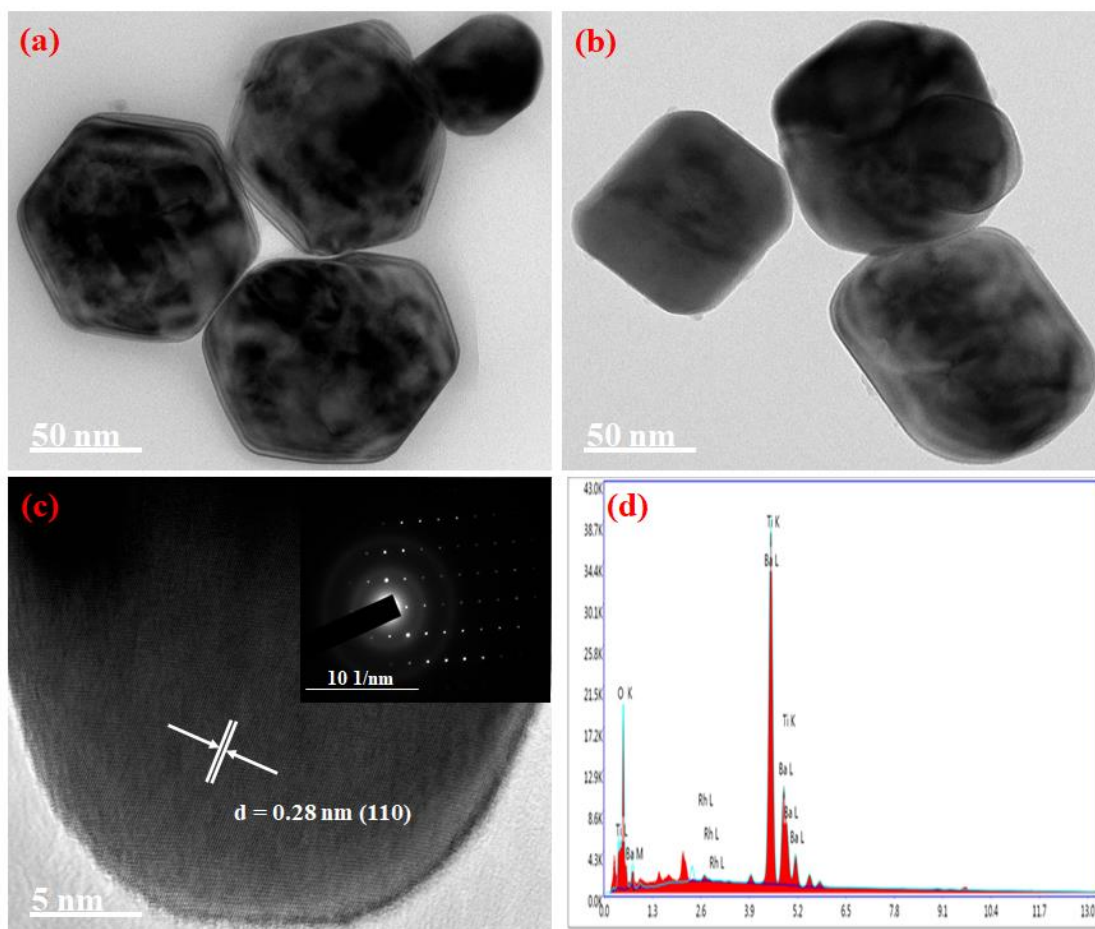


Figure 5.2 (a) TEM image of BaTiO₃, (b) TEM image of 0.5 Rh, (c) HRTEM of 0.5 Rh (inset shows SAED pattern of 0.5 Rh) and (d) EDX spectrum of 0.5 Rh.

5.3.3 BET Surface Area Analysis

Since the surface area of the sample plays a huge role in the catalysis process, The surface area of both doped and undoped BaTiO₃ was studied. In the nitrogen adsorption-desorption isotherms of BaTiO₃ and 0.5 Rh, a pattern of type IV with hysteresis loops being type H3 indicated the presence of slit-like pores (Figures 5.3 a and 5.3 b) (Sethi et al. 2020). The BET surface area was found to be 7 m²/g for 0.5 Rh which is higher as compared to pure BaTiO₃ (4.5 m²/g). This higher surface area of 0.5 Rh will be highly beneficial for the effective adsorption and degradation of the pollutants. A broad BJH pore size distribution in the range of 2-100 nm indicated the presence of mesopores and macropores (inset of Figures 5.3 a and 5.3 b). The pore volume of 0.5 Rh was found to be 0.0419 cm³/g which is almost twice that of the

pristine ($0.0229 \text{ cm}^3/\text{g}$), which helps in the efficient photo-absorption and diffusion of molecules during the photocatalytic reaction.

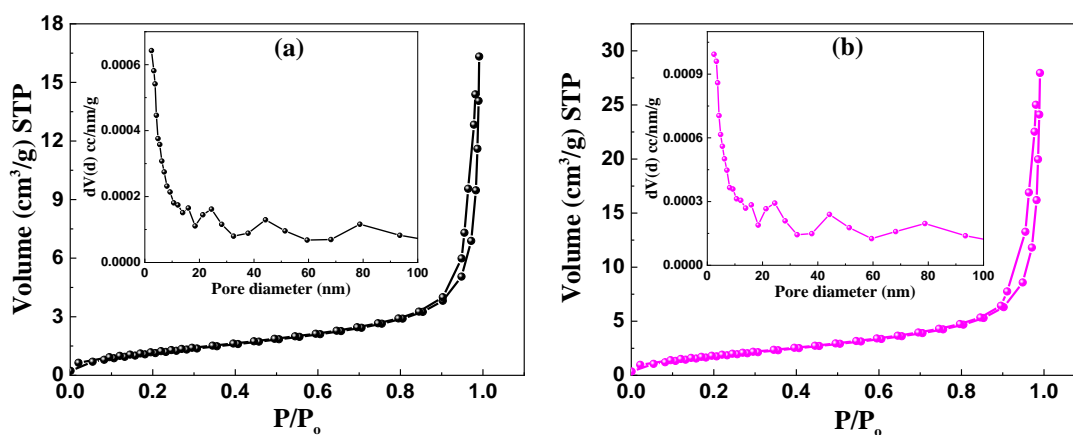


Figure 5.3 BET surface area analysis of (a) BaTiO₃ (inset shows pore size distribution) and (b) 0.5 Rh (inset shows pore size distribution).

5.3.4 XPS Analysis

XPS survey spectrum indicated the presence of Ba, Ti, O, and Rh species in the sample (Figure 5.4). It can be seen that Ba 3d has two spin states Ba 3d_{5/2} and Ba 3d_{3/2} which appear at binding energies of 778.74 eV and 794.03 eV, respectively as peaks (Figure 5.5 a). The binding energy separation of 15.29 eV between the two spin states of Ba confirmed the oxidation state of Ba in BaTiO₃ as +2 (Sadiq et al. 2018). The high-resolution spectrum of Ti indicates it is in +4 oxidation state as peaks emerge at binding energies of 458.42 eV (for Ti 2p_{3/2}) and 464.19 eV (for Ti 2p_{1/2}), respectively (Figure 5.5 b). Further, the peaks at binding energies 529.61 eV and 531.45 eV can be attributed to the lattice oxygen (O_L) and surface hydroxyl groups (O_{OH}), respectively (Figure 5.5 c) (Sethi et al. 2020, Amaechi et al. 2019). The deconvoluted peaks of Rh at binding energies 310.10 eV and 314.58 eV can be allotted to the Rh 3d_{5/2} and Rh 3d_{3/2} spin states, respectively (Figure 5.5 d). These binding energy values indicated the successful incorporation of Rh³⁺ ions into the lattice of the BaTiO₃ and not Rh⁴⁺ (Maeda 2014, Shenoy et al. 2018).

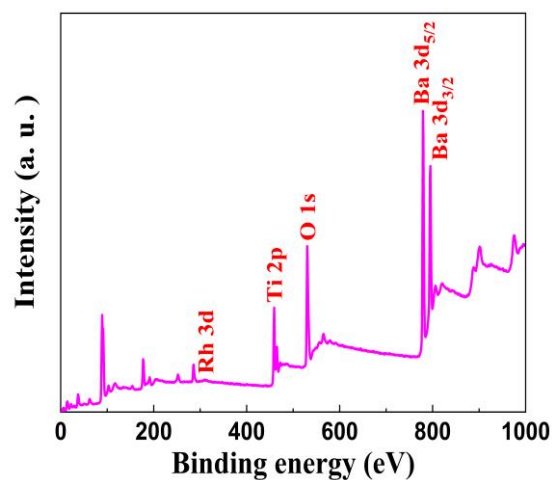


Figure 5.4 XPS survey spectrum of 0.5 Rh sample.

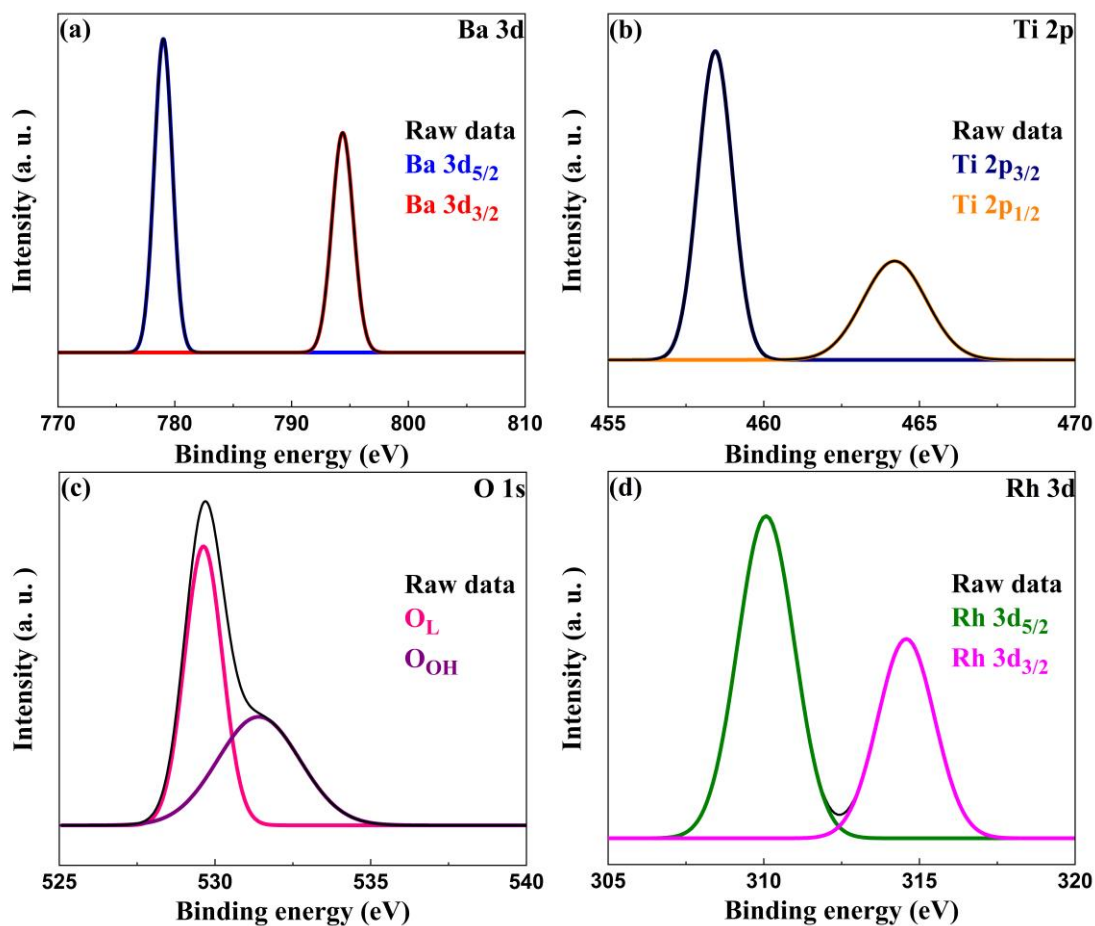


Figure 5.5 High-resolution XPS plot of (a) Ba 3d, (b) Ti 2p, (c) O 1s and (d) Rh 3d.

5.3.5 Optical Absorbance Analysis

In the DR spectra of pristine BaTiO₃, an absorption edge at around 400 nm can be seen due to the electronic transitions from the O 'p' orbitals to the Ti 'd' orbitals (Figure 5.6 a). Whereas, the absorption edges of Rh-doped samples are red-shifted to the visible region (400-550 nm) due to the decrease in the band gap. These wavelengths can be attributed to the electronic transitions from the donor level formed by the Rh³⁺ species to the conduction band of BaTiO₃. The characteristic absorption peak at 580 nm, caused by Rh⁴⁺, was absent indicating that Rh was doped in +3 oxidation state further confirming the results from XPS (Shenoy et al. 2018, Kawasaki et al. 2012).

The direct band gap of the samples was calculated using Tauc relation using equation 2.2. The band gap energies of BaTiO₃, 0.1 Rh, 0.3 Rh, 0.5 Rh and 0.7 Rh estimated from the respective absorption edge values were found to be 3.04 eV, 2.37 eV, 2.34 eV, 2.26 eV and 2.17 eV, respectively.

From the PL spectra of BaTiO₃ and Rh doped BaTiO₃, there is a noticeable drop in the fluorescence intensity can be seen for the doped samples as compared to pristine which indicates the lower opportunity for the recombination of photoinduced charges in the case of doped samples (Figure 5.6 b). The electrons are rapidly replenished to the vacant site by the VB which prevents their recombination with holes generated. Thus, more photoinduced holes and electrons can participate in the photocatalytic reactions. It can be noted that the PL intensity decreases till 0.5 Rh and beyond this concentration the PL intensity increases which can be attributed to the formation of recombination centers.

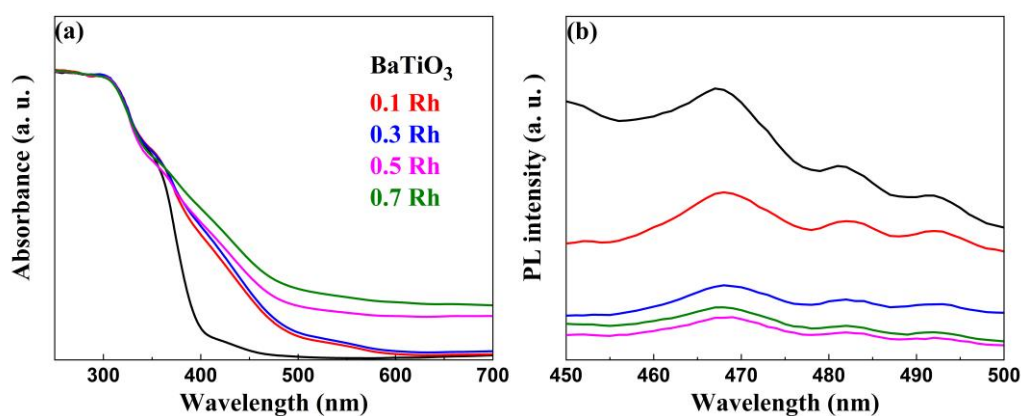


Figure 5.6 (a) DR and (b) PL spectra of BaTiO₃ and Rh doped BaTiO₃ samples.

5.3.6 Photocatalytic Activity

The photocatalytic efficiency of the synthesized materials was evaluated for the decomposition of MB dye under irradiation of visible light. Figure 5.7 a shows the photocatalytic degradation curves of MB in presence of BaTiO₃ and Rh-doped BaTiO₃ samples. The percentage degradation of BaTiO₃, 0.1 Rh, 0.3 Rh, 0.5 Rh, and 0.7 Rh was found to be 45, 55, 69, 96, and 73 respectively. The photocatalytic activity of Rh-doped samples was found to be higher than the pristine which could be attributed to the formation of Rh³⁺ donor levels above the VB which efficiently decreased the band gap enabling the harvesting of the visible light. 0.5 Rh exhibited the highest photocatalytic activity beyond which the activity decreased. This is due to the formation of recombination centers as revealed by the PL studies above. To further confirm this fact, 0.9 Rh sample was also synthesized and tested its photocatalytic activity and 0.9 Rh showed the least activity of 57% with a rate constant of 0.0068 min⁻¹.

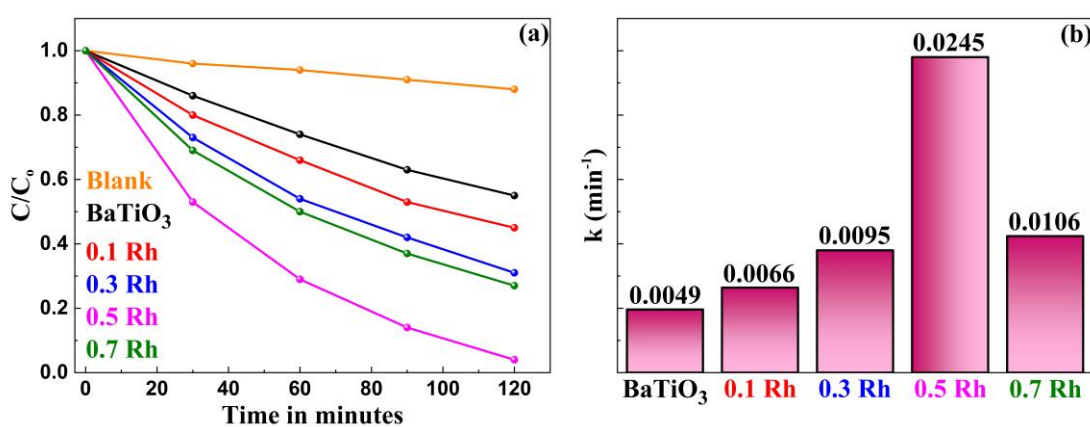


Figure 5.7 (a) Photocatalytic degradation curves and (b) rate constants of the BaTiO₃ and Rh-doped BaTiO₃.

The kinetics of the photocatalytic degradation of MB by BaTiO₃ and Rh-doped BaTiO₃ samples is well in agreement with the pseudo-first-order rate equation given by equation (2.3). The rate constant of 0.5 Rh was found to be higher than all the synthesized samples (Figure 5.7 b). Further, the 0.5 Rh showed only a marginal drop in the photocatalytic efficiency even after five consecutive cycles, suggesting its high stability and reusability towards photocatalytic degradation reactions (Figure 5.8).

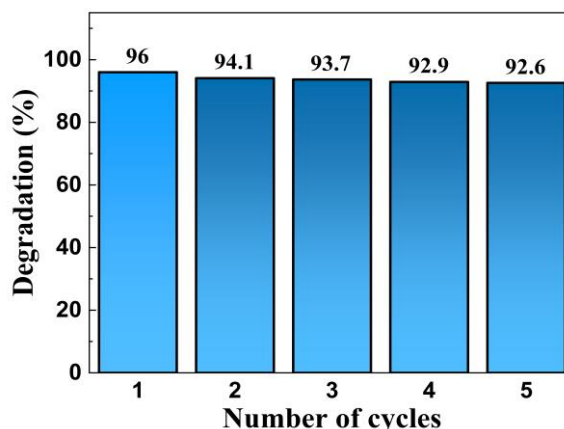


Figure 5.8 Cyclic stability of the synthesized 0.5 Rh.

From the Figure 5.9, it can be seen that superoxide radical anions are not the major active species as the corresponding scavenger benzoquinone did not deteriorate the photocatalytic activity to a larger extent. Whereas, the addition of potassium iodide and isopropyl alcohol reduced the photocatalytic activity significantly. As a result, holes followed by hydroxyl radicals are considered to be the active species for the effectual degradation of dye.

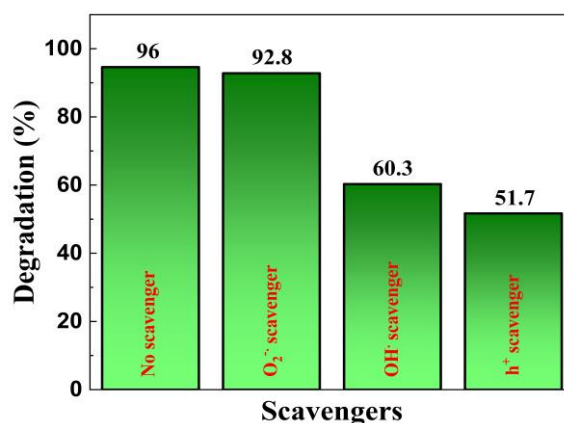


Figure 5.9 Effect of radical and hole scavengers on the photocatalytic degradation of MB by 0.5 Rh.

Based on the above study a mechanism for the photocatalytic degradation of MB dye as follows: When 0.5 Rh gets irradiated with energy greater than or equal to its bandgap, the electron from the donor levels formed by Rh³⁺ species is transferred to the CB. Later, these electrons react with oxygen to produce superoxide anion radicals. The formed holes either directly react with MB to produce degradation

products or react with surface hydroxyl groups to produce hydroxyl radicals. The formed superoxide and hydroxyl radicals react with dye molecules to produce harmless degradation products (Figure 5.10).

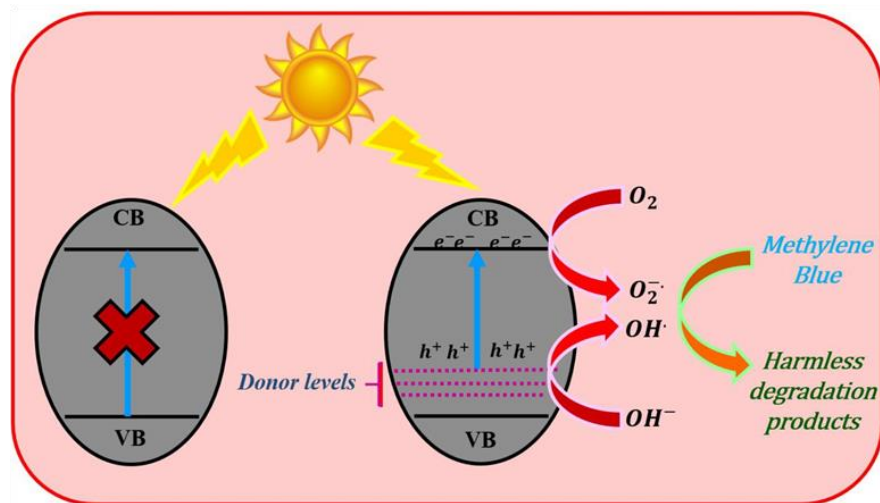


Figure 5.10 The photocatalytic mechanism of Rh-doped BaTiO₃ for the degradation of MB under visible light irradiation.

The thermodynamic parameters such as, activation energy (E_a), the free energy of activation (ΔG^\ddagger), enthalpy of activation (ΔH^\ddagger), and entropy of activation (ΔS^\ddagger) were computed as described in Chapter 2.

Table 5.1 Thermodynamic parameters of BaTiO₃ and Rh doped BaTiO₃ samples

Sample	E_a (kJ/mol)	ΔH^\ddagger (kJ/mol)	ΔS^\ddagger (kJ/mol)	ΔG^\ddagger (kJ/mol)
BaTiO ₃	13.2	10.7	-0.25	86.6
0.1 Rh	12.5	10.0	-0.25	85.9
0.3 Rh	11.6	9.1	-0.25	85.0
0.5 Rh	9.3	6.8	-0.25	82.7
0.7 Rh	11.3	8.8	-0.25	84.7
0.9 Rh	12.4	9.9	-0.25	85.8
Without catalyst	17.7	15.2	-0.25	91.2

From the values tabulated (Table 5.1), it can be observed that higher energy of activation is required for the photodegradation of MB without catalyst whereas relatively lower energy of activation is needed in the presence of BaTiO₃ and Rh doped samples. This shows that the catalyst alters the path of the reaction by lowering the activation energy barrier. 0.5 Rh sample exhibited the lowest activation energy as compared to other samples. The endothermic and non-spontaneous nature of the reaction was revealed by the positive enthalpy and free energy change.

CHAPTER 6

SOLVOTHERMAL SYNTHESIS OF POROUS GRAPHENE-BARIUM TITANATE NANOCOMPOSITE FOR PHOTOCATALYTIC APPLICATION

Chapter 6 presents and discusses the synthesis and photocatalytic activity of porous graphene-BaTiO₃ nanocomposite using a solvothermal approach.

6.1 INTRODUCTION

BaTiO₃ is a prominent semiconductor photocatalyst with distinguished ferroelectric, piezoelectric, and dielectric properties. As we know that its photocatalytic activity is restricted to the UV region of the solar spectrum, it is composited with electron-accepting materials like graphene to reduce the band gap and to enhance the lifetime of charge carriers.

A new form of graphene called PG is known to possess promising properties (Sethi et al. 2019). Thus, compositing BaTiO₃ with PG is expected to possess excellent photocatalytic efficiency. Even though the synthesis of BaTiO₃/graphene composites for photocatalytic applications have previously been reported, there have been no reports devoted to the synthesis of porous graphene-BaTiO₃ (PGBT) composite (Wang et al. 2015, Zhao et al. 2018, Mengting et al. 2019). PGST nanocomposite for photocatalytic degradation of MB was discussed in chapter 4 and the enhanced activity (~92 % in 120 minutes) was attributed to the high surface area, reduced band gap, and suppressed recombination rate of photoinduced charge carriers. Hence, the same approach was applied for its barium analogue.

Herein, PGBT composite was synthesized by a facile one-pot and reproducible solvothermal approach. The synthesized catalysts were systematically characterized by diffraction, microscopic and spectroscopic techniques to get more insight into the crystal structure, morphology, chemical environment, and optical properties. The photocatalytic efficiency of the synthesized PGBT composite was evaluated for the degradation of MB dye solution under visible light.

6.2 EXPERIMENTAL SECTION

6.2.1 Synthesis of PGBT Composite

All chemicals were procured from Sigma-Aldrich and were used as received without further purification. GO, PG and BaTiO₃ were synthesized according to the method discussed previously (Bhat et al. 2020, Sethi et al. 2019). ‘x PGBT’ (x = 2.5, 5.0, 7.5, 10.0, and 12.5 wt % GO) was synthesized by a simple one-pot solvothermal approach. A calculated amount of BaTiO₃ powder was added to the solution of GO

sonicated in a 1:1 water-ethylene glycol mixture and stirred for 3 hours to obtain a brownish-white suspension. The resultant mixture was sealed in an autoclave which was maintained at 160 °C for 16 hours. The obtained black precipitates were thoroughly washed with distilled water and dried in an oven at 70 °C for 8 hours. The composite obtained by taking 2.5, 5.0, 7.5, 10.0 and 12.5 wt % GO was designated as 2.5 PGBT, 5.0 PGBT, 7.5 PGBT, 10 PGBT and 12.5 PGBT, respectively. The details of other characterization tools employed and the procedure for the determination of photocatalytic activity are discussed in the previous chapters.

6.3 RESULTS AND DISCUSSION

6.3.1 XRD Analysis

XRD analysis was carried out in order to get more insight into the crystal structure and phase purity of the synthesized samples. All the diffraction peaks of PGBT samples shown in Figure 6.1 could be ascribed to the cubic phase of BaTiO₃ (JCPDS card No. 00-031-0174). A deviation in the 2θ value of (110) peak from 31.35° (BaTiO₃) to 31.47° (7.5 PGBT) suggests a strong interaction between the BaTiO₃ and the PG sheets in the composite. Scherrer equation was employed to calculate the average crystal sizes using (110) crystal planes and the values were found to be 45.2 nm, 35.36 nm, 33.1 nm, 32.2 nm, 29.34 nm, and 28.24 nm for BaTiO₃, 2.5 PGBT, 5.0 PGBT, 7.5 PGBT, 10 PGBT, and 12.5 PGBT, respectively. No characteristic peaks for PG are present in the PGBT samples due to their low content and relatively low diffraction intensity. However, its presence can be confirmed from Raman and XPS analysis.

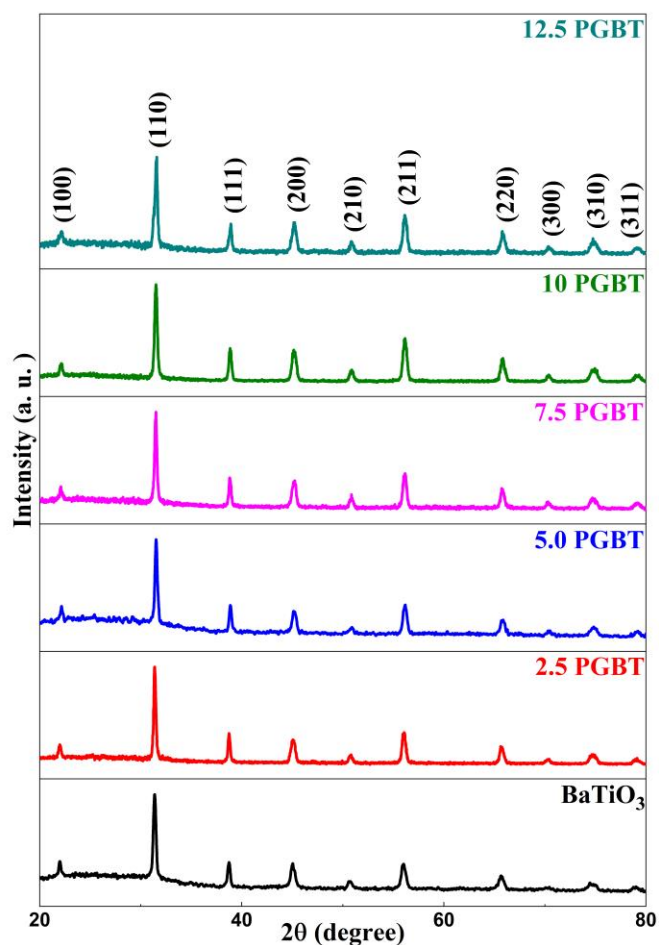


Figure 6.1 XRD patterns of BaTiO₃ and PGBT composites.

6.3.2 Raman Analysis

The Raman spectrum of PG displays a peak at 1346.1 cm⁻¹ (D band), which could be ascribed to the k-point phonons of A_{1g} symmetry of the sp³ defects, and another peak at 1595.1 cm⁻¹ (G band), which could be attributed to the E_{2g} graphite mode of the sp² bonded carbon atoms (Figure 6.2) (Sethi et al. 2019, Sadiq et al. 2017, Li et al. 2021). However, in the 7.5 PGBT, these peaks shift to 1347.5 cm⁻¹ and 1596.5 cm⁻¹, due to the chemical interaction between BaTiO₃ and PG. The intensity ratio of the D band to the G band (I_D/I_G) is a measure of the degree of defects. It can be observed that I_D/I_G in the case of 7.5 PGBT (0.91) is lower than that of PG (1.07) indicating strong adherence and interaction of BaTiO₃ nanoparticles on PG sheets (Sadiq et al. 2016, Sethi et al. 2020, Sethi et al. 2021).

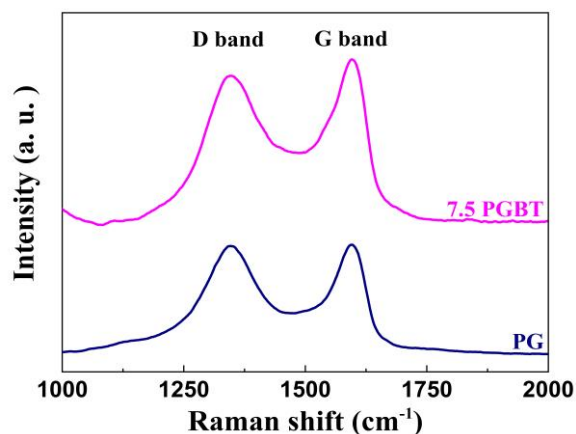


Figure 6.2 Raman spectra of PG and 7.5 PGBT.

6.3.3 TEM Analysis

TEM analysis was used to investigate the morphology of PG, BaTiO₃, and 7.5 PGBT samples. BaTiO₃ nanoparticles had roughly cuboctahedral shape tending towards spherical shape while PG revealed wrinkled nature with several pores (Figure 6.3 a and Figure 6.3 b). The TEM image of 7.5 PGBT revealed BaTiO₃ nanoparticles partially wrapped in PG facilitating easier migration and conduction of charge carriers (Figure 6.3 c). HRTEM of 7.5 PGBT showed the lattice fringes 0.28 nm apart corresponding to the (110) plane of BaTiO₃ (Figure 6.3 d).

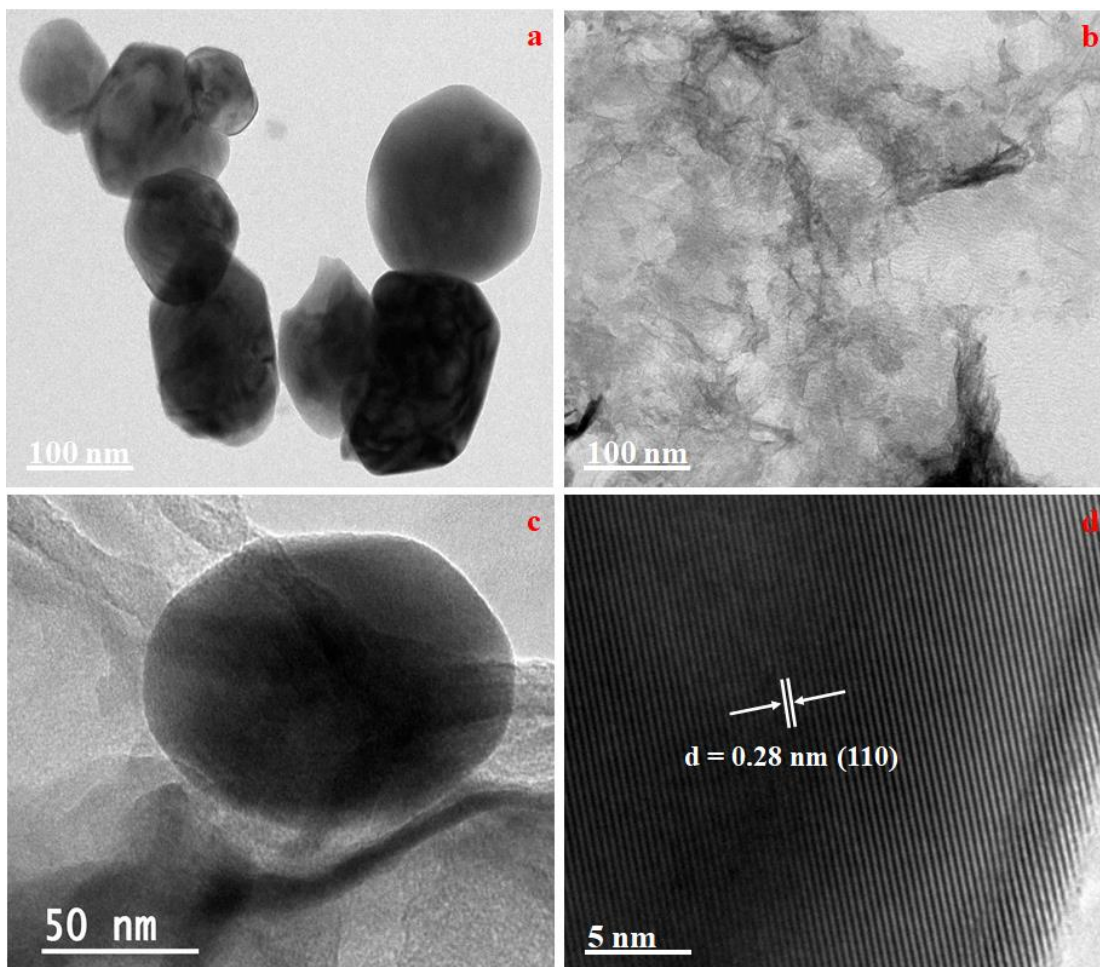


Figure 6.3 (a) TEM image of BaTiO₃, (b) TEM image of PG, (c) TEM image of 7.5 PGBT and (d) HRTEM image of 7.5 PGBT.

6.3.4 BET Surface Area Analysis

Figure 6.4 showed the nitrogen adsorption-desorption isotherm of the 7.5 PGBT sample. The isotherm exhibited a type IV characteristic with a hysteresis loop resembling type H3, indicating the presence of slit-like pores (Sethi et al. 2020). The BET-specific surface area of 7.5 PGBT was found to be 36 m²g⁻¹, which is eight times greater than the bare BaTiO₃ (4.5 m²g⁻¹). This enhanced surface area of the composite could be attributed to the presence of PG which provides more active sites for the efficient adsorption of MB dye molecules through π - π stacking. It also holds them in close proximity to the BaTiO₃ nanoparticles, as a result, the path length traveled by the active species reduces and hence boosts the photocatalytic activity. The BJH pore size distribution of 7.5 PGBT indicated the presence of mesopores and macropores

with a pore volume of $0.14 \text{ cm}^3\text{g}^{-1}$ (Figure 6.4 inset) which is almost six times higher than that of BaTiO_3 ($0.022 \text{ cm}^3\text{g}^{-1}$). Higher pore volume helps in the rapid diffusion of various reactants and products formed during the photocatalytic reaction.

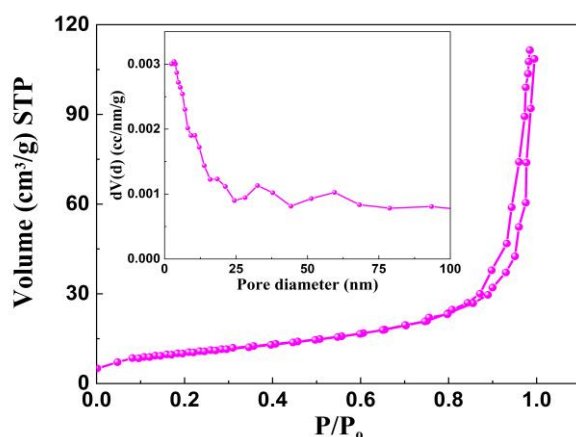


Figure 6.4 Nitrogen adsorption-desorption isotherm of 7.5 PGBT. The inset shows BJH pore size distribution.

6.3.5 XPS Analysis

XPS survey spectrum of 7.5 PGBT confirmed the presence of Ba, Ti, O, and C elements (Figure 6.5). High-resolution XPS along with the binding energy values of various elements present in 7.5 PGBT confirmed the presence of Ba in +2 state, and Ti in +4 state (Figure 6.6 and Table 6.1) (Bhat et al. 2020, Verhoeven and Van Doveren 1982, Zhou et al. 2021, Sethi et al. 2020, Sobahi and Amin 2021, Kappadan et al. 2020). The existence of chemical interaction between BaTiO_3 and PG is suggested by the formation of Ba-C bonds. The presence of the Ba-C bond helps in the efficient transport of carriers and better photocatalytic efficiency due to reduced recombination rate (Alamelu and Ali 2020, Boukhvalov et al. 2020).

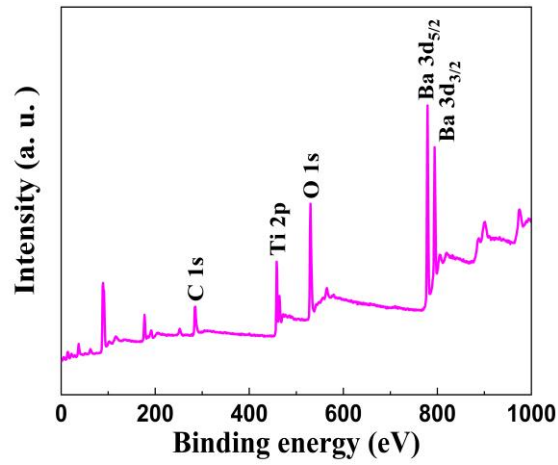


Figure 6.5 XPS survey spectrum of 7.5 PGBT sample.

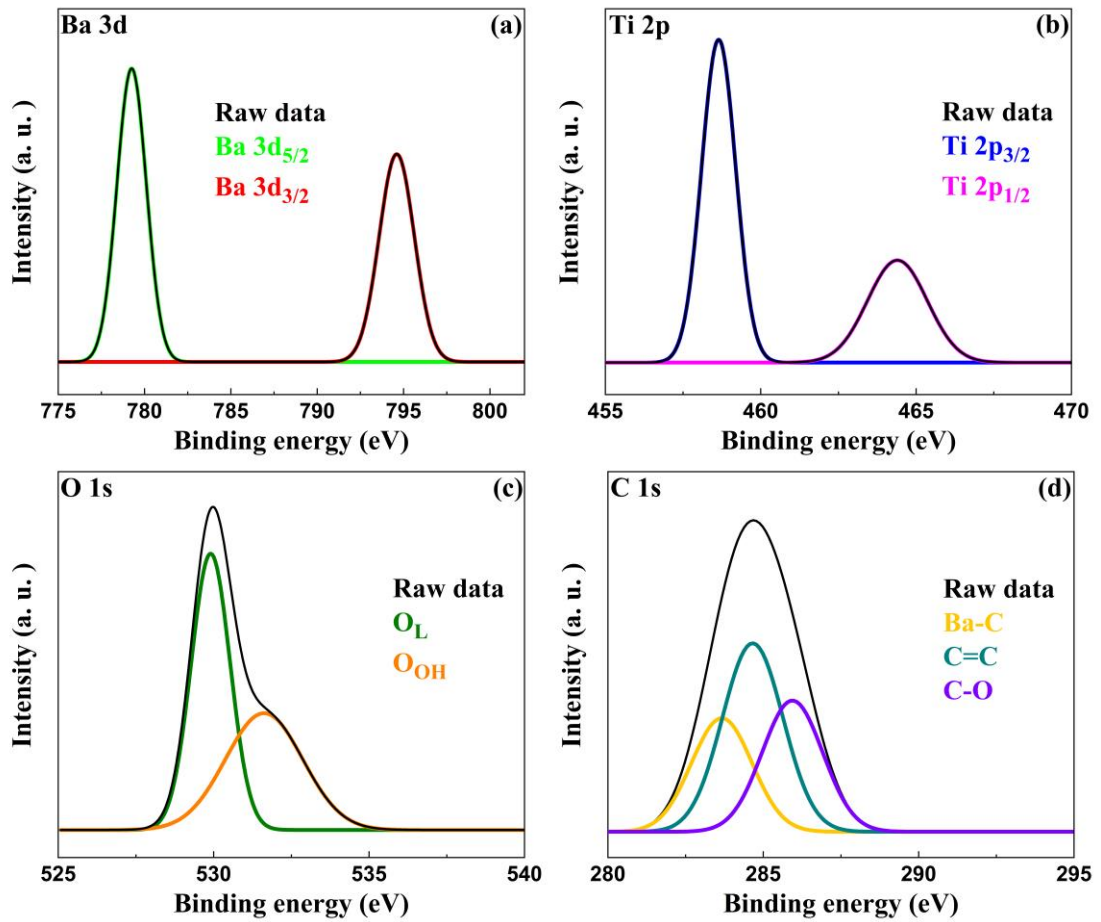


Figure 6.6 High-resolution XPS plot of (a) Ba 3d, (b) Ti 2p, (c) O 1s and (d) C 1s of 7.5 PGBT.

Table 6.1 XPS binding energy values of 7.5 PGBT.

Element	Binding energy (eV)	Assignment
Ba 3d	779.2	Ba 3d _{5/2}
	794.6	Ba 3d _{3/2}
Ti 2p	458.6	Ti 2p _{3/2}
	464.3	Ti 2p _{1/2}
O 1s	529.9	Lattice oxygen (O _L)
	531.6	Surface hydroxyl groups (O _{OH})
C 1s	283.6	Ba-C
	284.6	C=C
	285.9	C-O

6.3.6 Optical Absorbance Analysis

The effect of PG on the band gap energy of BaTiO₃ is studied by DRS analysis. From the DR spectra, it can be seen that the absorption edges of PGBT were red-shifted as compared to pristine BaTiO₃ (Figure 6.7 a). The band gap energies of the synthesized composites were derived from the Kubelka-Munk equation 3.1 (Shenoy and Bhat 2017). The band gap energies determined by plotting A/S versus energy of BaTiO₃, 2.5 PGBT, 5.0 PGBT, 7.5 PGBT, 10 PGBT and 12.5 PGBT were found to be 3.12 eV, 2.93 eV, 2.89 eV, 2.85 eV, 2.81 eV and 2.79 eV, respectively (Figure 6.7 b).

PL analysis was utilized to investigate the extent of the separation of charge carriers. The probability of involvement of the charge carriers in the photocatalytic reaction is decided by the lifetime of charge carriers before their recombination. The

lower recombination rate of photoinduced charge carriers and the efficient electron migration from BaTiO₃ to PG through the Ba-C bond is observed as a reduction in the fluorescence intensity (Figure 6.7 c). This indicates a greater probability of the charge carriers being involved in the photocatalytic reaction. However, beyond 7.5 PGBT, the enhancement in the fluorescence intensity can be observed which could be attributed to the superfluous PG which can act as a kind of recombination center (Song et al. 2018).

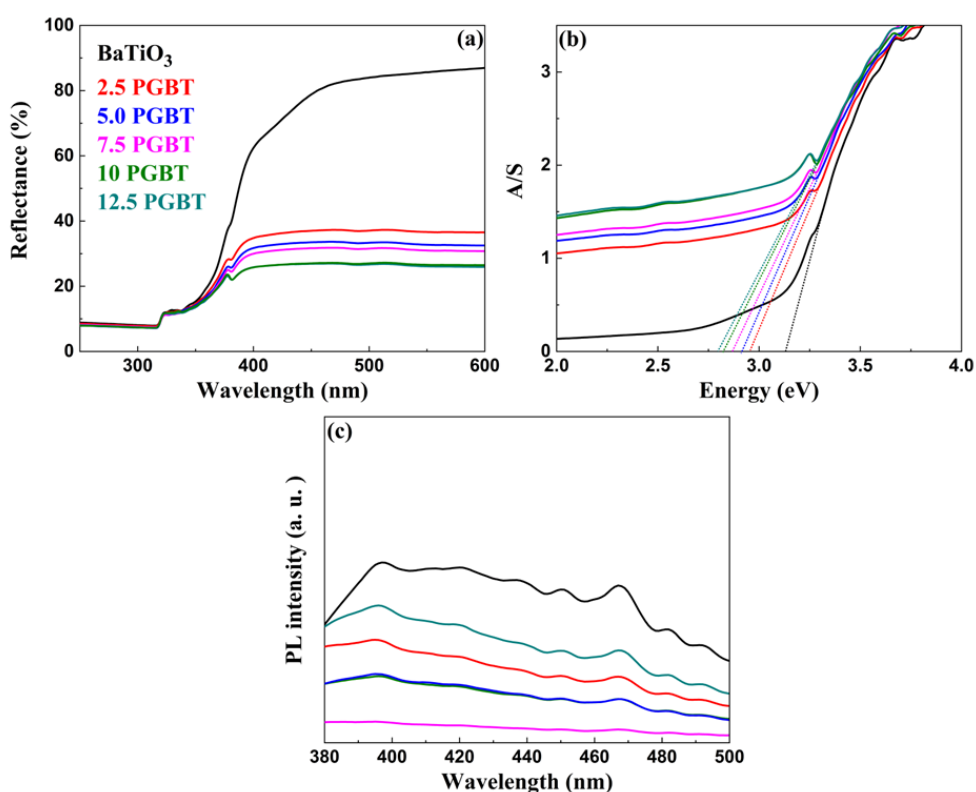


Figure 6.7 (a) UV-visible DR spectra, (b) electronic absorption spectra and (c) PL spectra of BaTiO₃ and PGBT.

6.3.7 Photocatalytic Activity

The percentage degradation of MB by BaTiO₃, 2.5 PGBT, 5.0 PGBT, 7.5 PGBT, 10 PGBT and 12.5 PGBT was found to be 34.7, 77.9, 85.1, 98.6, 87.6 and 62.9, respectively (Figure 6.8 a). The outstanding photocatalytic performance of 7.5 PGBT can be attributed to the shifting of absorption edge to the longer wavelength region of the solar spectrum allowing greater absorption of visible light, high specific surface area providing more active sites, and remarkable electrical transport property

of PG which lengthened the lifetime of photoinduced charge carriers. However, beyond 7.5 PGBT, the photocatalytic efficiency was found to be low due to hindrance in the absorption of light by BaTiO₃ due to excess PG and increase in recombination rate as confirmed by PL results.

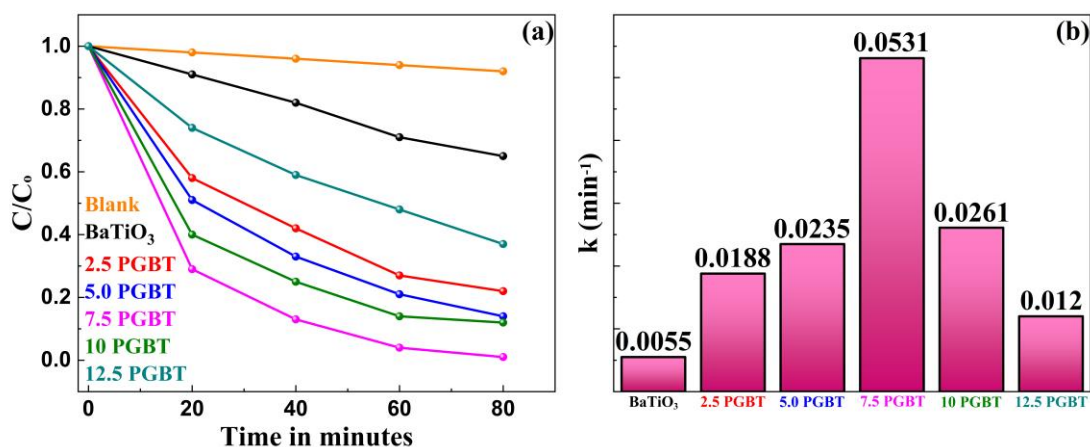


Figure 6.8 (a) Photocatalytic degradation curves and (b) rate constants for the photocatalytic degradation of MB by the synthesized BaTiO₃ and PGBT composites.

The above photocatalytic degradation reaction follows the pseudo-first-order rate equation 2.3. The rate constant of 7.5 PGBT was found to be 0.0531 min⁻¹, which is nearly 10 times higher than that of pristine (0.0055 min⁻¹) (Figure 6.8 b). The slight decline in the photocatalytic activity of 7.5 PGBT after seven consecutive cycles suggests its high stability (Figure 6.9).

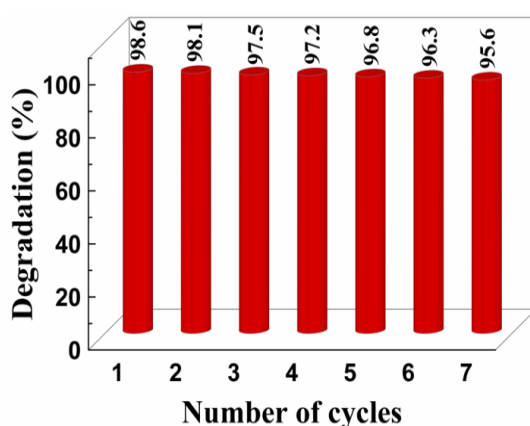


Figure 6.9 Cyclic stability of the synthesized 7.5 PGBT.

Further, the radical trapping experiments indicated that the holes and hydroxyl radicals are the major active species, as the addition of scavenging agents decreased

the photocatalytic rate, whereas superoxide anion radicals are the minor active species for the photocatalytic degradation of MB (Figure 6.10).

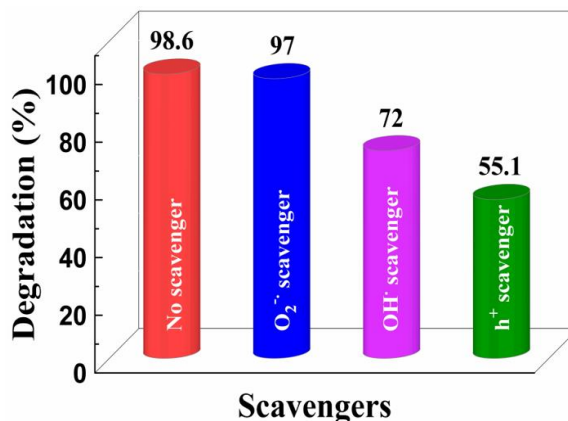


Figure 6.10 Effect of radical and hole scavengers on the photocatalytic degradation of MB by 7.5 PGBT.

The photocatalytic reaction is thought of to proceed as follows: when 7.5 PGBT absorbs a photon, an electron from the VB gets excited to the CB of BaTiO₃ leaving behind the positive hole in the VB. PG being an electron-accepting and transporting channel, the electrons from the BaTiO₃ nanoparticles transfer to the PG sheets through the Ba-C bonds, thereby significantly suppressing the recombination of photoinduced charge carriers and augment the photocatalytic activity (Figure 6.11). These electrons react with oxygen to produce superoxide anion radicals and the holes either directly oxidize MB or react with hydroxyl groups adsorbed on the surface to produce hydroxyl radicals. These generated active species react with MB molecules to produce CO₂ and H₂O.

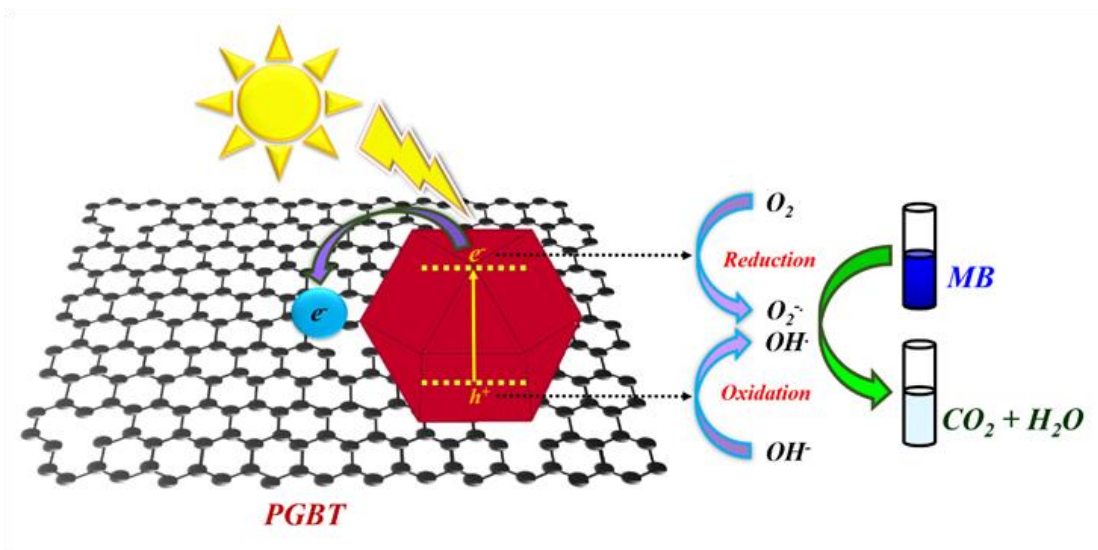


Figure 6.11 Mechanism of photocatalytic degradation of MB by PGBT.

The thermodynamic parameters such as, activation energy (E_a), the free energy of activation (ΔG^\ddagger), enthalpy of activation (ΔH^\ddagger), and entropy of activation (ΔS^\ddagger) were computed as described in Chapter 2.

Table 6.2 Thermodynamic parameters of BaTiO₃ and PGBT samples

Sample	E_a (kJ/mol)	ΔH^\ddagger (kJ/mol)	ΔS^\ddagger (kJ/mol)	ΔG^\ddagger (kJ/mol)
BaTiO ₃	12.97	10.48	-0.25	86.44
2.5 PGBT	9.91	7.41	-0.25	83.37
5.0 PGBT	9.35	6.86	-0.25	82.82
7.5 PGBT	7.32	4.82	-0.25	80.78
10 PGBT	9.09	6.60	-0.25	82.56
12.5 PGBT	11.03	8.53	-0.25	84.49
Without catalyst	17.7	15.2	-0.25	91.2

From Table 6.2, it can be seen that the activation energy (E_a) is higher for the photocatalytic degradation of MB without catalyst, whereas the energy of activation decreased in the presence of $BaTiO_3$ and PGBT samples. This confirms that the catalyst provides an alternate path for the reaction with a lower activation energy barrier. 7.5 PGBT sample exhibited the lowest activation energy as compared to other samples. The endothermic and non-spontaneous nature of the reaction was confirmed by the positive enthalpy change ($\Delta H^\#$) and free energy change ($\Delta G^\#$) values.

CHAPTER 7

SOLVOTHERMAL SYNTHESIS OF VANADIUM-DOPED CALCIUM TITANATE FOR PHOTOCATALYTIC APPLICATION

Chapter 7 presents and discusses the synthesis and photocatalytic activity of V-doped CaTiO₃ cuboids by a solvothermal approach.

7.1 INTRODUCTION

The band gap energy of CaTiO₃ is about 3.2 eV, as a result, its photocatalytic activity is restricted to the UV portion of the solar spectrum only and hence various strategies like doping, construction of heterostructures, and coupling with pi-conjugated structures have been utilized to reduce the band gap (Yan et al. 2020, Chen et al. 2020). Dopants are known to introduce bulk defects which can also act as recombination centers of photoinduced charges thus diminishing the photocatalytic efficiency of the material. Hence, it is imperative to find dopants that can efficiently harvest solar energy and also can suppress the recombination of photo-induced charge carriers. Various dopants such as Ag, Cr, Cu, Er, Eu, Fe, La, N, Na, and Zr have been utilized to improve the photocatalytic efficiency of CaTiO₃ (Chen et al. 2020, Zhang et al. 2012, Wang et al. 2018, Zhang et al. 2010, Lozano-Sanchez et al. 2015, Park 2019, Yang et al. 2014, Wang et al. 2018, Huang et al. 2016). In addition to this, co-doping has been utilized to passivate the unoccupied impurity states induced by mono-doped systems and thus suppress the recombination rate of photoinduced charges (Chen et al. 2020, Zhang et al. 2012, Wang et al. 2018).

Vanadium is a promising dopant in SrTiO₃ for photocatalytic degradation of MB (Bantawal et al. 2020). It is known that vanadium is a transition element that can exhibit multiple oxidation states. Hence, substitutional doping requires it to be introduced with an isovalent charge to avoid the formation of the so-called in-gap states acting as recombination centers due to the formation of oxygen vacancies. Hence, there is a dire need to develop a novel and eco-friendly synthetic technique which can avoid the formation of defect states.

Herein, for the first time, V-doped CaTiO₃ was synthesized by a facile one-pot solvothermal approach by avoiding high-temperature calcination. The photocatalytic activity of the material was tested using MB dye as a model pollutant.

7.2 EXPERIMENTAL SECTION

7.2.1 Synthesis

All the chemicals were purchased from Sigma-Aldrich and were used as received. Titanium(IV) isopropoxide (1.47 mL) was dissolved in 10 mL of 2-propanol. To this, a calculated amount of vanadyl acetylacetonate was added and stirred for one hour. An appropriate amount of calcium nitrate tetrahydrate and 15 mL of 2 M KOH were added. The resultant mixture was sealed in an autoclave and kept in a hot air oven maintained at 180 °C for 24 hours. The resultant precipitates were washed thoroughly with acetic acid and water. The washed products were dried in an oven at 70 °C for 8 hours. The products obtained by using 0.25, 0.5, 1.0, 1.5 and 2.0 mol % of the V precursor were labelled as 0.25 V, 0.5 V, 1.0 V, 1.5 V and 2.0 V respectively. The details of other characterization tools employed and the procedure for the determination of photocatalytic activity are discussed in the previous chapters.

7.3 RESULTS AND DISCUSSION

7.3.1 XRD Analysis

The XRD diffraction profiles of CaTiO₃ and V-doped CaTiO₃ can be well-matched with the orthorhombic phase of CaTiO₃ with JCPDS card number 42-0423 (Figure 7.1). There is no characteristic peak of vanadium oxide in the XRD profiles of V-doped CaTiO₃, indicating the successful incorporation of V into the host lattice of CaTiO₃. The shift in the 2θ values after V doping is negligible due to the similar radius of V⁴⁺ and Ti⁴⁺ ions. If V is doped in the Ca site, then an appreciable shift would have been observed as Ca²⁺ ions are larger compared to V⁴⁺ ions. The average crystallite sizes of the synthesized samples were calculated with the help of the Scherrer equation by using the diffraction angle and FWHM values of the (121) crystal plane. The crystallite sizes were found to be 36.46 nm, 37.45 nm, 44.73 nm, 45.47 nm, 46.23 nm, and 47.83 nm for CaTiO₃, 0.25 V, 0.5 V, 1.0 V, 1.5 V, and 2.0 V, respectively. The increase in the crystallite sizes with an increase in doping points towards the increased crystallinity due to favored directional growth with an increase in the concentration of the V dopant (Liu et al. 2009, Wu and Chen 2004).

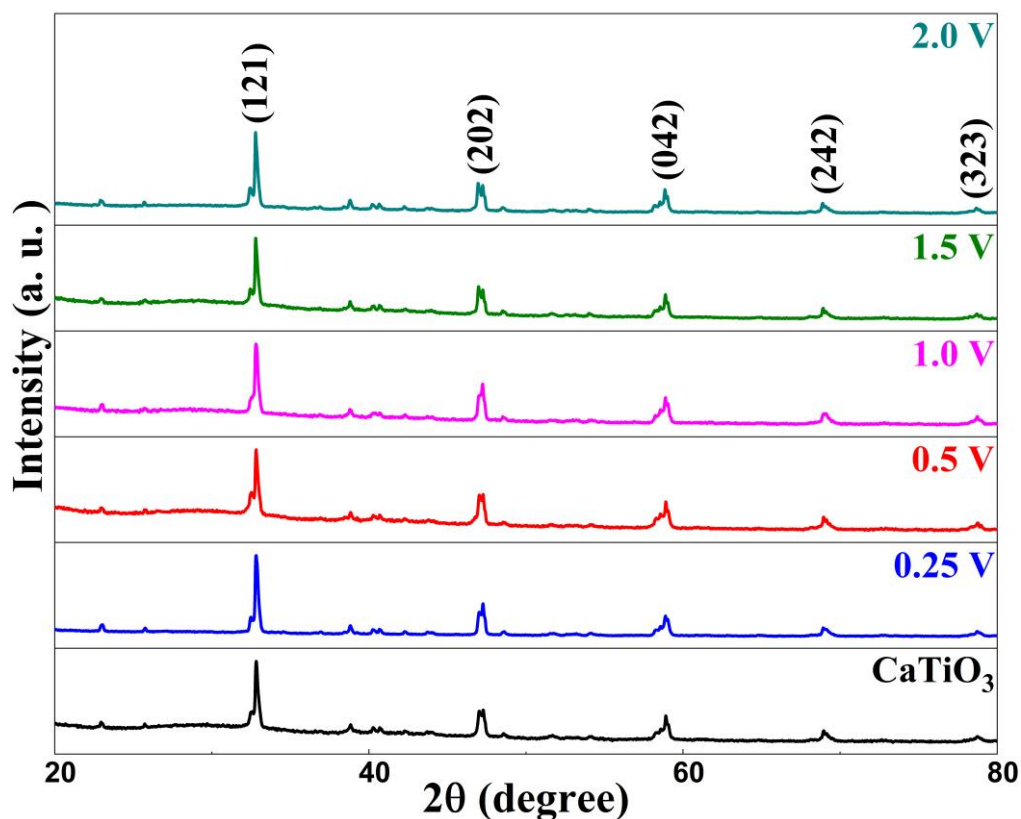


Figure 7.1 XRD patterns as a function of the doping concentration of V.

7.3.2 FESEM and TEM analysis

The morphology of the doped CaTiO_3 was studied with the help of FESEM and TEM analysis. From the FESEM image, It can be seen that V-doped CaTiO_3 has cuboidal morphology (Figure 7.2 a). This fact is further supported by TEM analysis (Figure 7.2 b). V doping showed no change in the morphology of CaTiO_3 . HRTEM analysis of 1.0 V revealed lattice fringes with 0.27 nm spacing, which could be indexed to the (121) plane of CaTiO_3 (Figure 7.2 c). The selected area electron diffraction (SAED) pattern indicated the single-crystalline nature of the material (Figure 7.2 d).

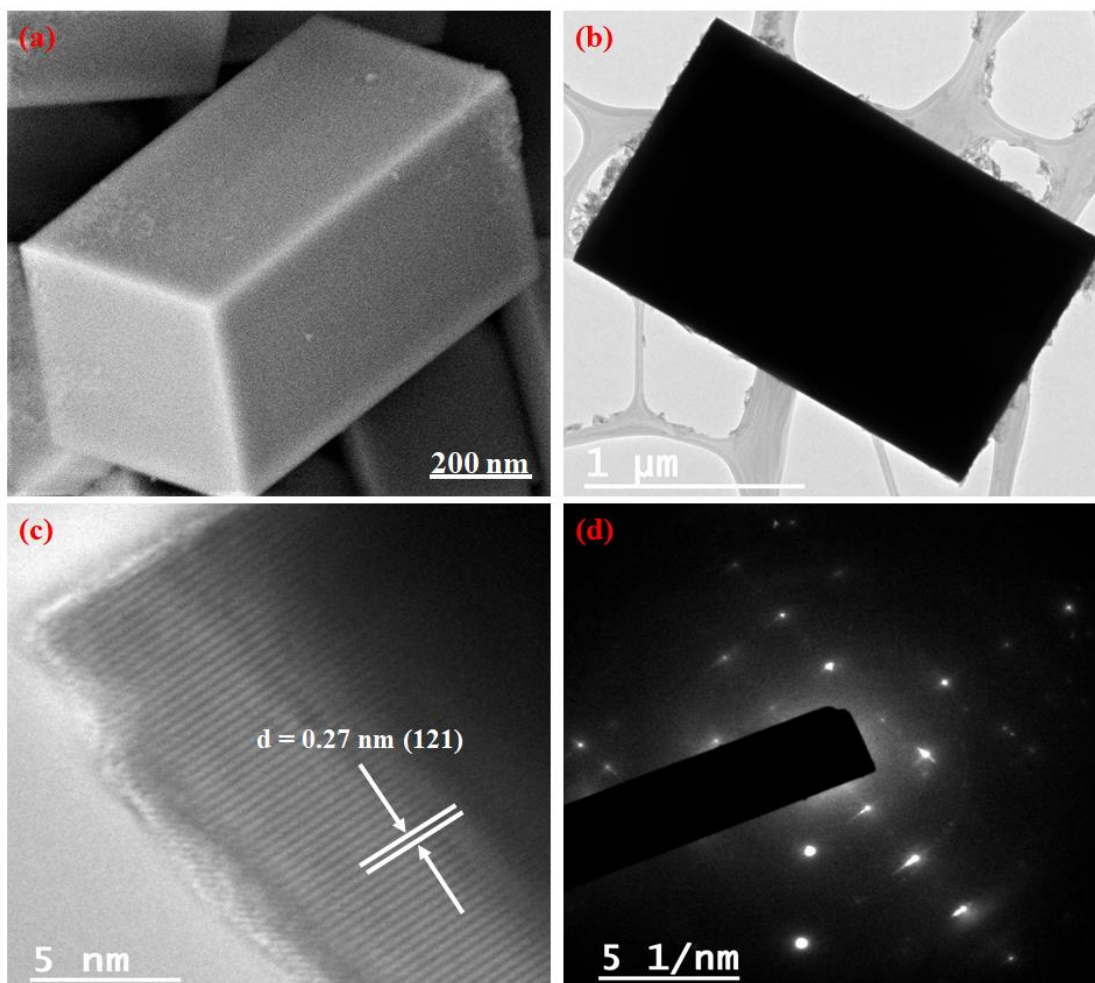


Figure 7.2 (a) FESEM image, (b) TEM image, (c) HRTEM image and (d) SAED pattern of 1.0 V.

7.3.3 BET Surface Area Analysis

The textural properties of the undoped CaTiO_3 and 1.0 V were investigated by BET analysis. The nitrogen adsorption-desorption isotherms indicated a type IV pattern with the hysteresis loops resembling type H3 ($P/P_0 > 0.4$), revealing the presence of slit-like pores (Figures 7.3 a and b) (Ren et al. 2020). The BET surface area of 1.0 V was found to be $21.78 \text{ m}^2\text{g}^{-1}$ which is higher in comparison to CaTiO_3 ($15.88 \text{ m}^2\text{g}^{-1}$), which enables the efficient adsorption and degradation of the pollutants by enhancing the surface-active sites. The BJH pore size distributions of the pure CaTiO_3 and 1.0 V samples presented a narrow distribution ranging from 3 to 6.6 nm indicating the presence of mesopores (insets of Figures 7.3 a and b). The pore volume of 1.0 V was found to be $0.0270 \text{ cm}^3\text{g}^{-1}$ which is slightly higher than that of CaTiO_3

($0.0240 \text{ cm}^3\text{g}^{-1}$), facilitating effective diffusion of molecules during the photocatalytic reaction.

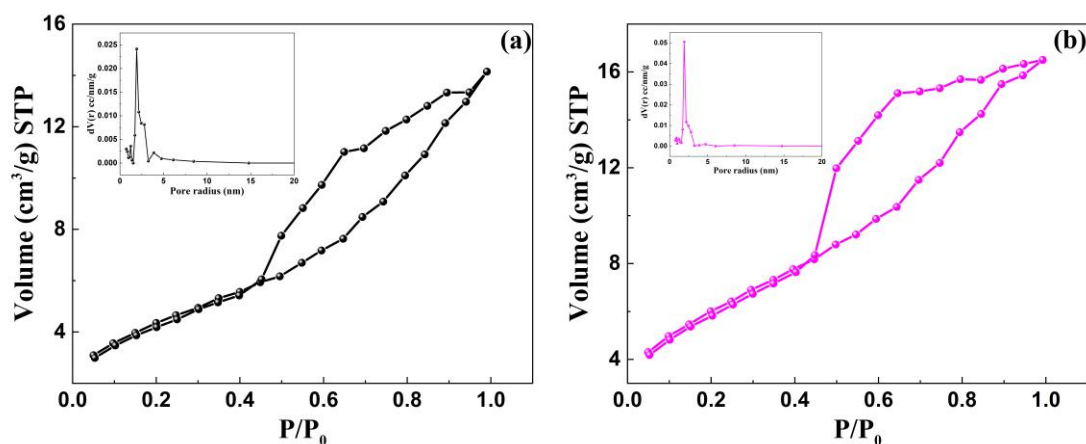


Figure 7.3 Nitrogen adsorption-desorption isotherms and BJH pore size distribution (inset) of (a) CaTiO_3 and (b) 1.0 V.

7.3.4 XPS Analysis

The XPS survey spectrum of CaTiO_3 indicated the presence of Ca, Ti, O, and V elements (Figure 7.4). The double peaks at the binding energies of 346.7 eV and 350.3 eV could be attributed to Ca $2p_{3/2}$ and Ca $2p_{1/2}$ spin states of Ca^{2+} , respectively in 1.0 V (Figure 7.5 a) (Jiang et al. 2020). The peaks at the binding energies of 458.8 eV and 464.6 eV could be ascribed to Ti $2p_{3/2}$ and Ti $2p_{1/2}$ states, respectively. These binding energy values confirmed the existence of the +4 oxidation state for Ti in the 1.0 V sample (Figure 7.5 b) (Bhat et al. 2020). The binding energies of 530.2 eV and 531.7 eV could be attributed to O^{2-} in the lattice (O_L) and the hydroxyl groups adsorbed on the surface (O_{OH}), respectively in 1.0 V (Figure 7.5 c) (Cai et al. 2020). The double peaks at the binding energies of 515.9 eV and 523.3 eV could be ascribed to V $2p_{3/2}$ and V $2p_{1/2}$ states, respectively, indicating the oxidation state of V as +4 (Figure 7.5 d) and the successful incorporation of V in CaTiO_3 (Top et al. 2018, Vattikuti et al. 2018, Li et al. 2020). The maintenance of charge neutrality in the crystal thus avoids the formation of defect states and hence prevents recombination of charge carriers and enhances the carrier lifetime. The doping site of V in CaTiO_3 can also be determined experimentally using the XPS technique. The V doping resulted in the shifting of the XPS peak of Ca 2p from 346.2 eV for CaTiO_3 to 346.7 eV for 1.0

V whereas, the XPS peak of Ti 2p from 458.1 eV for CaTiO₃ to 458.8 eV for 1.0 V. This strongly suggests that the incorporated V has more effect on the Ti site than the Ca site, which can be considered as the evidence for Ti site substitution (Figure 7.6).

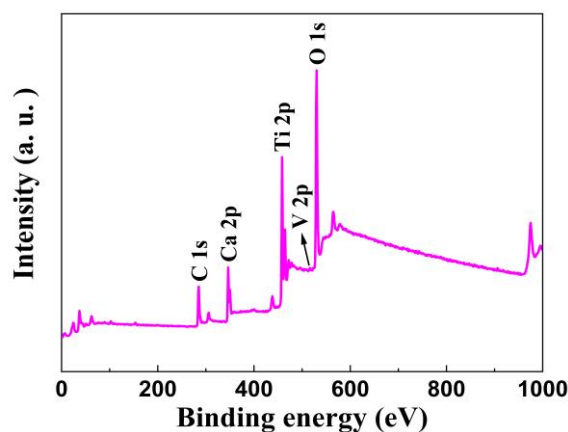


Figure 7.4 XPS survey spectrum of 1.0 V sample.

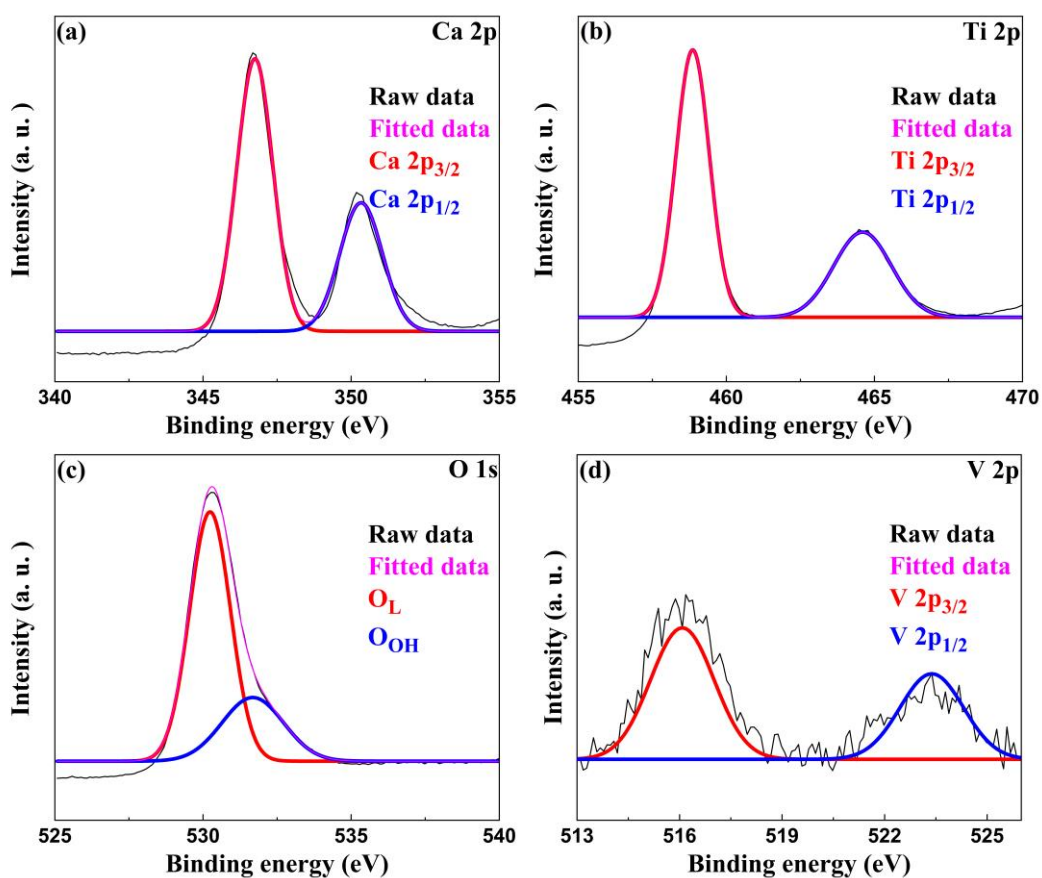


Figure 7.5 High resolution XPS spectrum of (a) Ca 2p, (b) Ti 2p, (c) O 1s and (d) V 2p of 1.0 V.

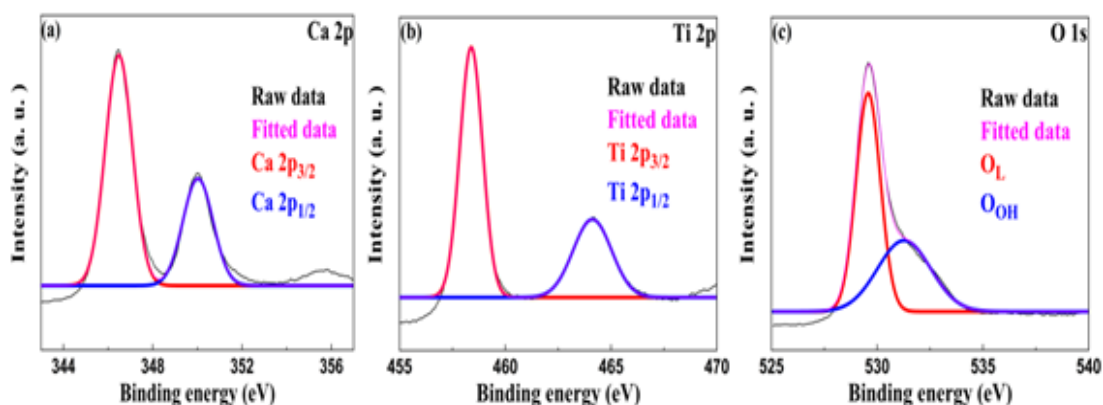


Figure 7.6 High resolution XPS spectrum of (a) Ca 2p, (b) Ti 2p and (c) O 1s of CaTiO₃.

7.3.5 Optical Absorbance Analysis

As shown in Figure 7.7 a, the absorption edge of V-doped CaTiO₃ was red-shifted as compared to pristine CaTiO₃. This could be attributed to the insertion of the t_{2g} level of the V 3d orbital within the band gap. The absorption data were derived using the Kubelka-Munk equation 3.1 (Shenoy and Bhat 2017). The band gap energies of CaTiO₃, 0.25 V, 0.5 V, 1.0 V, 1.5 V and 2.0 V were found to be 3.28 eV, 2.41 eV, 2.33 eV, 2.23 eV, 2.12 eV and 2.03 eV, respectively (Figure 7.7 b).

PL analysis was carried out in order to get more insight into defect chemistry and charge recombination behavior of the synthesized materials. As shown in Figure 7.7 c, the V-doped CaTiO₃ sample exhibited inferior fluorescence intensity in comparison to pristine CaTiO₃ which could be attributed to the incorporation of V in the isovalent state, thus suppressing the formation of the recombination centers. Among the different samples, 1.0 V showed the least PL intensity and as a result, it is expected to show the highest photocatalytic activity.

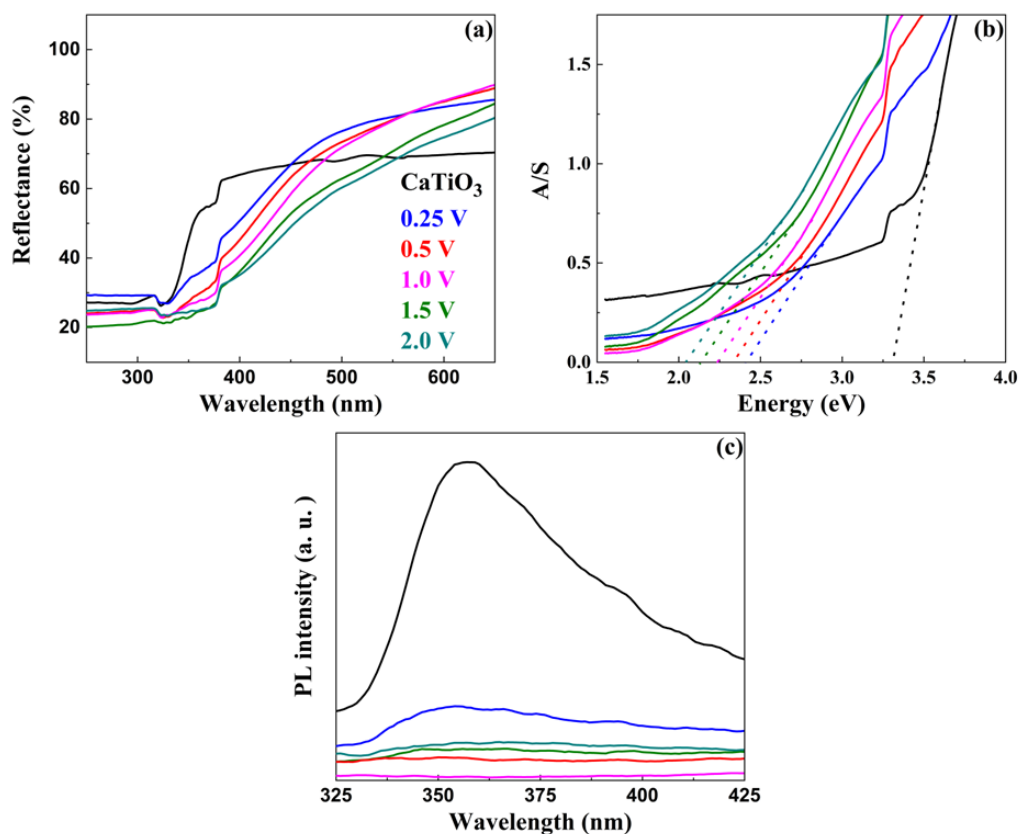


Figure 7.7 (a) UV-visible DR spectra, (b) electronic absorption spectra and (c) PL spectra of CaTiO₃ and V-doped CaTiO₃ samples.

7.3.6 Photocatalytic Activity

The photocatalytic activity of the synthesized catalysts was evaluated for the degradation of MB dye solution under visible light. Figure 7.8 a shows the photocatalytic degradation of MB as a function of irradiation time in the presence of CaTiO₃ and V-doped CaTiO₃ samples. The photocatalytic activity of V-doped CaTiO₃ samples was found to be higher than that of CaTiO₃ which could be attributed to the introduction of additional energy levels just beneath the CB effectively decreasing the band gap and reduction in the recombination of the photoinduced charges due to efficient charge separation. Among the various V-doped samples, 1.0 V exhibited the highest photocatalytic activity, beyond which the photocatalytic activity decreases. This reduction in photocatalytic activity can be attributed to the formation of recombination centers as confirmed by PL analysis. In addition to this,

the 1.0 V sample exhibited a higher surface area which enables the efficient adsorption and degradation of the pollutants during the photocatalytic reaction.

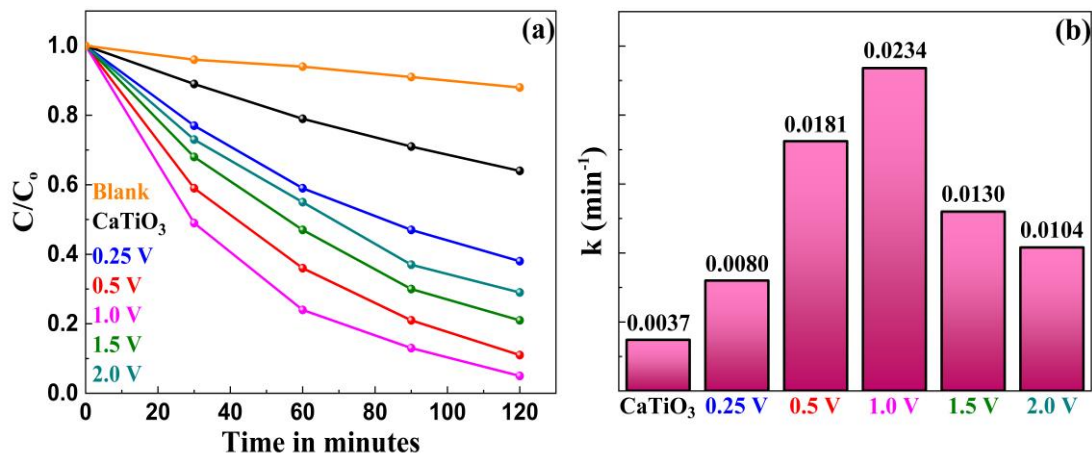


Figure 7.8 (a) The photocatalytic degradation curves and (b) the rate constants of the photocatalytic degradation of MB by the synthesized CaTiO₃ and V-doped CaTiO₃.

The degradation kinetics of MB by CaTiO₃ and V-doped CaTiO₃ is well fitted with the pseudo-first-order rate equation given by equation 2.3 (Sadiq et al. 2017). The rate constant of 1.0 V was found to be higher than that of all the other samples indicating the higher efficiency of the material (Figure 7.8 b). Further, 1.0 V exhibited high stability towards the photocatalytic degradation reactions as 1.0 V just showed a slight decline in the photocatalytic activity even after seven consecutive cycles (Figure 7.9).

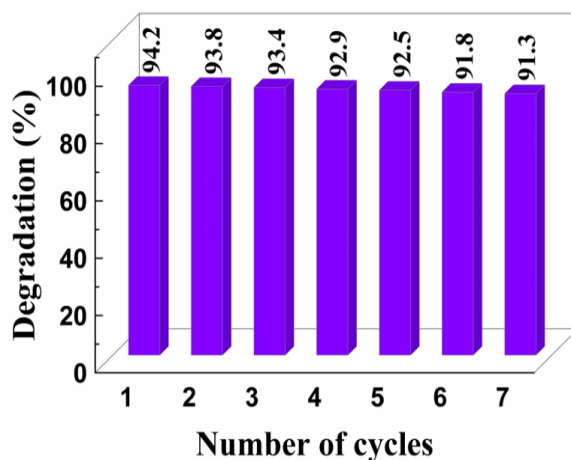


Figure 7.9 Cycling stability of the synthesized 1.0 V.

From Figure 7.10, it can be seen that, superoxide anion radicals are not the major active species as the corresponding scavenger benzoquinone did not deteriorate the photocatalytic activity much. This is also confirmed by the band edge positions as a decrease in the band gap with V doping brings the potential of the CB lower than the potential for the generation of superoxide anion radicals. Further, the addition of potassium iodide (hole scavenger) and isopropyl alcohol (OH^\cdot scavenger) reduced the photocatalytic activity significantly. As a result, holes followed by hydroxyl radicals are considered to be the active species for the effective degradation of the dye.

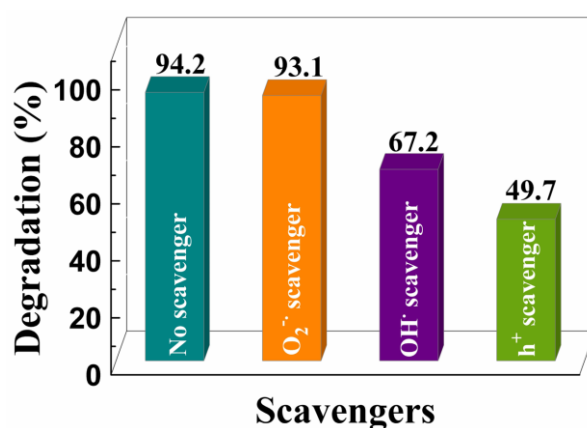


Figure 7.10 Effect of radical and hole scavengers on the photocatalytic degradation of MB by 1.0 V.

The mechanism of photocatalytic degradation of MB can be stated as follows: when V-doped CaTiO_3 is irradiated with an energy equal to or greater than its band gap, electrons from the VB get excited to the energy levels created by V just beneath the CB edge generating the corresponding number of holes in the VB. These electrons react with oxygen to produce superoxide radicals ($\text{O}_2^{\cdot-}$). The holes in the VB either directly react with MB or react with surface hydroxyl groups to produce hydroxyl radicals (OH^\cdot). The formed radicals are said to be active species for the effective degradation of MB to carbon dioxide and water (Figure 7.11).

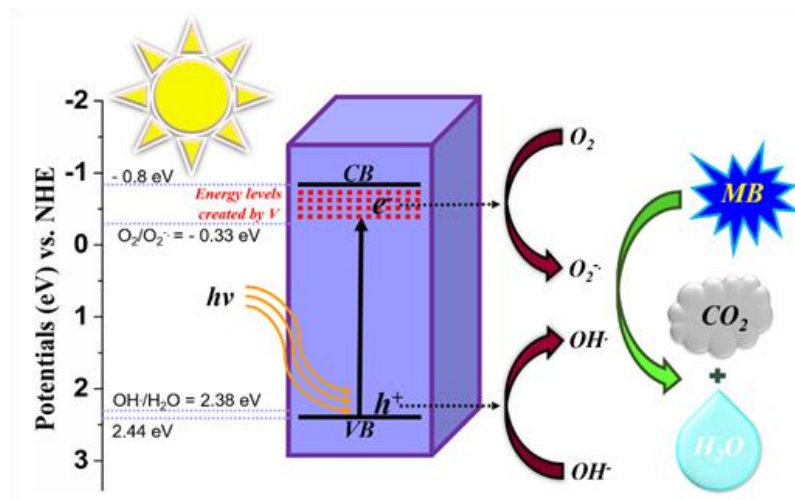


Figure 7.11 Proposed mechanism for the photocatalytic degradation of MB under visible light irradiation.

The thermodynamic parameters such as, activation energy (E_a), the free energy of activation (ΔG^\ddagger), enthalpy of activation (ΔH^\ddagger), and entropy of activation (ΔS^\ddagger) were computed as described in Chapter 2.

Table 7.1 Thermodynamic parameters of CaTiO_3 and V doped CaTiO_3 samples

Sample	E_a (kJ/mol)	ΔH^\ddagger (kJ/mol)	ΔS^\ddagger (kJ/mol)	ΔG^\ddagger (kJ/mol)
CaTiO_3	13.9	11.5	-0.25	87.4
0.25 V	12.0	9.5	-0.25	85.5
0.5 V	10.0	7.5	-0.25	83.5
1.0 V	9.4	6.9	-0.25	82.8
1.5 V	10.0	8.3	-0.25	84.3
2.0 V	10.8	8.9	-0.25	84.9
Without catalyst	17.7	15.2	-0.25	91.2

From the values tabulated (Table 7.1), it can be seen that higher energy of activation is required for the photodegradation of MB without the catalyst, whereas relatively lower energy of activation is needed in the presence of CaTiO_3 and V-doped CaTiO_3 catalysts. This confirms that the catalyst alters the path of the reaction by lowering the activation energy barrier. The 1.0 V sample exhibited the lowest activation energy as compared to other samples. The endothermic and non-spontaneous nature of the reaction was indicated by the positive enthalpy and free energy change.

CHAPTER 8

SOLVOTHERMAL SYNTHESIS OF POROUS GRAPHENE-CALCIUM TITANATE NANOCOMPOSITE FOR PHOTOCATALYTIC APPLICATION

Chapter 8 presents and discusses the synthesis and photocatalytic activity of porous graphene-CaTiO₃ nanocomposite by a solvothermal approach.

8.1 INTRODUCTION

It is well known that compositing with 2D materials and doping with metallic or non-metallic ions are the most promising strategies employed to improve the photocatalytic efficiency of CaTiO₃ (Kumar et al. 2017, Chen et al. 2020). Doping is known to be an effective technique for the extension of visible light response of wide band gap photocatalyst but on the other side known to introduce undesirable in-gap states which function as recombination centers, thus limiting the photocatalytic efficiency of the material. In addition, weak carrier transport results in a suppressed lifetime of photogenerated charges. As a result, coupling CaTiO₃ with efficient conducting support is necessary to enable the rapid delivery of charge carriers to the reaction site.

A new form of graphene called PG is known to possess promising properties (Sethi et al. 2019). Hence, it is interesting to enhance the photocatalytic activity of CaTiO₃ by compositing with PG. Keeping all these points in view it was found that there have been no reports devoted to the synthesis and photocatalytic activity of porous graphene-CaTiO₃ (PGCT) composite. In Chapter 5 and Chapter 7, the photocatalytic performances of PGST and PGBT composites were discussed and were found to be highly promising. Motivated by these results, the photocatalytic property of PGCT composite is investigated.

Herein, PGCT composite was synthesized by a facile solvothermal approach. The synthesized materials were carefully analyzed by various advanced characterization techniques to obtain more information on the purity, crystal structure, morphology, elemental oxidation states, and optical properties. MB dye solution was considered as a model pollutant for the determination of the photocatalytic activity of the synthesized composite materials.

8.2 EXPERIMENTAL SECTION

8.2.1 Synthesis

All the chemicals were purchased from Sigma-Aldrich and were used as received. GO and PG were synthesized according to the reported method (Sethi et al.

2019). ‘x PGC’ (x = 2.5, 5.0, 7.5, 10.0, and 12.5 wt % GO) was synthesized by a simple solvothermal approach as follows: A calculated amount of CaTiO₃ powder was added to the solution of GO sonicated in 1:1 water-ethylene glycol mixture and stirred for 3 hours to obtain a brownish white suspension. The resultant suspension was sealed in an autoclave and kept at 160 °C for 16 hours. The obtained black precipitates were thoroughly washed with distilled water and dried in an oven at 70 °C for 8 hours. The composite obtained by taking 2.5, 5.0, 7.5, 10.0, and 12.5 wt % GO was represented as 2.5 PGCT, 5.0 PGCT, 7.5 PGCT, 10 PGCT, and 12.5 PGCT, respectively. The details of other characterization tools employed and the procedure for the determination of photocatalytic activity are discussed in the previous chapters.

8.3 RESULTS AND DISCUSSION

8.3.1 XRD Analysis

The XRD patterns of the pure CaTiO₃ and the PGCT composites with varying concentrations of PG could be indexed to the orthorhombic phase of CaTiO₃ with JCPDS card number 42-0423 (Figure 8.1). A small shift in the diffraction angle of (121) plane from 32.83° (CaTiO₃) to 32.89° (7.5 PGCT) indicates a plausible interaction between the CaTiO₃ and the PG sheets in the composite. Notably, no typical diffraction peaks for PG are present in the composite materials which might be due to the trace amount of PG with the low atomic number which cannot be detected by the diffractometer. The average crystal sizes of the synthesized samples were calculated by using the values of diffraction angles and FWHM of (121) plane with the help of the Scherrer equation and the values were found to be 36.5 nm, 29.7 nm, 29.4 nm, 29.0 nm, 28.9 nm and 28.1 nm for CaTiO₃, 2.5 PGCT, 5.0 PGCT, 7.5 PGCT, 10 PGCT, and 12.5 PGCT, respectively.

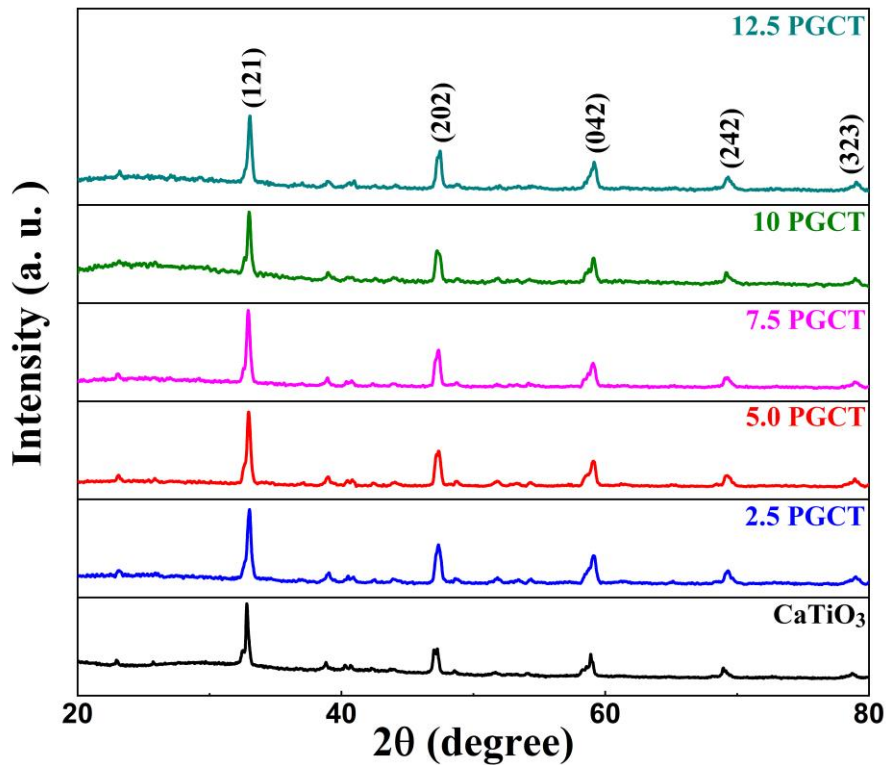


Figure 8.1 XRD patterns of CaTiO₃ and PGCT samples.

8.3.2 Raman Analysis

Raman analysis was carried out to confirm the presence of PG in the composite sample. PG reveals a peak at 1347.2 cm⁻¹ (D band), which could be assigned to the breathing mode of A_{1g} symmetry of the phonons near the k-point, and another peak at 1596.2 cm⁻¹ (G band), which could be ascribed to the in-plane vibration of carbon atoms in sp² hybridized states (Figure 8.2) (Sethi et al. 2019). Notably, in the case of the 7.5 PGCT sample, these peaks shift to 1350.2 cm⁻¹ and 1593.2 cm⁻¹, which can be due to the possible chemical interaction between the CaTiO₃ and the PG sheets. The degree of defects was derived from the intensity ratio of the D band to the G band (I_D/I_G) (Wang et al. 2020). The I_D/I_G value in the case of 7.5 PGCT (0.91) is lower than that of PG (1.07) which can be due to the successful incorporation of CaTiO₃ cuboids on PG sheets (Sadiq et al. 2016, Sethi et al. 2021).

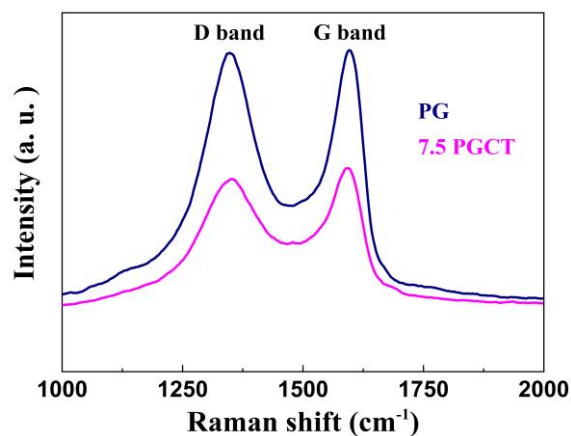


Figure 8.2 Raman spectra of PG and 7.5 PGCT.

8.3.3 FESEM and TEM Analysis

The morphology of PG, CaTiO₃, and 7.5 PGCT samples was investigated using electron microscopy. CaTiO₃ particles exhibited a cuboidal shape while PG revealed wrinkled nature with many pores (Figure 8.3 a and Figure 8.3 b). The TEM image of 7.5 PGCT indicated CaTiO₃ cuboids partially wrapped in PG expediting smooth migration and conduction of charge carriers (Figure 8.3 c). SAED pattern of 7.5 PGCT revealed the single-crystalline nature of the sample (Figure 8.3 d).

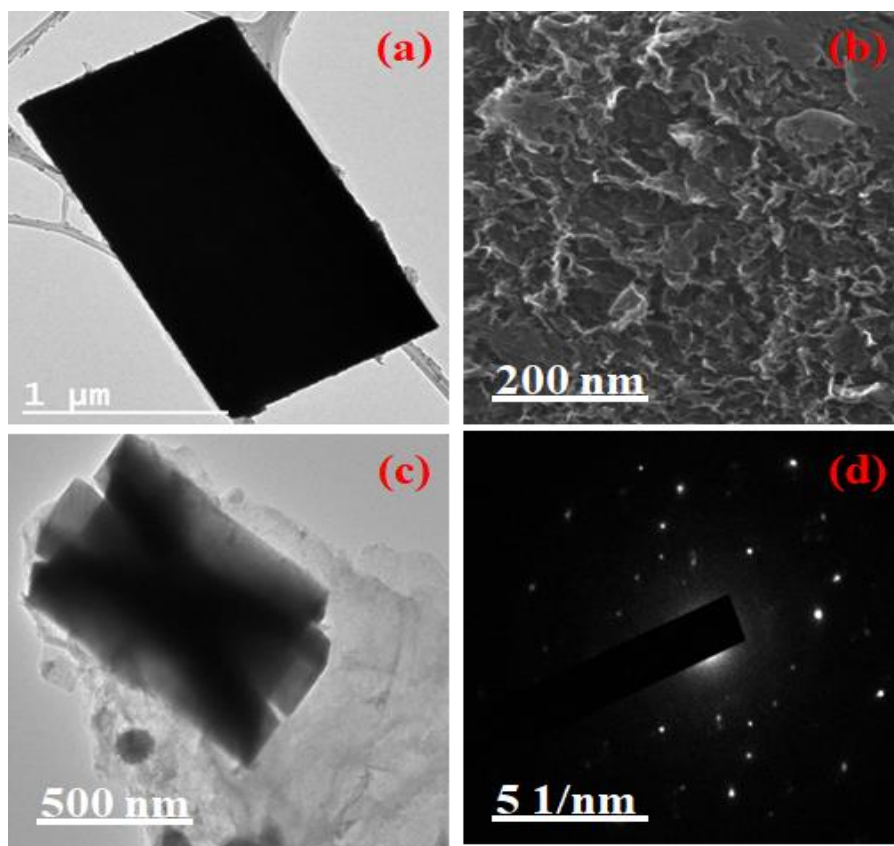


Figure 8.3 (a) TEM image of CaTiO_3 , (b) FESEM image of PG, (c) TEM image of 7.5 PGCT, and (d) SAED pattern of 7.5 PGCT.

8.3.4 BET Surface Area Analysis

Nitrogen adsorption-desorption isotherm of the 7.5 PGCT sample is shown in Figure 8.4. The isotherm can be classified as type IV with hysteresis loop H3 which is a characteristic of mesoporous materials (Sethi et al. 2020). The BET-specific surface area of 7.5 PGCT was found to be $31.9 \text{ m}^2\text{g}^{-1}$, which is higher than the pure CaTiO_3 ($15.88 \text{ m}^2\text{g}^{-1}$). This larger surface area of the composite could be ascribed to the presence of PG which has an extremely high surface area. The pore size distribution of the 7.5 PGCT was analyzed by BJH analysis and is shown in the inset of Figure 8.4. It can be seen that the pore size is mainly concentrated in the range of 2-50 nm which indicates the presence of mesopores with a pore volume of $0.0891 \text{ cm}^3\text{g}^{-1}$ which is higher than that of pure CaTiO_3 ($0.0240 \text{ cm}^3\text{g}^{-1}$). Higher surface area and pore volume increase the photocatalytic activity due to enhanced adsorption of dye

molecules and rapid transport of various reactants and products formed during the photocatalytic reaction.

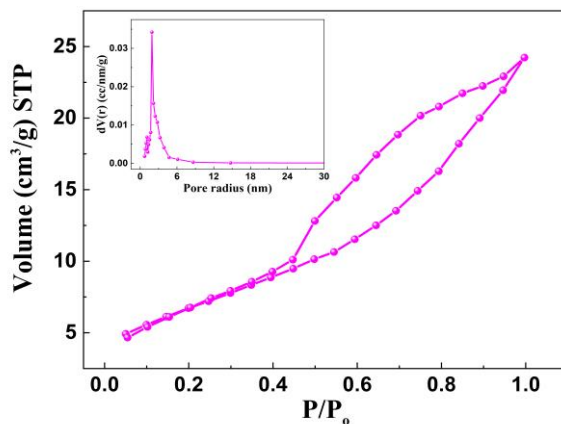


Figure 8.4 Nitrogen adsorption-desorption isotherm and BJH pore size distribution (inset) of 7.5 PGCT.

8.3.5 XPS Analysis

XPS survey spectrum of 7.5 PGCT indicated the presence of Ca, Ti, O, and C elements (Figure 8.5). The binding energy values of various elements in the high-resolution XPS spectra of 7.5 PGCT indicated the presence of Ca in +2 state, Ti in +4 state (Figure 8.6 and Table 8.1) (Sethi et al. 2021, Yan et al. 2020, Nishikiori et al. 2019, Shi et al. 2018, Jiang et al. 2019, Sun et al. 2019). The formation of these Ti-O-C bonds elucidated the existence of chemical interaction between CaTiO₃ and PG which helps in the effective transport of carriers and thus promotes photocatalytic activity (Boukhvalov et al. 2020, He et al. 2018).

Table 8.1 XPS binding energy values of 7.5 PGCT

Element	Binding energy (eV)	Assignment
Ca 2p	347.3	Ca 2p _{3/2}
	350.9	Ca 2p _{1/2}
Ti 2p	459.2	Ti 2p _{3/2}
	464.9	Ti 2p _{1/2}
O 1s	530.5	Lattice oxygen (O _L)
	533.1	Surface hydroxyl groups (O _{OH})
	531.6	Ti-O-C
C 1s	284.7	C=C
	286.7	C-OH
	289.1	O-C=O

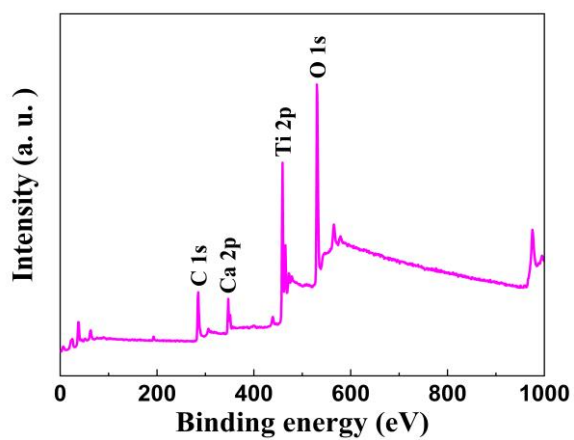


Figure 8.5 XPS survey spectrum of 7.5 PGCT sample.

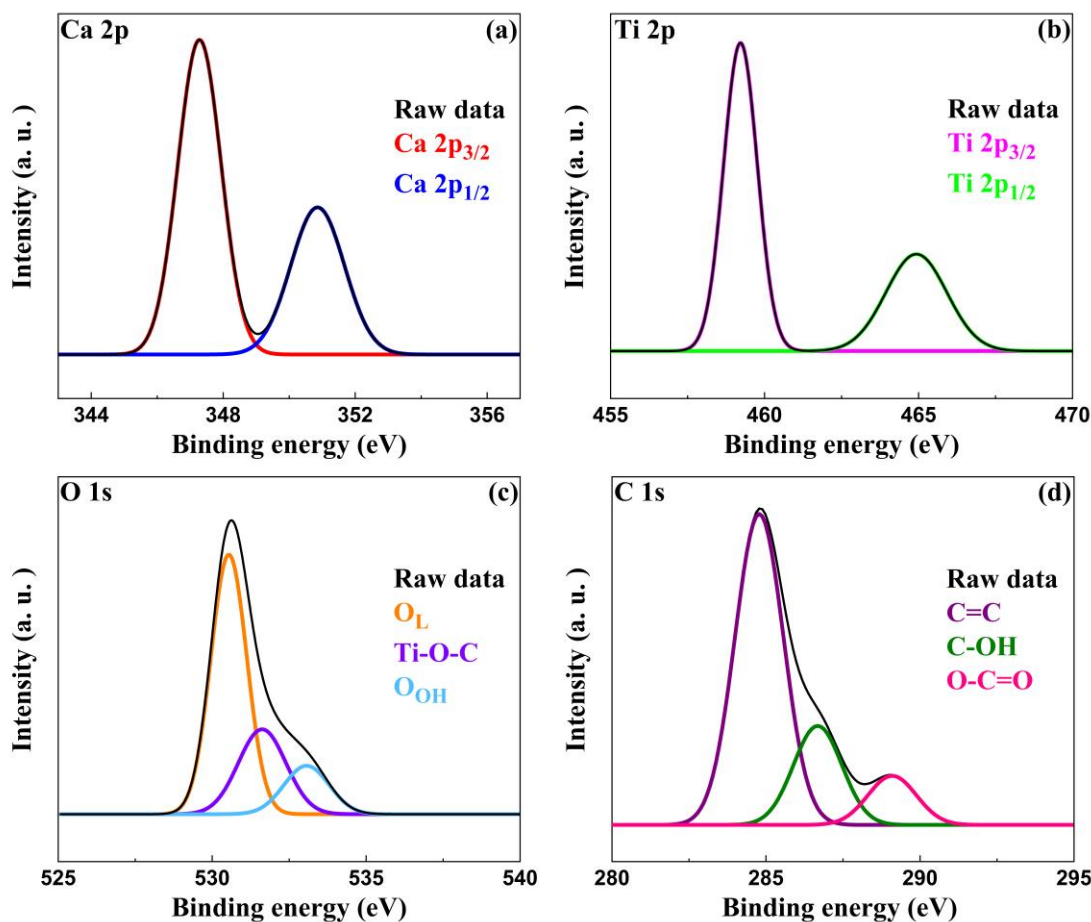


Figure 8.6 High resolution XPS plot of (a) Ca 2p, (b) Ti 2p, (c) O 1s and (d) C 1s of 7.5 PGCT.

8.3.6 Optical Absorbance Analysis

The optical absorption properties of the synthesized materials were investigated by DRS analysis. From the DR spectra, it can be seen that the absorption edges of PGCT were shifted to the longer wavelength side as compared to bare CaTiO_3 (Figure 8.7 a). The energy band gap of the synthesized catalysts was obtained from the Kubelka-Munk equation (3.1) (Shenoy and Bhat 2017). The band gap energies were determined by plotting A/S versus energy and the values were turned out to be 3.2 eV, 3.12 eV, 2.94 eV, 2.77 eV, 2.60 eV, and 2.51 eV for CaTiO_3 , 2.5 PGCT, 5.0 PGCT, 7.5 PGCT, 10 PGCT, and 12.5 PGCT respectively (Figure 8.7 b).

PL analysis has been widely used to investigate the lifetime of photoinduced charge carriers. From the PL spectra, a significant reduction in the fluorescence intensity of composite materials as compared to bare CaTiO₃ was observed which can be attributed to the efficient electron transport from CaTiO₃ to PG through the Ti-O-C bond thus enhancing the lifetime of photogenerated charge carriers (Figure 8.7 c). However, beyond 7.5 PGCT, the fluorescence intensity was found to be enhanced which could be attributed to the excessive graphene which can act as recombination centers (Liu et al. 2019).

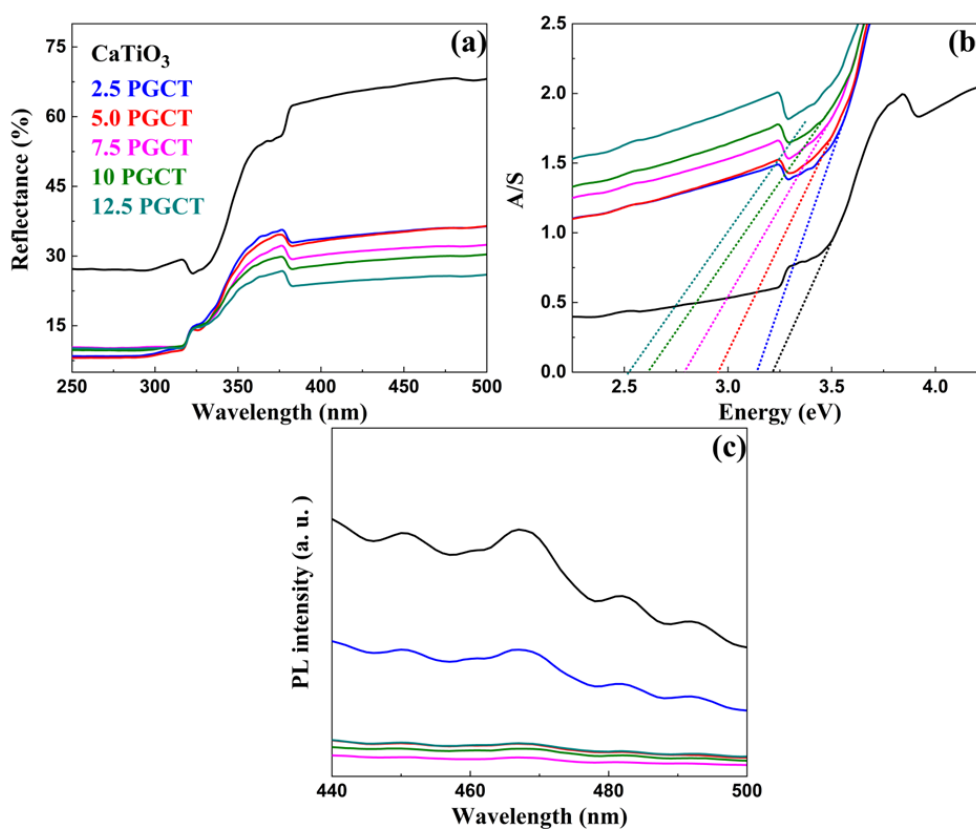


Figure 8.7 (a) UV-visible DR spectra, (b) electronic absorption spectra and (c) PL spectra of CaTiO₃ and PGCT.

8.3.7 Photocatalytic Activity

The percentage of MB removal by the CaTiO₃, 2.5 PGCT, 5.0 PGCT, 7.5 PGCT, 10 PGCT, and 12.5 PGCT was found to be 14.0, 74.0, 88.0, 98.1, 90.0, and 80.0, respectively (Figure 8.8 a). The outstanding photocatalytic efficiency of 7.5 PGCT can be ascribed to the improved optical absorption ability in the visible region

of the solar spectrum, large surface area which provides more surface-active sites for the efficient adsorption of MB, and effective interfacial charge transfer through the Ti-O-C bond. However, at higher concentrations of PG (i.e., beyond 7.5 PGCT), the photocatalytic efficiency was found to be low due to the light-shielding effect caused by PG and also the formation of recombination centers as confirmed from the above PL results.

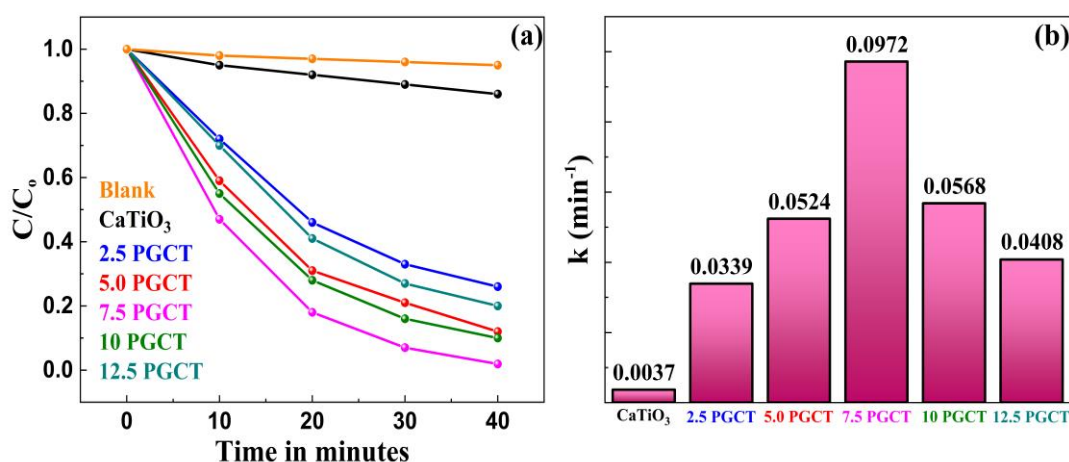


Figure 8.8 (a) Photocatalytic degradation curves and (b) rate constants for the photocatalytic degradation of MB by the synthesized $CaTiO_3$ and PGCT.

To derive the kinetic information, the above photocatalytic degradation results were better fitted with a pseudo-first-order rate equation 2.3. Apparently, the rate constant of 7.5 PGCT was found to be 0.0972 min^{-1} , which is far higher than that of pristine (0.0037 min^{-1}) (Figure 8.8 b). The slight deterioration in the photocatalytic activity of 7.5 PGCT after seven successive cycles pointing its high stability (Figure 8.9).

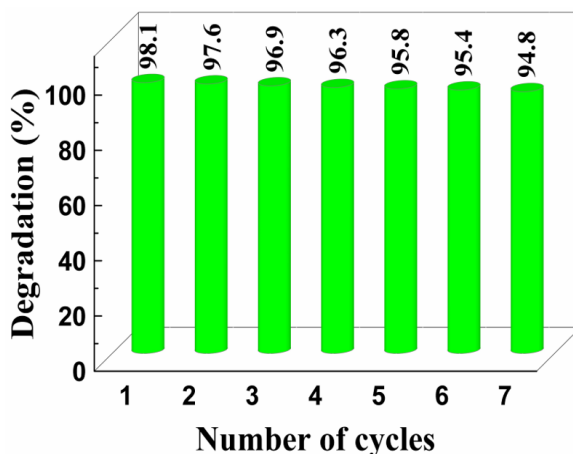


Figure 8.9 Cyclic stability of the synthesized 7.5 PGCT.

Further, the radical scavenging experiments indicated holes and hydroxyl radicals were the main reactive species as the addition of corresponding scavenging agents efficiently suppressed the photocatalytic rate, whereas superoxide anion radicals are the minor reactive species for the photocatalytic degradation of MB (Figure 8.10).

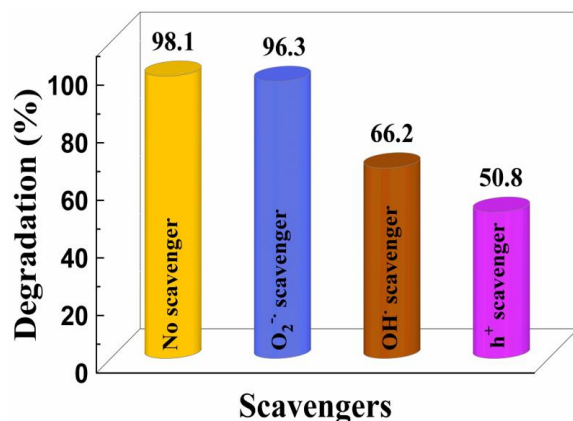


Figure 8.10 Effect of radical and hole scavengers on the photocatalytic degradation of MB by 7.5 PGCT.

Under visible light irradiation, an electron from the VB gets excited to the CB of $CaTiO_3$ resulting in the formation of a hole in the VB. The electrons from the CB of $CaTiO_3$ transfer to the PG sheets through the Ti-O-C bonds owing to the excellent electronic conductivity of PG thereby lengthening the lifetime of photoinduced charge carriers and enhancing the photocatalytic activity (Figure 8.11). These electrons react with oxygen to produce superoxide anion radicals and the holes either directly oxidize

MB or react with surface hydroxyl groups to produce hydroxyl radicals. These radicals react with MB dye molecules to produce CO₂ and H₂O.

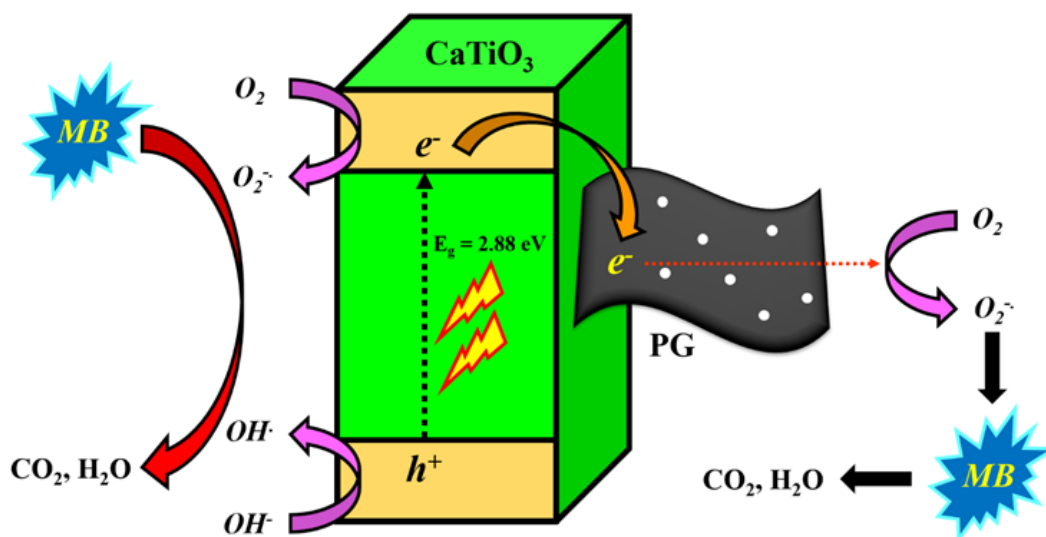


Figure 8.11 Mechanism of photocatalytic degradation of MB by PGCT.

The thermodynamic parameters such as, activation energy (E_a), the free energy of activation (ΔG^\ddagger), enthalpy of activation (ΔH^\ddagger), and entropy of activation (ΔS^\ddagger) were computed as described in Chapter 2. From Table 8.2, it can be seen that the E_a is higher for the photocatalytic degradation of MB without catalyst, whereas the energy of activation decreased in the presence of CaTiO₃ and PGCT samples. This confirms that the catalyst provides an alternate path for the reaction with lower activation energy. 7.5 PGCT sample exhibited the lowest activation energy as compared to other samples. The endothermic and non-spontaneous nature of the reaction was confirmed by the positive enthalpy change (ΔH^\ddagger) and free energy change (ΔG^\ddagger) values.

Table 8.2 Thermodynamic parameters of CaTiO₃ and PGCT samples

Sample	E _a (kJ/mol)	ΔH [#] (kJ/mol)	ΔS [#] (kJ/mol)	ΔG [#] (kJ/mol)
CaTiO ₃	13.97	11.47	-0.25	87.44
2.5 PGCT	8.44	5.94	-0.25	81.9
5.0 PGCT	7.35	4.86	-0.25	80.82
7.5 PGCT	5.81	3.32	-0.25	79.28
10 PGCT	7.15	4.66	-0.25	80.62
12.5 PGCT	7.98	5.48	-0.25	81.44
Without catalyst	16.6	14.1	-0.25	90.0

CHAPTER 9

SUMMARY AND CONCLUSIONS

Chapter 9 outlines the summary of the work presented in the thesis along with the important conclusions drawn from the study. Also, the scope for further research has been included.

9.1 SUMMARY

The thesis reports the successful synthesis of seven different series of photocatalysts using the solvothermal or hydrothermal approach. All the synthesized materials were thoroughly characterized for their elemental composition, structural, morphological, and optical properties with the help of various characterization techniques such as XRD, FESEM, TEM, HRTEM, Raman spectroscopy, XPS, BET method, DRS, and PL spectroscopy. Thereafter, the photocatalytic efficiencies of the synthesized materials were evaluated by taking MB as a target pollutant under visible light.

A summary of the overall work presented in the thesis is outlined in the following section.

Chapter 1 gives a brief introduction to the basic concepts of the study carried out. It also gives a brief outline of the relevant works in the literature which focus on graphene, perovskite titanate, metal-doped perovskite titanate, graphene-based composites, their synthetic methods, and photocatalytic applications along with the scope and objectives of the present research work.

Chapter 2 deals with the solvothermal synthesis of Rh-doped SrTiO₃ for photocatalytic application. The characterization results indicated the successful incorporation of Rh³⁺ into the Sr site with the reduction in band gap due to the formation of donor levels as well as the reduction in the rate of recombination of photoinduced charges. The 1.0 Rh sample was found to be highly active for the photocatalytic degradation of MB dye (72.9 % in 120 minutes). The 1.0 Rh exhibited sufficient photocatalytic stability even after 4 cycles for practical applications.

Chapter 3 deals with the solvothermal synthesis of V-doped SrTiO₃ for photocatalytic application. The characterization results indicated the successful doping of V⁴⁺ into Ti sites of SrTiO₃ and reduction in the band gap due to the formation of dopant levels just beneath the CB extending its absorption to the visible

region of the electromagnetic spectrum. The isovalent doping prevented the formation of recombination centers along with the increased surface area of the nanocubes. The high photocatalytic activity for MB degradation (83 % in 120 minutes) and stability of V-doped SrTiO₃ (1.0 V) even after 5 cycles indicated the suitability of the material for environmental remediation applications.

Chapter 4 deals with the solvothermal synthesis of PGST nanocomposite for photocatalytic application. The characterization results indicated the loofah-like structures which increased the surface area facilitating a higher rate of adsorption of MB dye. DRS analysis indicated a reduction in the band gap of SrTiO₃ on integration with PG due to the formation of C states within the band gap of SrTiO₃, extending the absorption to the visible region of the solar spectrum. The increased rate of charge transfer due to the formation of the Sr-C bond enhanced the charge separation and reduced the recombination rate. The composite (7.5 PGST) exhibited enhanced photocatalytic activity (~92 % in 120 minutes) and cyclic stability even after 5 cycles. The high performance of the PGST was attributed to the tuned electronic structure, morphology, and chemical bonding, which makes it a potential candidate for photocatalytic environmental remediation.

Chapter 5 deals with the hydrothermal synthesis of Rh-doped BaTiO₃ for photocatalytic application. The results indicated the successful incorporation of Rh³⁺ into the Ba site with the suppression in band gap due to the formation of donor levels as well as the reduction in the rate of recombination of photogenerated charge carriers. The 0.5 Rh sample was found to be highly active for the photocatalytic degradation of MB dye (96 % in 120 minutes). The 0.5 Rh exhibited sufficient photocatalytic stability even after 5 cycles for water treatment applications.

Chapter 6 deals with the solvothermal synthesis of PGBT nanocomposite for photocatalytic application. The composite (7.5 PGBT) exhibited excellent photocatalytic activity (98.6 % in 80 minutes) and cyclic stability even after seven consecutive cycles. The outstanding performance of the PGBT composite was attributed to the intimate contact between BaTiO₃ and PG through the Ba-C bond and high surface area. DRS analysis indicated a decrease in the band gap which extends

the absorption to the visible region enhancing the photocatalytic performance. The formation of the Ba-C bond was found to be highly advantageous for the efficient transport of photogenerated charge carriers, thereby suppressing the recombination of charge carriers.

Chapter 7 deals with the solvothermal synthesis of V-doped CaTiO_3 for photocatalytic application. The present synthetic strategy incorporated V^{4+} ions into Ti sites of CaTiO_3 with high surface area as confirmed by XRD, XPS, and BET results. DRS analysis showed that the band gap of the doped samples decreased due to the formation of additional energy levels just beneath the CB. The PL results indicated the efficient charge separation due to the isovalent doping. The superior photocatalytic activity (94.2 % in 120 minutes) and high stability of V-doped CaTiO_3 (1.0 V) even after seven consecutive cycles for MB degradation indicated that the material can be a promising catalyst for photocatalytic water treatment.

Chapter 8 deals with the solvothermal synthesis of PGCT nanocomposite for photocatalytic application. The composite (7.5 PGCT) showed excellent photocatalytic efficiency (98.1 % in 40 minutes) for the degradation of MB dye solution under visible light and excellent cyclic stability (7 cycles). The enhanced activity of the PGCT composite was attributed to the strong binding between CaTiO_3 and PG via the Ti-O-C bond, large surface area, efficient visible light-harvesting capacity, and suppressed charge recombination.

Chapter 9 deals with the summary of the work presented in the thesis along with important conclusions drawn from the study. The results of the research work presented in the thesis are also compared with the reported literature. The scope for further research has also been included in this chapter.

9.2 CONCLUSIONS

The overall conclusions drawn from the present research work are listed below:

- Metal ion-doped perovskite alkaline earth titanates can be prepared by a simple solvothermal/hydrothermal approach.

- Graphene-perovskite alkaline earth titanate-based nanocomposites can be prepared by a simple solvothermal approach.
- The synthesized materials can be used as efficient catalysts for the photodegradation of dyes.
- The synthesized materials exhibited enhanced photocatalytic activity due to enhanced visible light absorption and reduced charge recombination.
- The synthesized materials are highly stable and reusable.

The summarized results of the present research work are given in Table 9.1.

Further, the results obtained in this work have also been compared with reported literature (Table 9.2).

Table 9.1 Summarized results of present work

Catalysts	Rh-doped SrTiO₃	Rh-doped BaTiO₃	V-doped SrTiO₃	V-doped CaTiO₃	PGST composite	PGBT composite	PGCT composite
Photocatalytic activity towards MB under visible light irradiation							
MB: 100 mL (10 mg/L), Catalyst: 50 mg, Visible light source: High-pressure 250 W Hg vapor lamp (410-700 nm)							
Efficiency and time required	72.9 %, 120 min	96 %, 120 min	83 %, 120 min	94.2 %, 120 min	91.9 %, 120 min	98.6 %, 80 min	98.1 %, 40 min
Reusability	4 cycles (72.9 % to 71.1 %)	5 cycles (96.0 % to 92.6 %)	5 cycles (83.0 % to 80.2 %)	7 cycles (94.2 % to 91.3 %)	5 cycles (91.9 % to 90.1 %)	7 cycles (98.6 % to 95.6 %)	7 cycles (98.1 % to 94.8 %)

Table 9.2 Comparison of the photocatalytic degradation process parameters of reported catalysts

Photocatalysts	Light source	Degradation extent and time	Reference
Porous carbon quantum dots – SrTiO ₃ /graphene	Visible light source (250 W metal halide lamp)	MB 94 %, 210 min	Cui et al. 2022
Eu(III) doped SrTiO ₃	Visible (using a halogen lamp) light irradiation	MB 90-95 %, 600 min	Jang et al. 2021
RGO/SrTiO ₃ nanocomposite	UV-Visible irradiation (500 W halogen lamp)	MB 91 %, 150 min	Venkatesh et al. 2021
Bi-doped SrTiO ₃	Natural sunlight	MB 100 %, 150 min	Garcia et al. 2021
Carbon doped SrTiO ₃	Xenon lamp (500 W)	MB 95 %, 180 min	Chang and Hu 2020
BaTiO ₃ /ZnO heterostructure	UV light source (250 W)	MB 93.6 %, 60 min	Kappadan et al. 2020
Na ⁺ co-doped CaTiO ₃ :Eu ³⁺ powder	UV light source (35 W Hg lamp with a wavelength of 253.7 nm)	MB 96.62 %, 300 min	Chen et al. 2020

BaTiO ₃ @graphene oxide composite	UV-visible light source (Xe lamp)	MB 95 %, 180 min	Mengting et al. 2019
SrTiO ₃ /g-C ₃ N ₄ composite	Visible light irradiation using LED flood lamps	MB 0.0071 min ⁻¹	Konstas et al. 2018
SrTiO ₃ -TiN nanocomposite	Solar simulator (300 W Xe lamp)	MB 72 %, 150 min	Kang et al. 2018
Nitrogen-doped CaTiO ₃ coupled with RGO	Visible light source	MB 95 %, 180 min	Kumar et al. 2017
Rh-doped SrTiO ₃	Visible light source	MB 72.9 %, 120 min	Present work
Rh-doped BaTiO ₃	Visible light source	MB 96 %, 120 min	Present work
V-doped SrTiO ₃	Visible light source	MB 83 %, 120 min	Present work
V-doped CaTiO ₃	Visible light source	MB 94.2 %, 120 min	Present work
PGST composite	Visible light source	MB 91.9 %, 120 min	Present work

PGBT composite	Visible light source	MB 98.6 %, 80 min	Present work
PGCT composite	Visible light source	MB 98.1 %, 40 min	Present work

9.3 SCOPE FOR FUTURE WORK

As a continuation of the investigations carried out in the present thesis, there is scope for further studies. The following section highlights future research work.

- In this thesis, MB was chosen as a model pollutant to study the photocatalytic activities of the prepared catalysts. This paves the way for the study of photocatalytic activity by taking other dyes.
- The various intermediates involved in photodegradation can be studied with the help of techniques like HPLC and LC/MS.
- V-doped BaTiO₃ can be synthesized by a high-temperature solid-state reaction method and its photocatalytic activity can be evaluated.
- Rh-doped CaTiO₃ can be synthesized by a high-temperature solid-state reaction method and its photocatalytic activity can be evaluated.
- The synthesized materials can be used to study photocatalytic water splitting.

REFERENCES

Abdi, M., Mahdikhah, V. and Sheibani, S. (2020). "Visible light photocatalytic performance of La-Fe co-doped SrTiO₃ perovskite powder." *Opt. Mater.*, 102, 109803.

Ahmadi, M., Seyed Dorraji, M. S., Rasoulifard, M. H. and Amani-Ghadim, A. R. (2019). "The effective role of reduced-graphene oxide in visible light photocatalytic activity of wide band gap SrTiO₃ semiconductor." *Sep. Purif. Technol.*, 228, 115771.

Alamelu, K. and Jaffar Ali, B. M. (2020). "Ag nanoparticle-impregnated sulfonated graphene/TiO₂ composite for the photocatalytic removal of organic pollutants." *Appl. Surf. Sci.*, 512, 145629.

Ali, A., Liang, Y., Ahmed, S., Yang, B., Guo, B. and Yang, Y. (2020). "Mutual contaminants relational realization and photocatalytic treatment using Cu₂MgSnS₄ decorated BaTiO₃." *Appl. Mater. Today*, 18, 100534.

Alkhouzaam, A., Qiblawey, H., Khraisheh, M., Atieh, M. and Al-Ghouti, M. (2020). "Synthesis of graphene oxides particle of high oxidation degree using a modified Hummers method." *Ceram. Int.*, 46 (15), 23997–24007.

Amaechi, I. C., Hadj Youssef, A., Kolhatkar, G., Rawach, D., Gomez-Yañez, C., Claverie, J. P., Sun, S. and Ruediger, A. (2021). "Ultrafast microwave-assisted hydrothermal synthesis and photocatalytic behaviour of ferroelectric Fe³⁺-doped BaTiO₃ nanoparticles under simulated sunlight." *Catal. Today*, 360, 90–98.

Amaechi, I. C., Hadj Youssef, A., Rawach, D., Claverie, J. P., Sun, S. and Ruediger, A. (2019). "Ferroelectric Fe–Cr codoped BaTiO₃ nanoparticles for the photocatalytic oxidation of azo dyes." *ACS Appl. Nano Mater.*, 2(5), 2890–2901.

Amaechi, I. C., Kolhatkar, G., Youssef, A. H., Rawach, D., Sun, S. and Ruediger, A. (2019). "B-site modified photoferroic Cr³⁺-doped barium titanate nanoparticles: Microwave-assisted hydrothermal synthesis, photocatalytic and electrochemical properties." *RSC Adv.*, 9(36), 20806–20817.

Amaechi, I. C., Youssef, A. H., Kolhatkar, G., Rawach, D., Gomez-Yañez, C., Claverie, J.P., Sun, S. and Ruediger, A. (2021). "Ultrafast microwave-assisted hydrothermal synthesis and photocatalytic behaviour of ferroelectric Fe³⁺-doped BaTiO₃ nanoparticles under simulated sunlight." *Catal. Today*, 360, 90-98.

Bae, H. S., Manikandan, V., Hwang, J. H., Seo, Y. S., Chung, H. S., Ryu, H. I., Chae, W. S., Cho, M., Ekambe, P. S. and Jang, J. S. (2021). "Photocatalytic degradation of organic pollutants and inactivation of pathogens under visible light via CoO_x surface-modified Rh/Sb-doped SrTiO₃ nanocube." *J. Mater. Sci.*, 56, 17235-17253.

Bantawal, H., Sethi, M., Shenoy, U. S. and Bhat, D. K. (2019). "Porous graphene wrapped SrTiO₃ nanocomposite: Sr–C bond as an effective coadjutant for high performance photocatalytic degradation of methylene blue." *ACS Appl. Nano Mater.*, 2(10), 6629–6636.

Bantawal, H., Shenoy, U. S. and Bhat, D. K. (2020). "Vanadium-doped SrTiO₃ nanocubes: Insight into role of vanadium in improving the photocatalytic activity." *Appl. Surf. Sci.*, 513, 145858.

Bhat, D. K., Bantawal, H. and Shenoy, U. S. (2020). "Rhodium doping augments photocatalytic activity of barium titanate: Effect of electronic structure engineering." *Nanoscale Adv.*, 2(12), 5688–5698.

Bhat, D. K. and Shenoy, U. S. (2019). "Zn: A versatile resonant dopant for SnTe thermoelectrics." *Mater. Today Phys.*, 11, 100158.

Bilal Taşyürek, L., Sevim, M., Çaldıran, Z., Aydoğan, S. and Metin, Ö. (2018). "The synthesis of SrTiO₃ nanocubes and the analysis of nearly ideal diode application of Ni/SrTiO₃ nanocubes/n-Si heterojunctions." *Mater. Res. Express*, 5, 015060.

Boukhalov, D. W., Zhidkov, I. S., Kukharensko, A. I., Cholakh, S. O., Menéndez, J. L., Fernández-García, L. and Kurmaev, E. Z. (2020). "Interaction of graphene oxide with barium titanate in composite: XPS and DFT studies." *J. Alloys Compd.*, 840, 155747.

Cai, J., Cao, A., Huang, J., Jin, W., Zhang, J., Jiang, Z. and Li, X. (2020). "Understanding oxygen vacancies in disorder-engineered surface and subsurface of CaTiO₃ nanosheets on photocatalytic hydrogen evolution." *Appl. Catal. B*, 267, 118378.

Cao, J., Ji, Y., Tian, C. and Yi, Z. (2014). "Synthesis and enhancement of visible light activities of nitrogen-doped BaTiO₃." *J. Alloys Compd.*, 615, 243–248.

Chang, C. W. and Hu, C. (2020). "Graphene oxide-derived carbon-doped SrTiO₃ for highly efficient photocatalytic degradation of organic pollutants under visible light irradiation." *Chem. Eng. J.*, 383, 123116.

Chao, C., Zhou, Y., Han, T., Yang, Y., Wei, J., Li, H. and He, W. (2020). "Ferroelectric polarization-enhanced photocatalytic properties and photo-induced charge carrier behavior of Au/BaTiO₃." *J. Alloys and Compd.*, 825, 154060.

Chen, H. C., Huang, C. W., Wu, J. C. S. and Lin, S. T. (2012). "Theoretical investigation of the metal-doped SrTiO₃ photocatalysts for water splitting." *J. Phys. Chem. C*, 116 (14), 7897–7903.

Chen, M., Xiong, Q., Liu, Z., Qiu, K. and Xiao, X. (2020). "Synthesis and photocatalytic activity of Na⁺ co-doped CaTiO₃:Eu³⁺ photocatalysts for methylene blue degradation." *Ceram. Int.*, 46 (8, Part B), 12111–12119.

Chen, X., He, X., Yang, X., Wu, Z. and Li, Y. (2020). "Construction of novel 2D/1D g-C₃N₄/CaTiO₃ heterojunction with face-to-face contact for boosting photodegradation of triphenylmethane dyes under simulated sunlight." *J. Taiwan Inst. Chem. Eng.*, 107 98–109.

Coros, M., Pogacean, F., Turza, A., Dan, M., Berghian-Grosan, C., Pana, I. O. and Pruneanu, S. (2020). "Green synthesis, characterization and potential application of reduced graphene oxide." *Phys. E: Low-Dimens. Syst. Nanostructures*, 119 113971.

Cui, J., Liu, J., Xia, X., Chai, X., Guo, H., Gao, J. and Gao, S. (2022). "Carbonized propagation synthesis of porous CQDs-SrTiO₃/graphene and its photocatalytic

performance for removal of methylene blue.” *Environ. Sci. Water Res. Technol.*, 8, 671-685.

Demircivi, P. and Simsek, E. B. (2019). “Visible-light-enhanced photoactivity of perovskite-type W-doped BaTiO₃ photocatalyst for photodegradation of tetracycline.” *J. Alloys Compd.*, 774, 795–802.

Demircivi, P., Gulen, B., Simsek, E. B. and Berek, D. (2020). “Enhanced photocatalytic degradation of tetracycline using hydrothermally synthesized carbon fiber decorated BaTiO₃.” *Mater. Chem. Phys.*, 241, 122236.

Deng, T., Zhang, Z., Liu, Y., Wang, Y., Su, F., Li, S., Zhang, Y., Li, H., Chen, H., Zhao, Z., Li, Y. and Liu, Z. (2019). "Three-dimensional graphene field-effect transistors as high-performance photodetectors." *Nano Lett.*, 19 (3), 1494–1503.

Di Valentin, C. and Pacchioni, G. (2013). "Trends in non-metal doping of anatase TiO₂: B, C, N and F." *Catal. Today*, 206 12–18.

Dong, L., Shi, H., Cheng, K., Wang, Q., Weng, W. and Han, W. (2014). "Shape-controlled growth of SrTiO₃ polyhedral submicro/nanocrystals." *Nano Res.*, 7 (9), 1311–1318.

Dong, S., Feng, J., Fan, M., Pi, Y., Hu, L., Han, X., Liu, M., Sun, J. and Sun, J. (2015). "Recent developments in heterogeneous photocatalytic water treatment using visible light-responsive photocatalysts: a review." *RSC Adv.*, 5 (19), 14610–14630.

Fujishima, A. and Honda, K. (1972). "Electrochemical photolysis of water at a semiconductor electrode." *Nature*, 238 (5358), 37–38.

Furuhashi, K., Jia, Q., Kudo, A. and Onishi, H. (2013). "Time-resolved infrared absorption study of SrTiO₃ photocatalysts codoped with rhodium and antimony." *J. Phys. Chem. C*, 117 (37), 19101–19106.

Garcia, C. R., Oliva, J., Chávez, D., Esquivel, B., Gómez-Solís, C., Martínez-Sánchez, E. and Mtz-Enriquez, A.I. (2021). “Effect of bismuth dopant on the photocatalytic properties of SrTiO₃ under solar irradiation.” *Top. Catal.*, 64, 155-166.

Glaze, W. H., Kang, J. W. and Chapin, D. H. (1987). "The chemistry of water treatment processes involving ozone, hydrogen peroxide and ultraviolet radiation." *Ozone Sci. Eng.*, 9 (4), 335–352.

Govindasamy, M., Wang, S. F., Pan, W. C., Subramanian, B., Ramalingam, R. J. and Al-lohedan, H. (2019). "Facile sonochemical synthesis of perovskite-type SrTiO₃ nanocubes with reduced graphene oxide nanocatalyst for an enhanced electrochemical detection of α -amino acid (tryptophan)." *Ultrason. Sonochem.*, 56, 193–199.

He, C., Bu, X., Yang, S., He, P., Ding, G. and Xie, X. (2018). "Core-shell SrTiO₃/graphene structure by chemical vapor deposition for enhanced photocatalytic performance." *Appl. Surf. Sci.*, 436, 373–381.

Hoang, V. Q. T., Phan, T. Q. P., Senthilkumar, V., Doan, V. T., Kim, Y. S. and Le, M. V. (2019). "Enhanced photocatalytic activities of vanadium and molybdenum co-doped strontium titanate under visible light." *Int. J. Appl. Ceram. Technol.*, 16 (4), 1651–1658.

Huang, H. C., Yang, C. L., Wang, M. S. and Ma, X. G. (2019). "Chalcogens doped BaTiO₃ for visible light photocatalytic hydrogen production from water splitting." *Spectrochim. Acta A Mol. Biomol. Spectrosc.*, 208, 65–72.

Huang, X., Yan, X., Wu, H., Fang, Y., Min, Y., Li, W., Wang, S. and Wu, Z. (2016). "Preparation of Zr-doped CaTiO₃ with enhanced charge separation efficiency and photocatalytic activity." *Trans. Nonferrous Met. Soc. China*, 26(2), 464–471.

Hummers, W.S. and Offeman, R.E. (1958). "Preparation of graphitic oxide." *J. Am. Chem. Soc.*, 80 (6), 1339–1339.

Huo, Q., Jin, J., Wang, X., Lu, S., Zhang, Y., Ma, J. and Wang, S. (2019). "Preparation of graphene-based sensor and its application in human behavior monitoring." *Mater. Res. Express*, 6 (7), 075613.

Hussain, T., Junaid, M. and Qayyum, H.A. (2020). "Preparation of Ba-doped SrTiO₃ photocatalyst by sol-gel method for hydrogen generation." *Chem. Phys. Lett.*, 754 137741.

Irie, H., Maruyama, Y. and Hashimoto, K. (2007). "Ag⁺ and Pb²⁺ doped SrTiO₃ photocatalysts. A correlation between band structure and photocatalytic activity." *J. Phys. Chem. C*, 111 (4), 1847–1852.

Iwashina, K. and Kudo, A. (2011). "Rh-doped SrTiO₃ photocatalyst electrode showing cathodic photocurrent for water splitting under visible-light irradiation." *J. Am. Chem. Soc.*, 133 (34), 13272–13275.

Jaihindh, D. P., Verma, A., Chen, C. C., Huang, Y. C., Dong, C. L. and Fu, Y. P. (2019). "Study of oxidation states of Fe- and Co-doped TiO₂ photocatalytic energy materials and their visible-light-driven photocatalytic behavior." *Int. J. Hydrog. Energy*, 44 (30), 15892–15906.

Jang, H. J., Park, S. J., Yang, J. H., Hong, S. M., Rhee, C. K., Kim, D. and Sohn, Y. (2021). "Photocatalytic and photoelectrocatalytic properties of Eu (III)-doped perovskite SrTiO₃ nanoparticles with dopant level approaches." *Mater. Sci. Semicond. Process.*, 132, 105919.

Jiang, E., Song, N., Che, G., Liu, C., Dong, H. and Yang, L. (2020). "Construction of a Z-scheme MoS₂/CaTiO₃ heterostructure by the morphology-controlled strategy towards enhancing photocatalytic activity." *Chem. Eng. J.*, 399, 125721.

Jiang, X., Yin, D., Yang, M., Du, J., Wang, W., Zhang, L., Yang, L., Han, X. and Zhao, B. (2019). "Revealing interfacial charge transfer in TiO₂/reduced graphene oxide nanocomposite by surface-enhanced Raman scattering (SERS): Simultaneous a superior SERS-active substrate." *Appl. Surf. Sci.*, 487, 938–944.

Jiao, Z., Chen, T., Xiong, J., Wang, T., Lu, G., Ye, J. and Bi, Y. (2013). "Visible-light-driven photoelectrochemical and photocatalytic performances of Cr-doped SrTiO₃/TiO₂ heterostructured nanotube arrays." *Sci. Rep.*, 3 (1), 2720.

Jongprateep, O., Sato, N., Techapiesancharoenkij, R. and Surawathanawises, K. (2019). "Electrocatalytic properties of calcium titanate, strontium titanate, and strontium calcium titanate powders synthesized by solution combustion technique." *Adv. Mater. Sci. Eng.*, 2019, 1612456.

Kampouri, S. and Stylianou, K.C. (2019). "Dual-functional photocatalysis for simultaneous hydrogen production and oxidation of organic substances." *ACS Catal.*, 9 (5), 4247–4270.

Kang, C., Xiao, K., Wang, Y., Huang, D., Zhu, L., Liu, F. and Tian, T. (2018). "Synthesis of SrTiO₃-TiN nanocomposites with enhanced photocatalytic activity under simulated solar irradiation." *Ind. Eng. Chem. Res.*, 57(34), 11526-11534.

Kanhere, P. and Chen, Z. (2014). "A review on visible light active perovskite-based photocatalysts." *Molecules*, 19 (12), 19995–20022.

Kappadan, S., Thomas, S. and Kalarikkal, N. (2020). "BaTiO₃/ZnO heterostructured photocatalyst with improved efficiency in dye degradation." *Mater. Chem. Phys.*, 255, 123583.

Kawasaki, S., Akagi, K., Nakatsuji, K., Yamamoto, S., Matsuda, I., Harada, Y., Yoshinobu, J., Komori, F., Takahashi, R., Lippmaa, M., Sakai, C., Niwa, H., Oshima, M., Iwashina, K. and Kudo, A. (2012). "Elucidation of Rh-induced in-gap states of Rh:SrTiO₃ visible-light-driven photocatalyst by soft X-ray spectroscopy and first-principles calculations." *J. Phys. Chem. C*, 116 (46), 24445–24448.

Kawasaki, S., Takahashi, R., Akagi, K., Yoshinobu, J., Komori, F., Horiba, K., Kumigashira, H., Iwashina, K., Kudo, A. and Lippmaa, M. (2014). "Electronic structure and photoelectrochemical properties of an Ir-doped SrTiO₃ photocatalyst." *J. Phys. Chem. C*, 118 (35), 20222–20228.

Kiss, B., Manning, T. D., Hesp, D., Didier, C., Taylor, A., Pickup, D. M., Chadwick, A. V., Allison, H. E., Dhanak, V. R., Claridge, J. B., Darwent, J. R. and Rosseinsky, M. J. (2017). "Nano-structured rhodium doped SrTiO₃-visible light-activated photocatalyst for water decontamination." *Appl. Catal. B*, 206, 547–555.

Konstas, P. S., Konstantinou, I., Petrakis, D. and Albanis, T. (2018). "Synthesis, characterization of g-C₃N₄/SrTiO₃ heterojunctions and photocatalytic activity for organic pollutants degradation." *Catalysts*, 8(11), 554.

Kshirsagar, A. S. and Khanna, P. K. (2019). "CuSbSe₂/TiO₂: Novel type-II heterojunction nano-photocatalyst." *Mater. Chem. Front.*, 3 (3), 437–449.

Kumar, A., Kumar, A. and Krishnan, V. (2020). "Perovskite oxide based materials for energy and environment-oriented photocatalysis." *ACS Catal.*, 10 (17), 10253–10315.

Kumar, A., Kumar, S., Bahuguna, A., Kumar, A., Sharma, V. and Krishnan, V. (2017). "Recyclable, bifunctional composites of perovskite type N-CaTiO₃ and reduced graphene oxide as an efficient adsorptive photocatalyst for environmental remediation." *Mater. Chem. Front.*, 1 (11), 2391–2404.

Kusiak-Nejman, E. and Morawski, A. W. (2019). "TiO₂/graphene-based nanocomposites for water treatment: A brief overview of charge carrier transfer, antimicrobial and photocatalytic performance." *Appl. Catal. B*, 253 179–186.

Lee, S. M., Park, Y. J., Lam, D. V., Kim, J. H. and Lee, K. (2020). "Effects of annealing on electrochemical performance in graphene/V₂O₅ supercapacitor." *Appl. Surf. Sci.*, 512, 145626.

Lee, X. J., Hiew, B. Y. Z., Lai, K. C., Lee, L. Y., Gan, S., Thangalazhy-Gopakumar, S. and Rigby, S. (2019). "Review on graphene and its derivatives: Synthesis methods and potential industrial implementation." *J. Taiwan Inst. Chem. Eng.*, 98, 163–180.

Li, J., Xu, J. and Huang, J. (2013). "Nanofibrous vanadium-doped rutile titania derived from cellulose substance by flame synthesis." *CrystEngComm*, 16 (3), 375–384.

Li, J., Yu, X., Zhu, Y., Fu, X. and Zhang, Y. (2021). "3D-2D-3D BiOI/porous g-C₃N₄/graphene hydrogel composite photocatalyst with synergy of adsorption-photocatalysis in static and flow systems." *J. Alloys Compd.*, 850, 156778.

Li, Y., Gu, D., Xu, S., Zhou, X., Yuan, K. and Jiang, Y. (2020). "A monoclinic V_{1-x}

$y\text{Ti}_x\text{Ru}_y\text{O}_2$ thin film with enhanced thermal-sensitive performance.” *Nanoscale Res. Lett.*, 15(1), 92.

Li, Y., Zhu, S., Kong, X., Liang, Y., Li, Z., Wu, S., Chang, C., Luo, S. and Cui, Z. (2021). "In situ synthesis of a novel $\text{Mn}_3\text{O}_4/\text{g-C}_3\text{N}_4$ p-n heterostructure photocatalyst for water splitting." *J. Colloid Interface Sci.*, 586, 778–784.

Liu, B., Wang, X., Cai, G., Wen, L., Song, Y. and Zhao, X. (2009). “Low temperature fabrication of V-doped TiO_2 nanoparticles, structure and photocatalytic studies.” *J. Hazard. Mater.*, 169(1–3), 1112–1118.

Liu, D., Jin, C., Shan, F., He, J. and Wang, F. (2020). “Synthesizing BaTiO_3 nanostructures to explore morphological influence, kinetics, and mechanism of piezocatalytic dye degradation.” *ACS Appl. Mater. Interfaces*, 12(15), 17443–17451.

Liu, X., Ji, H., Li, S. and Liu, W. (2019). “Graphene modified anatase/titanate nanosheets with enhanced photocatalytic activity for efficient degradation of sulfamethazine under simulated solar light.” *Chemosphere*, 233, 198–206.

Liu, X., Xiao, L., Zhang, Y. and Sun, H. (2020). “Significantly enhanced piezocatalytic capability in BaTiO_3 nanowires for degrading organic dye.” *J. Materiomics*, 6(2), 256–262.

Lozano-Sánchez, L. M., Obregón, S., Díaz-Torres, L. A., Lee, S. W. and Rodríguez-González, V. (2015). “Visible and near-infrared light-driven photocatalytic activity of erbium-doped CaTiO_3 system.” *J. Mol. Catal.*, 410, 19–25.

LV, M., Xie, Y., Wang, Y., Sun, X., Wu, F., Chen, H., Wang, S., Shen, C., Chen, Z., Ni, S., Liu, G. and Xu, X. (2015). "Bismuth and chromium co-doped strontium titanates and their photocatalytic properties under visible light irradiation." *Phys. Chem. Chem. Phys.*, 17(39), 26320–26329.

Ma, J., Yamamoto, Y., Su, C., Badhulika, S., Fukuhara, C. and Kong, C. Y. (2021). "One-pot microwave-assisted synthesis of porous reduced graphene oxide as an

electrode material for high capacitance supercapacitor." *Electrochim. Acta*, 386, 138439.

Macías, J., Yaremchenko, A. A., Rodríguez-Castellón, E., Sarykevich, M. and Frade, J. R. (2019). "Compromising between phase stability and electrical performance: SrVO₃-SrTiO₃ solid solutions as solid oxide fuel cell anode components." *ChemSusChem*, 12(1), 240–251.

Maeda, K. (2014). "Rhodium-doped barium titanate perovskite as a stable p-type semiconductor photocatalyst for hydrogen evolution under visible light." *ACS Appl. Mater. Interfaces*, 6(3), 2167–2173.

Mahalingam, S., Manap, A., Omar, A., Low, F. W., Afandi, N. F., Chia, C. H. and Rahim, N. A. (2021). "Functionalized graphene quantum dots for dye-sensitized solar cell: Key challenges, recent developments and future prospects." *Renew. Sustain. Energy Rev.*, 144, 110999.

Md Saad, S. K., Ali Umar, A., Ali Umar, M. I., Tomitori, M., Abd. Rahman, Mohd. Y., Mat Salleh, M. and Oyama, M. (2018). "Two-dimensional, hierarchical Ag-doped TiO₂ nanocatalysts: Effect of the metal oxidation state on the photocatalytic properties." *ACS Omega*, 3 (3), 2579–2587.

Mengting, Z., Kurniawan, T. A., Fei, S., Ouyang, T., Othman, M. H. D., Rezakazemi, M. and Shirazian, S. (2019). "Applicability of BaTiO₃/graphene oxide (GO) composite for enhanced photodegradation of methylene blue (MB) in synthetic wastewater under UV-vis irradiation." *Environ. Pollut.*, 255, 113182.

Mishra, N., Boeckl, J., Motta, N. and Iacopi, F. (2016). "Graphene growth on silicon carbide: A review." *Phys. Status Solidi A*, 213(9), 2277–2289.

Modak, B. and Ghosh, S. K. (2015). "Enhancement of visible light photocatalytic activity of SrTiO₃: A hybrid density functional study." *J. Phys. Chem. C*, 119(41), 23503–23514.

Modak, B. and Ghosh, S. K. (2015). "Exploring the role of La codoping beyond charge compensation for enhanced hydrogen evolution by Rh–SrTiO₃." *J. Phys. Chem. B*, 119(34), 11089–11098.

Modak, B. and Ghosh, S. K. (2015). "Role of F in improving the photocatalytic activity of Rh-doped SrTiO₃." *J. Phys. Chem. C*, 119(13), 7215–7224.

Modak, B. and Ghosh, S. K. (2018). "Insight into the enhanced photocatalytic activity of SrTiO₃ in the presence of a (Ni, V/Nb/Ta/Sb) pair." *Phys. Chem. Chem. Phys.*, 20(30), 20078–20087.

Mohamed, M. J. S., Shenoy U, S. and Bhat, D. K. (2018). "Novel NRGGO-CoWO₄-Fe₂O₃ nanocomposite as an efficient catalyst for dye degradation and reduction of 4-nitrophenol." *Mater. Chem. Phys.*, 208, 112–122.

Mohamed, M. J. S., Shenoy, U. S. and Bhat, D.K. (2017). "High performance dual catalytic activity of novel zinc tungstate-reduced graphene oxide nanocomposites." *Adv. Sci. Eng. Med.*, 9 (2), 115–121.

Muñoz, R. and Gómez-Aleixandre, C. (2013). "Review of CVD synthesis of graphene." *Chem. Vap. Depos.*, 19(10-11-12), 297–322.

Nageri, M. and Kumar, V. (2018). "Manganese-doped BaTiO₃ nanotube arrays for enhanced visible light photocatalytic applications." *Mater. Chem. Phys.*, 213, 400–405.

Nishikiori, H., Tagami, K., Matsunaga, S. and Teshima, K. (2019). "In situ probing of photoinduced hydrophilicity on titania surface using dye molecules." *ACS Omega*, 4(3), 5944–5949.

Nishioka, S. and Maeda, K. (2015). "Hydrothermal synthesis of rhodium-doped barium titanate nanocrystals for enhanced photocatalytic hydrogen evolution under visible light." *RSC Adv.*, 5(121), 100123–100128.

Novoselov, K. S., Geim, A. K., Morozov, S. V., Jiang, D., Zhang, Y., Dubonos, S. V., Grigorieva, I. V. and Firsov, A. A. (2004). "Electric field effect in atomically thin carbon films." *Science*, 306 (5696), 666–669.

Ong, W. J., Tan, L. L., Chai, S. P., Yong, S. T. and Mohamed, A. R. (2014). "Highly reactive {001} facets of TiO₂-based composites: Synthesis, formation mechanism and characterization." *Nanoscale*, 6(4), 1946–2008.

Ouyang, S., Tong, H., Umezawa, N., Cao, J., Li, P., Bi, Y., Zhang, Y. and Ye, J. (2012). "Surface-alkalinization-induced enhancement of photocatalytic H₂ evolution over SrTiO₃-based photocatalysts." *J. Am. Chem. Soc.*, 134(4), 1974–1977.

Park, B. G. (2019). "Photoluminescence of Eu³⁺-doped CaTiO₃ perovskites and their photocatalytic properties with a metal ion loading." *Chem. Phys. Lett.*, 722, 44–49.

Pei, S., Wei, Q., Huang, K., Cheng, H. M. and Ren, W. (2018). "Green synthesis of graphene oxide by seconds timescale water electrolytic oxidation." *Nat. Commun.*, 9(1), 145.

Pelaez, M., Nolan, N. T., Pillai, S. C., Seery, M. K., Falaras, P., Kontos, A. G., Dunlop, P. S. M., Hamilton, J. W. J., Byrne, J. A., O'Shea, K., Entezari, M. H. and Dionysiou, D. D. (2012). "A review on the visible light active titanium dioxide photocatalysts for environmental applications." *Appl. Catal. B*, 125, 331–349.

Phoon, B. L., Lai, C. W., Juan, J. C., Show, P. L. and Pan, G. T. (2019). "Recent developments of strontium titanate for photocatalytic water splitting application." *Int. J. Hydrog. Energy*, 44(28), 14316–14340.

Prinsen, P. and Luque, R. (2019). "Chapter 1. Introduction to Nanocatalysts." *Catalysis Series*, R. Luque and P. Prinsen, eds., Cambridge: Royal Society of Chemistry, 1–36.

Priyadharsini, C. I., Marimuthu, G., Pazhanivel, T., Anbarasan, P. M., Aroulmoji, V., Prabhu, S. and Ramesh, R. (2020). "Electrochemical supercapacitor studies of Ni²⁺-doped SrTiO₃ nanoparticles by a ball milling method." *Ionics*, 26(7), 3591–3597.

Qi, J., Li, Y., Zhang, X., Wang, J., Zhang, Q., Xue, Y., Cheng, J., Li, M., Han, X., Ma, Z. and Fang, D. (2020). "Solid-state synthesis semiconducting BaTiO₃ nanoparticles at low temperature." *Mater. Chem. Phys.*, 242, 122496.

Rayssi, C., El.Kossi, S., Dhahri, J. and Khirouni, K. (2018). "Frequency and temperature-dependence of dielectric permittivity and electric modulus studies of the solid solution Ca_{0.85}Er_{0.1}Ti_{1-x}Co_{4x/3}O₃ (0 ≤ x ≤ 0.1)." *RSC Adv.*, 8(31), 17139–17150.

Ren, D., Liang, Z., Ng, Y. H., Zhang, P., Xiang, Q. and Li, X. (2020). "Strongly coupled 2D-2D nanojunctions between P-doped Ni₂S (Ni₂SP) cocatalysts and CdS nanosheets for efficient photocatalytic H₂ evolution." *Chem. Eng. J.*, 390, 124496.

Ren, L., Yi, X., Tong, L., Zhou, W., Wang, D., Liu, L. and Ye, J. (2020). "Nitrogen-doped ultrathin graphene encapsulated Cu nanoparticles decorated on SrTiO₃ as an efficient water oxidation photocatalyst with activity comparable to BiVO₄ under visible-light irradiation." *Appl. Catal. B*, 279, 119352.

Sadiq Mohamed, M. J. and Bhat Denthaje, K. (2016). "Novel RGO-ZnWO₄-Fe₃O₄ nanocomposite as an efficient catalyst for rapid reduction of 4-nitrophenol to 4-aminophenol." *Ind. Eng. Chem. Res.*, 55(27), 7267–7272.

Sadiq, M. M. J., Shenoy, U. S. and Bhat, D. K. (2016). "Novel RGO-ZnWO₄-Fe₃O₄ nanocomposite as high performance visible light photocatalyst." *RSC Adv.*, 6(66), 61821–61829.

Sadiq, M. M. J., Shenoy, U. S. and Bhat, D. K. (2017). "Enhanced photocatalytic performance of N-doped RGO-FeWO₄/Fe₃O₄ ternary nanocomposite in environmental applications." *Mater. Today Chem.*, 4, 133–141.

Sadiq, M. M. J., Shenoy, U. S. and Bhat, D. K. (2018). "Synthesis of BaWO₄/NRGO-g-C₃N₄ nanocomposites with excellent multifunctional catalytic performance via microwave approach." *Front. Mater. Sci.*, 12(3), 247–263.

Sadiq, M. M. J., Shenoy, U. S. and Bhat, D. K. (2017). "NiWO₄-ZnO-NRGO ternary nanocomposite as an efficient photocatalyst for degradation of methylene blue and reduction of 4-nitro phenol." *J. Phys. Chem. Solids*, 109, 124–133.

Sattari-Esfahlan, S. M. and Kim, C. H. (2021). "Flexible graphene-channel memory devices: A review." *ACS Appl. Nano Mater.*, 4(7), 6542–6556.

Sekar, K., Kassam, A., Bai, Y., Coulson, B., Li, W., Douthwaite, R. E., Sasaki, K. and Lee, A. F. (2021). "Hierarchical bismuth vanadate/reduced graphene oxide composite photocatalyst for hydrogen evolution and bisphenol A degradation." *Appl. Mater. Today*, 22, 100963.

Senthilkumar, P., Jency, D. A., Kavinkumar, T., Dhayanithi, D., Dhanuskodi, S., Umadevi, M., Manivannan, S., Giridharan, N. V., Thiagarajan, V., Sriramkumar, M. and Jothivenkatachalam, K. (2019). "Built-in electric field assisted photocatalytic dye degradation and photoelectrochemical water splitting of ferroelectric Ce doped BaTiO₃ nanoassemblies." *ACS Sustain. Chem. Eng.*, 7(14), 12032-12043.

Sethi, M., Bantawal, H., Shenoy, U. S. and Bhat, D. K. (2019). "Eco-friendly synthesis of porous graphene and its utilization as high performance supercapacitor electrode material." *J. Alloys Compd.*, 799, 256–266.

Sethi, M., Shenoy, U. S. and Bhat, D. K. (2020). "A porous graphene-NiFe₂O₄ nanocomposite with high electrochemical performance and high cycling stability for energy storage applications." *Nanoscale Adv.*, 2(9), 4229–4241.

Sethi, M., Shenoy, U. S. and Bhat, D. K. (2020). "Porous graphene-NiCo₂O₄ nanorod hybrid composite as a high performance supercapacitor electrode material." *New J. Chem.*, 44(10), 4033–4041.

Sethi, M., Shenoy, U. S. and Bhat, D. K. (2020). "A porous graphene-NiFe₂O₄ nanocomposite with high electrochemical performance and high cycling stability for energy storage applications." *Nanoscale Adv.*, 2(9), 4229–4241.

Sethi, M., Shenoy, U. S. and Bhat, D. K. (2021). "Simple solvothermal synthesis of porous graphene-NiO nanocomposites with high cyclic stability for supercapacitor application." *J. Alloys Compd.*, 854, 157190.

Shenoy, S. and Bhat, D. K. (2017). "Enhanced bulk thermoelectric performance of $\text{Pb}_{0.6}\text{Sn}_{0.4}\text{Te}$: Effect of magnesium doping." *J. Phys. Chem. C*, 121(38), 20696–20703.

Shenoy, U. S. and Bhat, D. K. (2020). "Enhanced thermoelectric properties of vanadium doped SrTiO_3 : A resonant dopant approach." *J. Alloys Compd.*, 832, 154958.

Shenoy, U. S., Bantawal, H. and Bhat, D. K. (2018). "Band engineering of SrTiO_3 : Effect of synthetic technique and site occupancy of doped rhodium." *J. Phys. Chem. C*, 122(48), 27567-27574.

Shi, L., Zhang, Z., Wang, R., Zhou, C. and Sun, C. (2020). "Synthesis and post-annealing of Ag nanoparticles decorated urchin-like SrTiO_3 particles for enhanced electron/hole separation and photocatalytic activity." *Ceram. Int.*, 46(11), 19460-19468.

Shi, M., Rhimi, B., Zhang, K., Xu, J., Bahnemann, D. W. and Wang, C. (2021). "Visible light-driven novel $\text{Bi}_2\text{Ti}_2\text{O}_7/\text{CaTiO}_3$ composite photocatalyst with enhanced photocatalytic activity towards NO removal." *Chemosphere*, 275, 130083.

Shi, X., Yang, H., Liang, Z., Tian, A. and Xue, X. (2018). "Synthesis of vertically aligned CaTiO_3 nanotubes with simple hydrothermal method and its photoelectrochemical property." *Nanotechnology*, 29(38), 385605.

Singh, S., Singh, P., Viviani, M. and Presto, S. (2018). "Dy doped SrTiO_3 : A promising anodic material in solid oxide fuel cells." *Int. J. Hydrog. Energy*, 43(41), 19242–19249.

Sobahi, T. R. and Amin, M. S. (2021). "Photocatalytic oxidation of atrazine using BaTiO_3 -MWCNT nanocomposites under visible light." *Ceram. Int.*, 47(10), 14366–14374.

Song, J., Ling, Y., Xie, Y., Liu, L. and Zhu, H. (2018). "One-pot engineering TiO₂/graphene interface for enhanced adsorption and photocatalytic degradation of multiple organics." *Nanotechnology*, 29(39), 395701.

Song, S., Shen, H., Wang, Y., Chu, X., Xie, J., Zhou, N. and Shen, J. (2020). "Biomedical application of graphene: From drug delivery, tumor therapy, to theranostics." *Colloids Surf. B*, 185 110596.

Su, H. and Hu, Y. H. (2021). "Recent advances in graphene-based materials for fuel cell applications." *Energy Sci. Eng.*, 9(7), 958–983.

Sun, X., Li, H. J., Ou, N., Lyu, B., Gui, B., Tian, S., Qian, D., Wang, X. and Yang, J. (2019). "Visible-light driven TiO₂ photocatalyst coated with graphene quantum dots of tunable nitrogen doping." *Molecules*, 24(2), 344.

Tabish, T. A., Memon, F. A., Gomez, D. E., Horsell, D. W. and Zhang, S. (2018). "A facile synthesis of porous graphene for efficient water and wastewater treatment." *Sci. Rep.*, 8(1), 1817.

Tian, B., Li, C., Gu, F., Jiang, H., Hu, Y. and Zhang, J. (2009). "Flame sprayed V-doped TiO₂ nanoparticles with enhanced photocatalytic activity under visible light irradiation." *Chem. Eng. J.*, 151(1), 220–227.

Tonda, S., Kumar, S., Anjaneyulu, O. and Shanker, V. (2014). "Synthesis of Cr and La-codoped SrTiO₃ nanoparticles for enhanced photocatalytic performance under sunlight irradiation." *Phys. Chem. Chem. Phys.*, 16(43), 23819–23828.

Top, I., Binions, R., Warwick, M. E. A., Dunnill, C. W., Holdynski, M. and Abrahams, I. (2018). "VO₂/TiO₂ bilayer films for energy efficient windows with multifunctional properties." *J. Mater. Chem. C*, 6(16), 4485–4493.

Vattikuti, S. V. P., Police, A. K. R., Shim, J. and Byon, C. (2018). "In situ fabrication of the Bi₂O₃-V₂O₅ hybrid embedded with graphitic carbon nitride nanosheets: Oxygen vacancies mediated enhanced visible-light-driven photocatalytic degradation of organic pollutants and hydrogen evolution." *Appl. Surf. Sci.*, 447, 740–756.

Venkatesh, G., Vignesh, S., Srinivasan, M., Palanisamy, G., Elavarasan, N., Bhuvaneshwari, K., Ramasamy, P., Alam, M., Ubaidullah, M. and Raza, M. K. (2021). "Construction and investigation on perovskite-type SrTiO₃@ reduced graphene oxide hybrid nanocomposite for enhanced photocatalytic performance." *Colloids Surf. A Physicochem. Eng. Asp.*, 629, 127523.

Verhoeven, J. A. Th. and Van Doveren, H. (1982). "An XPS investigation of the interaction of CH₄, C₂H₂, C₂H₄ and C₂H₆ with a barium surface." *Surf. Sci.*, 123(2–3), 369–383.

Vijay, A. and Vaidya, S. (2021). "Tuning the morphology and exposed facets of SrTiO₃ nanostructures for photocatalytic dye degradation and hydrogen evolution." *ACS Appl. Nano Mater.*, 4, 3406-3415.

Wang, C., Zeng, Y., Xiao, X., Wu, S., Zhong, G., Xu, K., Wei, Z., Su, W. and Lu, X. (2020). "γ-MnO₂ nanorods/graphene composite as efficient cathode for advanced rechargeable aqueous zinc-ion battery." *J. Energy Chem.*, 43 182–187.

Wang, J., Han, F., Rao, Y., Hu, T., Huang, Y., Cao, J. and Lee, S. C. (2018). "Visible-light-driven nitrogen-doped carbon quantum dots/CaTiO₃ composite catalyst with enhanced NO adsorption for NO removal." *Ind. Eng. Chem. Res.*, 57(31), 10226–10233.

Wang, K., Miao, C., Liu, Y., Cai, L., Jones, W., Fan, J., Li, D. and Feng, J. (2020). "Vacancy enriched ultrathin TiMgAl-layered double hydroxide/graphene oxides composites as highly efficient visible-light catalysts for CO₂ reduction." *Appl. Catal. B*, 270, 118878.

Wang, R., Ni, S., Liu, G. and Xu, X. (2018). "Hollow CaTiO₃ cubes modified by La/Cr co-doping for efficient photocatalytic hydrogen production." *Appl. Catal. B*, 225, 139–147.

Wang, R. X., Zhu, Q., Wang, W. S., Fan, C. M. and Xu, A. W. (2015). "BaTiO₃-graphene nanocomposites: Synthesis and visible light photocatalytic activity." *New J. Chem.*, 39(6), 4407–4413.

Wang, Z., Huang, J., Mao, J., Guo, Q., Chen, Z. and Lai, Y. (2020). "Metal–organic frameworks and their derivatives with graphene composites: Preparation and applications in electrocatalysis and photocatalysis." *J. Mater. Chem. A*, 8(6), 2934–2961.

Wei, X., Xu, G., Ren, Z., Xu, C., Shen, G. and Han, G. (2008). "PVA-assisted hydrothermal synthesis of SrTiO₃ nanoparticles with enhanced photocatalytic activity for degradation of RhB." *J. Am. Ceram. Soc.*, 91(11), 3795–3799.

Wong, C. P. P., Lai, C. W., Lee, K. M., Pan, G. T., Chong, K. B., Johan, M. R., Juan, J. C. and Yang, T. C. K. (2021). "A high-capacity of oxygen induced SrTiO₃ cathode material for rechargeable alkaline zinc battery." *Mater. Sci. Semicond. Process.*, 130 105802.

Wu, J. C. S. and Chen, C. H. (2004). "A visible-light response vanadium-doped titania nanocatalyst by sol–gel method." *J. Photochem. Photobiol. A*, 163(3), 509–515.

Wu, J., Wang, W., Tian, Y., Song, C., Qiu, H. and Xue, H. (2020). "Piezotronic effect boosted photocatalytic performance of heterostructured BaTiO₃/TiO₂ nanofibers for degradation of organic pollutants." *Nano Energy*, 77, 105122.

Wu, R., Ding, Y., Yu, K. M., Zhou, K., Zhu, Z., Ou, X., Zhang, Q., Zhuang, M., Li, W. D., Xu, Z., Altman, M. S. and Luo, Z. (2019). "Edge-epitaxial growth of graphene on Cu with a hydrogen-free approach." *Chem. Mater.*, 31(7), 2555–2562.

Wu, Z., Zhang, Y., Wang, X. and Zou, Z. (2017). "Ag@SrTiO₃ nanocomposite for super photocatalytic degradation of organic dye and catalytic reduction of 4-nitrophenol." *New J. Chem.*, 41(13), 5678–5687.

Liu, X., Fan, B., Wang, Z., Guo, Z., Tang, B., Lv, S., Xing, A., Zhang, J., Cheng, X. and Xie, H. (2021). "Dynamic internal field engineering in BaTiO₃-TiO₂ nanostructures for photocatalytic dye degradation." *ACS Appl. Nano Mater.*, 4(4), 3742–3749.

- Xian, T., Yang, H. and Huo, Y. S. (2014). "Enhanced photocatalytic activity of CaTiO₃-graphene nanocomposites for dye degradation." *Phys. Scr.*, 89(11), 115801.
- Xian, T., Yang, H., Di, L. J. and Dai, J. F. (2015). "Enhanced photocatalytic activity of BaTiO₃@g-C₃N₄ for the degradation of methyl orange under simulated sunlight irradiation." *J. Alloys Compd.*, 622, 1098–1104.
- Xian, T., Yang, H., Di, L., Ma, J., Zhang, H. and Dai, J. (2014). "Photocatalytic reduction synthesis of SrTiO₃-graphene nanocomposites and their enhanced photocatalytic activity." *Nanoscale Res. Lett.*, 9(1), 327.
- Xiao, H., Fan, T., Wang, Z., Hu, T., Tang, X., Ma, L. and Tang, P. (2020). "High-throughput first-principle calculations of the structural, mechanical, and electronic properties of cubic XTiO₃ (X = Ca, Sr, Ba, Pb) ceramics under high pressure." *Int. J. Quantum Chem.*, 120(10), e26168.
- Xie, P., Yang, F., Li, R., Ai, C., Lin, C. and Lin, S. (2019). "Improving hydrogen evolution activity of perovskite BaTiO₃ with Mo doping: Experiments and first-principles analysis." *Int. J. Hydrog. Energy*, 44(23), 11695–11704.
- Xie, T. H., Sun, X. and Lin, J. (2008). "Enhanced photocatalytic degradation of RhB driven by visible light-induced MMCT of Ti(IV)–O–Fe(II) formed in Fe-doped SrTiO₃." *J. Phys. Chem. C*, 112(26), 9753–9759.
- Xing, B., Yuan, R., Zhang, C., Huang, G., Guo, H., Chen, Z., Chen, L., Yi, G., Zhang, Y. and Yu, J. (2017). "Facile synthesis of graphene nanosheets from humic acid for supercapacitors." *Fuel Process. Technol.*, 165, 112–122.
- Xing, B., Zeng, H., Huang, G., Zhang, C., Yuan, R., Cao, Y., Chen, Z. and Yu, J. (2019). "Porous graphene prepared from anthracite as high performance anode materials for lithium-ion battery applications." *J. Alloys Comd.*, 779, 202–211.
- Xu, S., Guo, L., Sun, Q. and Wang, Z. L. (2019). "Piezotronic effect enhanced plasmonic photocatalysis by AuNPs/BaTiO₃ heterostructures." *Adv. Funct. Mater.*, 29(13), 1808737.

Xu, S., Liu, Z., Zhang, M. and Guo, L. (2019). "Piezotronics enhanced photocatalytic activities of Ag-BaTiO₃ plasmonic photocatalysts." *J. Alloys and Compd.*, 801, 483-488.

Xue, C., Hu, S., Chang, Q., Li, Y., Liu, X. and Yang, J. (2017). "Fluoride doped SrTiO₃/TiO₂ nanotube arrays with a double layer walled structure for enhanced photocatalytic properties and bioactivity." *RSC Adv.*, 7(78), 49759–49768.

Yahya, M. S., Lew, W. B., Halim Yap, F. A. and Ismail, M. (2018). "The catalytic effect of an inert additive (SrTiO₃) on the hydrogen storage properties of 4MgH₂Na₃AlH₆." *Int. J. Hydrog. Energy*, 43(45), 20801–20810.

Yamada, K., Suzuki, H., Abe, R. and Saeki, A. (2019). "Complex photoconductivity reveals how the nonstoichiometric Sr/Ti affects the charge dynamics of a SrTiO₃ photocatalyst." *J. Phys. Chem. Lett.*, 10(8), 1986–1991.

Yan, Y., Yang, H., Yi, Z., Li, R. and Wang, X. (2019). "Enhanced photocatalytic performance and mechanism of Au@CaTiO₃ composites with Au nanoparticles assembled on CaTiO₃ nanocuboids." *Micromachines*, 10(4), 254.

Yan, Y., Yang, H., Yi, Z., Li, R. and Xian, T. (2020). "Design of ternary CaTiO₃/g-C₃N₄/AgBr Z-scheme heterostructured photocatalysts and their application for dye photodegradation." *Solid State Sci.*, 100, 106102.

Yan, Y., Yang, H., Zhao, X., Li, R. and Wang, X. (2018). "Enhanced photocatalytic activity of surface disorder-engineered CaTiO₃." *Mater. Res. Bull.*, 105, 286-290.

Yang, H., Han, C. and Xue, X. (2014). "Photocatalytic activity of Fe-doped CaTiO₃ under UV–visible light." *J. Environ. Sci.*, 26(7), 1489–1495.

You, T. T., Yang, N., Shu, Y. Q. and Yin, P. G. (2019). "A DFT study on graphene-based surface-enhanced Raman spectroscopy of benzenedithiol adsorbed on gold/graphene." *J. Raman Spectrosc.*, 50(10), 1510–1518.

Yu, H., Wang, J., Yan, S., Yu, T. and Zou, Z. (2014). "Elements doping to expand the light response of SrTiO₃." *J. Photochem. Photobiol. A*, 275, 65–71.

- Yu, H., Zhang, B., Bulin, C., Li, R. and Xing, R. (2016). "High-efficient synthesis of graphene oxide based on improved Hummers method." *Sci. Rep.*, 6(1), 36143.
- Zhang, H., Chen, G., He, X., and Xu, J. (2012). "Electronic structure and photocatalytic properties of Ag-La codoped CaTiO_3 ." *J. Alloys Compd.*, 516, 91–95.
- Zhang, H., Chen, G., Li, Y. and Teng, Y. (2010). "Electronic structure and photocatalytic properties of copper-doped CaTiO_3 ." *Int. J. Hydrog. Energy*, 35(7), 2713–2716.
- Zhang, Q., Chen, D., Song, Q., Zhou, C., Li, D., Tian, D. and Jiang, D. (2021). "Holey defected TiO_2 nanosheets with oxygen vacancies for efficient photocatalytic hydrogen production from water splitting." *Surf. Interfaces*, 23, 100979.
- Zhang, X., Wen, H., Chen, X., Wu, Y. and Xiao, S. (2017). "Study on the thermal and dielectric properties of SrTiO_3 /epoxy nanocomposites." *Energies*, 10(5), 692.
- Zhang, X., Yue, J., Zhao, Y., Yan, Z., Zhu, G., Liu, L., Xu, H. and Yu, A. (2021). "Synthesis of tetragonal BaTiO_3 nano-particle via a novel tartaric acid co-precipitation process." *Ceram. Int.*, 47(5), 7263–7267.
- Zhang, Y., Shen, G., Sheng, C., Zhang, F. and Fan, W. (2021). "The effect of piezo-photocatalysis on enhancing the charge carrier separation in $\text{BaTiO}_3/\text{KNbO}_3$ heterostructure photocatalyst." *Appl. Surf. Sci.*, 562, 150164.
- Zhang, Z., Shao, C., Zhang, L., Li, X. and Liu, Y. (2010). "Electrospun nanofibers of V-doped TiO_2 with high photocatalytic activity." *J. Colloid Interface Sci.*, 351(1), 57–62.
- Zhao, J., Chen, C. and Ma, W. (2005). "Photocatalytic degradation of organic pollutants under visible light irradiation." *Top. Catal.*, 35(3), 269–278.
- Zhao, Y., Zhang, X., Liu, J., Wang, C., Li, J. and Jin, H. (2018). "Graphene oxide modified nano-sized BaTiO_3 as photocatalyst." *Ceram. Int.*, 44(13), 15929–15934.

Zhong, D., Liu, W., Tan, P., Zhu, A., Qiao, L., Bian, Y. and Pan, J. (2019). "Efficient hydrogen generation of indium doped BaTiO₃ decorated with CdSe quantum dots: Novel understanding of the effect of doping strategy." *Int. J. Hydrog. Energy*, 44(3), 1627–1639.

Zhou, J., Chen, Z., Lu, Z., He, X. and Fu, X. (2021). "Morphology transformation of barium titanate nanostructures in molten salt medium." *Mater. Chem. Phys.*, 273, 125094.

Zhou, L., Dai, S., Xu, S., She, Y., Li, Y., Leveneur, S. and Qin, Y. (2021). "Piezoelectric effect synergistically enhances the performance of Ti₃₂-oxo-cluster/BaTiO₃/CuS p-n heterojunction photocatalytic degradation of pollutants." *Appl. Catal. B*, 291, 120019.

Zhou, Q., Li, N., Chen, D., Xu, Q., Li, H., He, J. and Lu, J. (2022). "Efficient removal of bisphenol A in water via piezocatalytic degradation by equivalent-vanadium-doped SrTiO₃ nanofibers." *Chem. Eng. Sci.*, 247, 116707.

Zhou, X., Shi, J. and Li, C. (2011). "Effect of metal doping on electronic structure and visible light absorption of SrTiO₃ and NaTaO₃ (Metal = Mn, Fe, and Co)." *J. Phys. Chem. C*, 115(16), 8305–8311.

Zou, F., Jiang, Z., Qin, X., Zhao, Y., Jiang, L., Zhi, J., Xiao, T. and Edwards, P. P. (2012). "Template-free synthesis of mesoporous N-doped SrTiO₃ perovskite with high visible-light-driven photocatalytic activity." *Chem. Commun.*, 48(68), 8514–8516.

Zou, J. P., Zhang, L. Z., Luo, S. L., Leng, L. H., Luo, X. B., Zhang, M. J., Luo, Y. and Guo, G. C. (2012). "Preparation and photocatalytic activities of two new Zn-doped SrTiO₃ and BaTiO₃ photocatalysts for hydrogen production from water without cocatalysts loading." *Int. J. Hydrog. Energy*, 37(22), 17068–17077.

LIST OF PUBLICATIONS

Papers published in international journals

Bantawal, H. and Bhat, D.K. (2018). "Hierarchical porous BaTiO₃ nano-hexagons as a visible light photocatalyst." *International Journal of Engineering & Technology*, 7, 105-109.

Shenoy, U.S., Bantawal, H. and Bhat, D.K. (2018). "Band engineering of SrTiO₃: effect of synthetic technique and site occupancy of doped rhodium." *The Journal of Physical Chemistry C*, 122(48), 27567-27574.

Bantawal, H., Sethi, M., Shenoy, U.S. and Bhat, D.K. (2019). "Porous graphene wrapped SrTiO₃ nanocomposite: Sr-C bond as an effective coadjutant for high performance photocatalytic degradation of methylene blue." *ACS Applied Nano Materials*, 2(10), 6629-6636.

Bantawal, H., Shenoy, U.S. and Bhat, D.K. (2020). "Vanadium-doped SrTiO₃ nanocubes: insight into role of vanadium in improving the photocatalytic activity." *Applied Surface Science*, 513, 145858.

Bhat, D.K., Bantawal, H. and Shenoy, U.S. (2020). "Rhodium doping augments photocatalytic activity of barium titanate: effect of electronic structure engineering." *Nanoscale Advances*, 2(12), 5688-5698.

Bantawal, H. and Bhat, D.K. (2020). "BaTiO₃-graphene nanocomposite as a photocatalyst for the degradation of methylene blue." *AIP Conference Proceedings*, 2247, 040004.

Bantawal, H., Shenoy, S.U. and Bhat, D.K. (2021). "Vanadium doped CaTiO₃ cuboids: role of vanadium in improving the photocatalytic activity." *Nanoscale Advances*, 3, 5301-5311.

Bantawal, H., Shenoy, U.S. and Bhat, D.K. "Porous graphene-BaTiO₃ nanocomposite as a high performance photocatalyst: enhanced photoresponse and efficient charge transfer." (Under review).

Bantawal, H. and Bhat, D.K. “Designing porous graphene-CaTiO₃ nanocomposite for the enhanced visible-light response, reduced charge recombination and improved photocatalytic activity.” (Manuscript under preparation).

CONFERENCES ATTENDED

Bantawal, H. and Bhat, D.K. (2018). “Rh-doped SrTiO₃ as a visible light photocatalyst.” National Symposium on Catalysis, held at Bengaluru on 17-19 January, 2018.

Bantawal, H. and Bhat, D.K. (2018). “Hierarchical porous BaTiO₃ nano-hexagons as a visible light photocatalyst.” International Conference on Recent Trends in Engineering and Sciences, held at Vishakapatnam on 20-21 February, 2018.

Bantawal, H., Shenoy, U.S. and Bhat, D.K. (2018). “Enhancing the photocatalytic activity of SrTiO₃ by tuning the Sr/Ti ratio: unusual effect of viscosity of synthesis medium.” 37th Annual National Conference of Indian Council of Chemists, held at National Institute of Technology Karnataka Surathkal on 12-14 December, 2018.

Bantawal, H., Shenoy, U.S. and Bhat, D.K. (2019). “Improving the photocatalytic activity of SrTiO₃ by altering the Sr/Ti ratio: unusual effect of viscosity of synthesis medium.” One Day National Seminar on Current Trends in Chemical Research and Development (CTCRD-2019), held at Vivekananda College of Arts, Science & Commerce Puttur on 18 September, 2019.

Bantawal, H. and Bhat, D.K. (2019). “BaTiO₃-graphene nanocomposite as a photocatalyst for the degradation of methylene blue.” International Conference on Design, Materials & Manufacture, held at National Institute of Technology Karnataka Surathkal on 6-8 December, 2019.

Bantawal, H., Sethi, M., Shenoy, U.S. and Bhat, D.K. (2020). “Designing porous graphene-SrTiO₃ nanocomposite for effective charge transfer, reduced recombination and improved photocatalytic activity.” National Conference on Frontiers of Catalysis Science & Technology and its Applications (FOCSTA-2020), held at St. Joseph’s College Bengaluru on 10-11 January, 2020.

BIODATA

HARSHA B

No. 318, Suvidha Homes Apartment, Opposite Maruthi Gas Agency, Pervaje Road, Karkala-574104, INDIA| +91-8095510090| harshabkb48@gmail.com

Personal details

Date of birth: 25.05.1993 | Gender: Male | Nationality: Indian

Education

Research Student | Department of Chemistry, National Institute of Technology Karnataka (NITK), India | Since January 2016

Guide: Prof. D. Krishna Bhat

Topic: Perovskite alkaline earth titanates based nanomaterials as photocatalysts

M.Sc. Chemistry | 2013-15 | Davangere University, India

‘A’ grade with University Rank Holder

B.Sc. Physics, Chemistry and Mathematics | 2010-2013 | Tumkur University, India

Percentage: 87.79 %

XIIth standard | 2010 | Vaishnavi Chethana Pre-University College Tumkur, Karnataka State Pre-University Board

Percentage: 79.66 %

Xth standard | 2008 | SVS High School, Karnataka Secondary Education Examination Board

Percentage: 79.36 %

Laboratory techniques/training

- Synthesis of nanomaterials including simple metal oxides, perovskites, spinels, metal sulfides by solvothermal/hydrothermal method, sol-gel method, and solid-state method.
- Synthesis of high-quality graphene and graphene-based nanocomposites by solvothermal/hydrothermal method.
- Synthesis of metal-doped perovskites by solvothermal/hydrothermal method, sol-gel method, and solid-state methods.

- Trained in handling photoreactor set-up, autoclaves, microwave ovens, homogenizer, probe sonicator, etc.
- Handsome experience in designing photoreactor setup for water splitting.
- Handsome experience in handling instruments like XRD, SEM, FTIR, UV-DRS, PL, etc.

Computer proficiency

- Extensive experience with Microsoft Office.
- Experience in handling scientific software including Chemdraw, Origin, Casa XPS, X'Pert Highscore, PeakFit, and Image J.

Research Publications

- Bantawal, H. and Bhat, D.K. (2018). "Hierarchical porous BaTiO₃ nano-hexagons as a visible light photocatalyst." *International Journal of Engineering & Technology*, 7, 105-109.
- Bantawal, H., Shenoy, U.S. and Bhat, D.K. (2018). "Tuning the photocatalytic activity of SrTiO₃ by varying the Sr/Ti ratio: unusual effect of viscosity of the synthesis medium." *The Journal of Physical Chemistry C*, 122(34), 20027-20033.
- Shenoy, U.S., Bantawal, H. and Bhat, D.K. (2018). "Band engineering of SrTiO₃: effect of synthetic technique and site occupancy of doped rhodium." *The Journal of Physical Chemistry C*, 122(48), 27567-27574.
- Bantawal, H., Sethi, M., Shenoy, U.S. and Bhat, D.K. (2019). "Porous graphene wrapped SrTiO₃ nanocomposite: Sr-C bond as an effective coadjutant for high performance photocatalytic degradation of methylene blue." *ACS Applied Nano Materials*, 2(10), 6629-6636.
- Bantawal, H., Shenoy, U.S. and Bhat, D.K. (2020). "Vanadium-doped SrTiO₃ nanocubes: insight into role of vanadium in improving the photocatalytic activity." *Applied Surface Science*, 513, 145858.
- Bhat, D.K., Bantawal, H. and Shenoy, U.S. (2020). "Rhodium doping augments photocatalytic activity of barium titanate: effect of electronic structure engineering." *Nanoscale Advances*, 2(12), 5688-5698.
- Bantawal, H. and Bhat, D.K. (2020). "BaTiO₃-graphene nanocomposite as a photocatalyst for the degradation of methylene blue." *AIP Conference Proceedings*, 2247, 040004.

- Bantawal, H., Shenoy, S.U. and Bhat, D.K. (2021). “Vanadium doped CaTiO₃ cuboids: role of vanadium in improving the photocatalytic activity.” *Nanoscale Advances*, 3, 5301-5311.
- Bantawal, H., Shenoy, U.S. and Bhat, D.K. “Porous graphene-BaTiO₃ nanocomposite as a high performance photocatalyst: enhanced photoresponse and efficient charge transfer.” (Under review).
- Bantawal, H. and Bhat, D.K. “Designing porous graphene-CaTiO₃ nanocomposite for the enhanced visible-light response, reduced charge recombination and improved photocatalytic activity.” (Manuscript under preparation).

Conferences attended

- Bantawal, H. and Bhat, D.K. (2018). “Rh-doped SrTiO₃ as a visible light photocatalyst.” National Symposium on Catalysis, held at Bengaluru on 17-19 January, 2018.
- Bantawal, H. and Bhat, D.K. (2018). “Hierarchical porous BaTiO₃ nano-hexagons as a visible light photocatalyst.” International Conference on Recent Trends in Engineering and Sciences, held at Vishakapatnam on 20-21 February, 2018.
- Bantawal, H., Shenoy, U.S. and Bhat, D.K. (2018). “Enhancing the photocatalytic activity of SrTiO₃ by tuning the Sr/Ti ratio: unusual effect of viscosity of synthesis medium.” 37th Annual National Conference of Indian Council of Chemists, held at National Institute of Technology Karnataka Surathkal on 12-14 December, 2018.
- Bantawal, H., Shenoy, U.S. and Bhat, D.K. (2019). “Improving the photocatalytic activity of SrTiO₃ by altering the Sr/Ti ratio: unusual effect of viscosity of synthesis medium.” One Day National Seminar on Current Trends in Chemical Research and Development (CTCRD-2019), held at Vivekananda College of Arts, Science & Commerce Puttur on 18 September, 2019.
- Bantawal, H. and Bhat, D.K. (2019). “BaTiO₃-graphene nanocomposite as a photocatalyst for the degradation of methylene blue.” International Conference on Design, Materials & Manufacture, held at National Institute of Technology Karnataka Surathkal on 6-8 December, 2019.
- Bantawal, H., Sethi, M., Shenoy, U.S. and Bhat, D.K. (2020). “Designing porous graphene-SrTiO₃ nanocomposite for effective charge transfer, reduced recombination and improved photocatalytic activity.” National Conference on Frontiers of Catalysis

Science & Technology and its Applications (FOCSTA-2020), held at St. Joseph's College Bengaluru on 10-11 January, 2020.

Awards and achievements

1. Won “**YOUNG SCIENTIST AWARD**” in a one-day National Seminar on Current Trends in Chemical Research and Development (CTCRD-2019) held at Vivekananda College of Arts, Science & Commerce Puttur on 18th September, 2019.
2. Selected as a “**SCIENTIST TRAINEE**” in a chemistry lab (R&D) at Anthem Biosciences Private Limited Bengaluru.
3. Selected as a “**STUDENT TUTOR**” for remedial coaching classes conducted for students from poor backgrounds at the National Institute of Technology Karnataka (NITK).
4. Won “**SECOND PRIZE**” in a debate competition on pheromones in RANST (Recent Advancements in Nano Science and Technology) organized at govt. science college Chitradurga on 22 and 23 April 2014.

“If you want to leave your footprints on the sands of time, do not drag your feet”

---A.P.J. Abdul Kalam
